BIOMECHANICAL MODELING OF THE HUMAN UPPER BODY FOR ROTORCRAFT/PILOT INTERACTION

Master's degree thesis of

ALESSANDRO COCCO

Politecnico di Milano
Department of Aerospace Science and Technology
Aerospace Structures

Supervisor: Prof. Pierangelo Masarati
Co-Supervisor: Prof. Vincenzo Muscarello
Co-Supervisor: Dott. Ing. Andrea Zanoni

Milan

April 2019

Dare to dream impossible thing,
then wake up and start working on them.
— Paolo Nespoli

Dedicated to my family that supports me in my studies

ABSTRACT

This work shows how different biodynamic modelling techniques are integrated in a rotorcraft design environment in order to evaluate the comfort inside it. Three modeling techniques are considered: lumped parameter, finite element and multibody dynamics. In particular a finite element model and a multibody model of the spine have been presented and validated comparing the frequency response function, between the acceleration at buttock and the acceleration at the head, of the developed model to similar models and experimental data available in literature. Even if the lumped parameter is the easiest to implement, it is limited to a single direction and also to a specific population group; instead the finite element as well as the multibody model can capture the movements in the three directions and also they can be adapted in order to match the response of a specific subject. This scaling procedure has been validated comparing the apparent mass of the model with an experimental campaign conducted by Toward and Griffin [38].
In the second part of the work the multibody model of the spine and of the upper limbs have been presented. They have been built using MBDyn, a software developed at Politecnico di Milano. The multibody formulation is able to capture well the non-linearities that are present in the system. Then the upper limbs model has been coupled with the reduced finite element model: the mixed formulation reduces the problem dimensions.
In the last part the multibody and the finite element model have been compared. Moreover the effect of vibrations in helicopter command response have been evaluated highlighting the impact that has a detailed modeling of the spine dynamic in the response: in particular, it has been observed that the collective oscillation are amplified when the dynamic of the spine is considered. Each of the three models have been integrated into a virtual helicopter environment with a seat-cushion interface, considering vibration up to 30 Hz. It is observed that the spine dynamics can play a significant role in estimating the acceleration of the head; therefore, the sophisticated finite element and multibody models redeem their higher modeling cost and computation time when the head-neck health of occupants is considered.

Keywords: multibody model; spine model; arm model; helicopter pilot model; finite element model; comfort;

SOMMARIO

Questo lavoro mostra come differenti strategie di modellazione biomeccanica sono integrate nel contesto di valutazione del comfort all'interno del progetto di un elicottero. Sono stati considerati tre differenti modelli: parametri concentrati, elementi finiti e modelli multicorpo. In particolare, è stato presentato e validato un modello di colonna vertebrale sviluppato usando sia la tecnica degli elementi finiti che multicorpo. La validazione del modello è stata compiuta confrontando le risposte in frequenza, tra l'accelerazione alle natiche e quella alla testa del modello sviluppato, con le risposte sperimentali e quelle fornite dai modelli a parametri concentrati. Anche se i modelli a parametri concentrati sono i più facili da implementare, essi possono valutare la dinamica in una sola direzione e inoltre possono rappresentare solo una ristretta popolazione. Al contrario il modello a elementi finiti, come quello multicorpo, può catturare la dinamica nelle tre direzioni e inoltre può essere adattato al fine di rappresentare al meglio la risposta di un singolo soggetto. La procedura di scalatura proposta è stata poi comparata con i risultati forniti dalla campagna sperimentale condotta nel lavoro di Toward and Griffin [38].
Nella seconda parte del lavoro sono stati presentati i modelli multicorpo della colonna vertebrale e degli arti superiori. Questi sono stati costruiti usando il software libero MBDyn sviluppato al Politecnico di Milano: il vantaggio principale è quello di poter catturare le nonlinearità che sono presenti nel modello. Successivamente il modello degli arti superiori è stato unito al modello ridotto, proveniente dal modello FEM, della colonna vertebrale: usando questa formulazione mista le dimensioni del problema si riducono notevolmente.
Nell'ultima parte sono stati confrontati il modello a elementi finiti e quello multicorpo. Inoltre, sono stati valutati gli effetti che comporta l'inserimento del modello ridotto, accoppiato con quello del braccio, nel problema di risposta ai comandi di un elicottero: è stato osservato in particolare che le oscillazioni del collettivo risultano amplificate quando viene considerata la dinamica della schiena. Infine, i tre modelli (parametri concentrati, elementi finiti e multicorpo) sono stati integrati all'interno di un modello agli stati di un elicottero, usando come elemento di interfaccia un sistema sedile-cuscino e considerando le vibrazioni fino a 30 Hz. E' stato osservato che la dinamica della colonna gioca un ruolo significativo nello stimare l'accelerazione della testa; perciò i sofisticati modelli a elementi finiti e multicorpo riscattano il loro alto costo computazionale e di modellazione quando viene considerata la salute del sistema collo-testa dell'occupante.

Parole-chiave: modello multicorpo; modello elementi finiti; modello pilota di elicottero; colonna vertebrale; braccio del pilota; comfort;

PUBLICATIONS

During this thesis period, I have the privilege to be the co-author of the following publications[1]:

[1] Aykut Tamer, Andrea Zanoni, Vincenzo Muscarello, Alessandro Cocco, Giuseppe Quaranta, and Pierangelo Masarati. "Biodynamic Modeling Techniques for Rotorcraft Comfort Evaluation." In: *Aerotecnica Missili & Spazio* (2019).

[2] Aykut Tamer, Andrea Zanoni, Alessandro Cocco, and Pierangelo Masarati. "Visual Performance Evaluation of Helicopter Pilots in Vibrating Cockpit." In: *ASME 2019 International Design Engineering Technical Conferences & Computers and Information in Engineering Conference* (2019).

1 They are currently submitted

ACKNOWLEDGEMENTS

First of all I want to thank my supervisor Prof. Masarati who gave me the opportunity to develop this work, and taking me in his wonderful research group. Then I have to thank a lot Ing. Andrea Zanoni who was always available in helping me in this work. Moreover I have to thank Prof. Muscarello who helps me in the developing of the finite element model. I want also to thank Aykut Tamer and Prof. Quaranta for their help.
Un sentito ringraziamento va alla mia famiglia che mi ha supportato e sostenuto in questi anni milanesi, sia nel percorso universitario che in quello musicale.
Ringrazio i coinquilini storici del Pensionato: Davide, Filippo L., Filippo P. Stefano, Gaetano con i quali abbiamo condiviso i momenti belli e meno belli di questi anni. Un grazie anche va ai compagni di università, dai compagni del primo anno: Alessandro, Cristiano e Nicolò ai quali si sono aggiunti in questi due anni di specialistica: Angelo, Alberto, Jacopo e Stefano, con i quali ho condiviso le fatiche di questi intensi anni.
Ringrazio infine gli amici dossonesi: Andrea G., Andrea B., Nicola, Francesco, Giovanni, Davide C., Davide M. per avermi fatto sempre sentire a casa ogni volta che tornavo.

CONTENTS

LIST OF FIGURES

LIST OF TABLES

ACRONYMS

FEM Finite Element Method

MBD Multibody Dynamics

LPM Lumped Parameter Model

BMI Body Mass Index

FRF Frequency Response Function

DOF Degrees of freedom

AM Apparent mass

STHT Seat to head transmissibility

DPMI Driving point mechanical impedance

CSD Cross spectral density

PSD Power spectral density

GA Genetic Algorithm

MASST Modern Aeroservoelastic State Space Tools

CMS Component Mode Synthesis

RMS Root mean square

Part I

STATE OF THE ART AND ANATOMY

The first part of the work is dedicated to present the the current state of the art on the biomechanical modeling of the spine. Secondly the spine anatomy has been revised, with a particular focus on the articulations.

1 INTRODUCTION

1.1 MOTIVATION

Vibration levels in helicopter are much higher than in fixed wing aircraft. These vibrations are primarily related to the oscillatory response of the airframe to time dependent loads. The predominant sources of vibration are the rotor forces and moments originating from the rotors, fuselage aerodynamics, engine and transmission. The resulting time dependent loads are transmitted to the fuselage, which excites the crew and occupants through their contact with the vehicle, usually the seat surface. In helicopters, vibrations can degrade the ride quality of the occupants and crew: high vibration levels can lead to an increasing of the pilot workload and to a degradation of the pilot's visual cues. Moreover, vibration might lead to chronic pain in the long-term [14]. For this reason, the interest on rotorcraft comfort assessment is increasing [36].

Helicopter ride-comfort is usually evaluated through flight test, since measuring vibration along with the effect of human body mechanical characteristics is essential to achieve a realistic comfort assessment. The disadvantage of this procedure is that only limited design improvements can be accommodated when the helicopter is ready for flight, and all the flight envelope needs to be analyzed. Therefore, in the design phase, engineers must mainly rely on computational tools when analyzing the potential impact of their design choices on the vibrational level of the helicopter.

Since the mechanical, physiological and psychological interaction of the human body with the vehicle dynamics may change the magnitude and perception of the accelerations, the resulting effects of vibration on the occupant are not directly correlated to the magnitude of the accelerations. Therefore, comfort assessment should take into account advantages in human-machine interaction modeling paradigms, starting from early design stages.

The goal of this work is then the developing of a biomechanical upper-body model that can be adopted in rotorcraft industry to evaluate the comfort inside the helicopter. Another important aspect that can be analyzed with this model is the role that the biodynamic of pilot covers when is coupled with the helicopter dynamics. This interaction shows up with the emergence of uncontrolled vibrations that derive from the reduction of the phase margin, due to the delay in the pilot's response, on the transfer function of the closed-loop system formed by the pilot and the vehicle.

1.2 STATE OF THE ART AND LITERATURE REVIEW

1.2.1 *Vibration in Helicopters*

In helicopter vibratory loads are transmitted from the blades to the rotor hub and then to the fuselage. These loads arise from aerodynamic forces and from inertia forces due to blade motions.
A rotor with identical blades equally spaced acts as a filter when all the blade loads are summed in the non-rotating reference frame. So then only the loads at frequencies which are integer multiples of fundamental frequency times the blade number (N_b/rev, where N_b is the number of blades) are transmitted to the fuselage [17][7]. Typically the N_b/rev vibrations exist regardless of the rotor condition and typically range from 10 Hz to 30 Hz, with exceptional values as high as 47Hz and as low as 4 Hz. There exist standards for comfort assessment: the rather general ISO-2631 [16], the air vehicle specific NASA Ride Quality (RQ) [21], and the rotorcraft specific Intrusion Index from Aircraft Design Standard (ADS) [33].
The ISO-2631 better reflects the helicopter crew ratings: it operates on a combination of time and frequency domain accelerations at several vibration interfaces, applying frequency weights with a qualitative scale. An important factor of ISO-2631 is the modulus of the ratio of the maximum instantaneous peak value of the acceleration signal to its root-mean-square Root mean square (RMS) value: a high value means that the vibration signal includes short-time acting shocks.
ISO-2631 recommends to use the magnitude of the frequency-weighted acceleration components with scaling factors. For the helicopter missions, this refers to the calculation of the translational acceleration along three axes at the seat surface. Thus we have:

$$\mathbf{a}(\mathbf{t}) = \begin{bmatrix} a_x(t) & a_y(t) & a_z(t) \end{bmatrix}^T \tag{1}$$

Since frequency weighting cannot be applied to a time signal, Fourier transformation ($\mathcal{F}$) is performed:

$$\mathcal{F}\left(\begin{bmatrix} a_x(t) \\ a_y(t) \\ a_z(t) \end{bmatrix}\right) = \sum_{n=-\infty}^{n=\infty} \begin{bmatrix} A_x(\omega_n) \\ A_y(\omega_n) \\ A_z(\omega_n) \end{bmatrix} e^{i\omega_n t} \tag{2}$$

Then, after applying the frequency (W_i) and directional (k_i) weights and performing the inverse Fourier transform, the frequency weighted acceleration becomes:

$$a_w = \mathcal{F}^{-1}\left(\sum_{n=-\infty}^{n=\infty} \begin{bmatrix} W_x k_x A_x(\omega_n) \\ W_y k_y A_y(\omega_n) \\ W_z k_z A_z(\omega_n) \end{bmatrix} e^{i\omega_n t}\right) \tag{3}$$

The ratings are given in terms of root mean square of the magnitude of the weighted acceleration over the exposure time T:

$$a_{w,RMS} = \sqrt{\frac{1}{T}\int_0^T a_w^T a_w dt} \tag{4}$$

Given the averaged weighted magnitude of acceleration of equation 4, ISO-2631 suggests to use a root-means-square averaged scale presented in table 1. The bounds are overlapping since human perception cannot be determined precisely.

Acceleration	**Rating**
Less than 0.03 g	not uncomfortable
0.03 g to 0.06 g	not comfortable
0.05 g to 0.10 g	a little uncomfortable
0.08 g to 0.16 g	fairly uncomfortable
0.13 g to 0.25 g	uncomfortable
Greater than 0.20 g	very uncomfortable

Table 1: Comfort rating after ISO-2631

1.2.2 *Human spine biomechanical models*

The methods used to model the human body can be divided into three categories: Lumped Parameter Model (LPM), FEM, and Multibody Dynamics (MBD).

1.2.2.1 *Lumped-Parameter model*

Lumped-Parameter models are the one that use simple mechanical elements, such as concentrated masses, dampers and springs, in order to simulate the dynamics of the human body. They main advantage of these models is its low computational cost and ease of parameter identification. The core of lumped parameter modeling is system identification of human body as a simplified mechanical system: the parameters are tuned in order to fit the biomechanical characteristics of a specific group of people. One disadvantage of the LPM models is that they are not consistent with the actual parameters of human anatomy and biodynamics, so then they may not fully reflect the responses of each part of human body. Also they are often used to describe a uni-directional dynamic responses of the human bodies because of compact expression and effective performance of the models with only parameters of mass, stiffness and damping.
One of the first lumped model was developed by Coermann [10] in

1962: he measured the mechanical impedance of eight people with different heights, weights and ages and proposed a 1 DOF linear model. Stech and Payne [35] proposed a 1 DOF non-linear model and applied it to the analysis of dynamic responses of human bodies during helicopter landing. The connection between the human body and seat was considered rigid and the seat was not included in the model. In 1995, Wan and Schimmels [42] presented a 4 DOF series-to-parallel linear model to describe the dynamic responses of seated occupants under vibration. The non-linear optimization of this model has been done by Abbas [1] using genetic algorithm. In 1998, Boileau and Rakheja [8] measured the vertical driving-point mechanical impedance of seated vehicle drivers in the range between 0.625-10 Hz. The measurement were performed varying the seated posture, backrest angle, and nature and amplitude of the vibration excitation. Then a 4 DOF linear model was proposed for which the parameters were estimated to satisfy both the measured driving-point mechanical impedance and the seat-to-head transmissibility characteristics defined from a synthesis of published data for subjects seated erect without backrest support. A multivariable optimization was performed using as objective function the sum of squared magnitude and phase magnitude associated with both the mechanical impedance and seat-to-head-transmissibility target values, and as limit constraints the anthropometric and biomechanical data: for example the sum of the lumped masses has to be equal to the experimental seated mass. An optimization of the Boileau model has been done by Zhang E [46] using an average-weighted Genetic Algorithm (GA).
In Bai et al. [3] is proposed a methodology for systematically identifying the best configuration or structure of a 4 DOF human vibration model and for its parameter identification. The models were calibrated using the frequency response functions recommended by the International Standard Organization [34]. In order to determine the model parameters an improved version of non-dominated sorting genetic algorithm based on Pareto optimization principle was used.

1.2.2.2 *FEM models*

The FEM models are more versatile with respect to the LPM system: first of all they respect the geometry of the human body, also they can be parametrized in order to have a model that is a able to represent all kind of people. Moreover the output of the analysis is far richer: for example in a frequency response analysis the acceleration of each vertebra of the spine can be measured. The two major drawbacks are that the computational cost is much higher and the identification of the mechanical parameters of the model is a really difficult task compared to the LPM.
The FEM models can be divided into two categories: discrete and continuum. The discrete models treat the spine as a structure made by

rigid elements, representing the vertebral bodies, that are connected through deformable elements representing the intervertebral discs. On the contrary, the continuum models treat the spine as homogeneous beam. Toth [37] modelled each vertebra separately in an 8 DOF non linear discrete model however, the model is restricted to only the axial direction. Orne and Liu [28] developed a discrete-parameter model of the human body under a variety of impact situations, in particular the pilot-ejection problem was deeply investigated, emphasizing the spine as the main load-carrying element. This model simultaneously accounts for axial, shear, and bending deformations of the discs, the variable size of the mass of the vertebrae and discs, the physiological curve of the spine and the eccentric inertial loading caused by the head and trunk. This model introduced the concept of modelling the inertial properties of the associated torso cross-sectional segment.
These two models were restricted to one or two dimensional behavior and did not consider the interaction of the spine with other parts of the torso such as the rib cage and the viscerae.
Belytschko, Schwer, and Schultz [6] developed a three dimensional, discrete mathematical model of the human spine, torso, and head. This model implements a small strain, large displacement formulation. The basic model developed was the isolated ligamentous spine model consisting of rigid bodies representing the head, vertebrae from T1 to L5 and the pelvis, interconnected by deformable elements representing the intervertebral discs and the various connective tissues. The complete model of Belytschko, Schwer, and Schultz [6] consisted of the ligamentous spine model plus a detailed representations of the cervical spine, the rib cage and the viscera. This model was able to capture the behavior of the spine in situations involving substantial bending. In Belytschko and Privitzer [5] a more accurate representation of the viscera-abdominal wall system and more reliable damping parameter were introduced. With these improvements the model was able to better match the experimental results, for instance the mechanical impedance of the spine.
The Kitazaki and Griffin [19] is an evolution of the Belytschko and Privitzer [5] model: the validation of this model did not seem exhaustive since it was done only considering the driving point impedance at the buttock down that can be dominated by the motion of the seat-buttocks interface and hardly reflects the motion of the other body parts. The Kitazaki and Griffin model is a 2D FEM model: it allows movements only in the mid-sagittal plane. The authors include in the model the spine, viscera, head, pelvis and buttock tissue, using beam, spring and mass elements. The geometrical and mechanical parameters were based on those presented in [5], but some of them were then modified in order to match the mode shapes obtained by the experimental work of Kitazaki and Griffin [20]. The model was entirely

linear and included 134 elements and 87 master degrees of freedom. The spinal column was modelled by 24 beam elements representing all the intervertebral discs between the vertebra C1 and the sacrum S1. All the discs were modelled separately to predict all the possible bending modes of the spine. Each beam was placed between the geometrical centers of adjacent vertebral bodies, and was given the axial and bending stiffness of the corresponding disc. Since no mass was assign to the beam elements, lumped mass elements were located anteriorly to the spine in the region between the T1 and T10 levels by massless rigid links. Below the T10 level the masses were placed in the geometric center of the corresponding vertebra and viscera. The same was done for the cervical region. Only the viscera below the T10 level was modelled because the mass of the viscera within the abdominopelvic cavity seemed to be larger than that within the thoracic cavity and it was thought that its local motion might affect the dynamic response of the whole body. The visceral column in the abdominopelvic cavity was modelled by seven mass elements at the levels from T11 to L5 interconnected by spring elements. The top and bottom node of the viscereral was connected to the T10 and the pelvic by a massless rigid link. The interaction between the spine and the viscerae was modelled by horizontal spring elements that connect the visceral masses and the spinal beams. In order to simplify the model, the motion of the viscerae was assumed to occur only in the axial direction. This may be valid for vertical vibration under 10 Hz : the viscera within the abdominopelvic cavity may behave like a balloon ([6]). The head was modelled as a lumped mass connected to the top of the spinal beam at the C1 level; the pelvis was also a lumped mass connected at S1 level. The buttocks tissue were modelled with two beam elements in order to allow rotation and fore-and-aft motion of the pelvis. The limbs were not modelled but their presence was taken into account in the inertial properties of the model. The mass of the upper arms was equally distributed to the translational torso masses for the levels from T1 to T6. The translational pelvic mass was supplemented by 30% of the translational masses of the thighs, forearms and hands. The rotational pelvic mass was increased by 50%, so as to account for the additional inertia of the hands and forearms placed of the thighs.

1.2.2.3 *Multibody models*

The multibody model adds flexibility to LPM with the ease of constraint formulation. Furthermore, flexible elements include and extend the capabilities of FEM models. The great advantage of Multibody model is that it can capture effects related to nonlinearities, especially the one originating from 3D geometry with ease. The multibody approach can be less onerous to be solved and can be easily integrated in a more complex simulative environment.

In the work of Yoshimura, Nakai, and Tamaoki [43] a multibody model of the spine having 10 DOF was presented: this model was restricted to the sagittal plane; the cervical and thoracic curvature were expressed as one rigid body. The lumbar curvature was modeled by five rigid bodies, the sacrum and coccyx by one rigid body. The connection between the vertebrae was realized by revolute joint, and the dynamics of intervertebral disk was represented by rotational spring and rotational dampers. Two sets of translational springs and dampers represented the interface between the seat and buttocks.
In the work of Desai, Guha, and Seshu [11] a 2D 20 DOF model that can be used to study the vertical and fore-aft vibrations was proposed. The parameters were optimized using a GA algorithm that minimizes the error of the seat to head transmissibility and the apparent mass between the model and the experimental values. The effect of the backrest was also considered.
A full multibody model of the spine was proposed by Valentini [40] for an accurate assessment of seated body vibration, but also this model wasclimited in the sagittal plane. In Valentini and Pennestrì [41] the previous model was improved in order to be able to capture the three-dimensional motion of the spine. The model was composed by 33 rigid bodies: the head, 24 vertebrae, the sacrum and 7 visceral masses placed using the Kitazaki and Griffin [19] approach. The model did not include any kinematic constraint, but the intraverebral disks were modelled using a six DOF bushing element composed by 6 dampers and 6 springs. The interaction between two adjacents vertebrae was represented by the internal force of the linear viscoelastic elements:

$$F_{i,i-1} = \mathbf{K}_{i,i-1}\delta_{i,i-1} - \mathbf{C}_{i,i-1}\dot{\delta}_{i,i-1} \tag{5}$$

Where:

- $\mathbf{K}_{i,i-1}$ is the 6x6 stiffness matrix
- $\mathbf{C}_{i,i-1}$ is the 6x6 damping matrix
- $\delta_{i,i-1}$ and $\dot{\delta}_{i,i-1}$ are the vectors of relative displacement and velocity, respectively, between the two bushing reference system $\{0_{b,i}\ x_{b,i}\ y_{b,i}\ z_{b,i}\}^T$ and $\{0_{b,i-1}\ x_{b,i-1}\ y_{b,i-1}\ z_{b,i-1}\}^T$ showed in figure 1.

Each viscera was connected to the corresponding vertebra using an axial bushing element. The compliance of the buttocks was also modeled with another bushing element.

1.2.2.4 *Comparison of numerical models with the experimental results*

The biodynamic response behaviors of seated human body subject to whole-body vibration of different types and magnitude has been

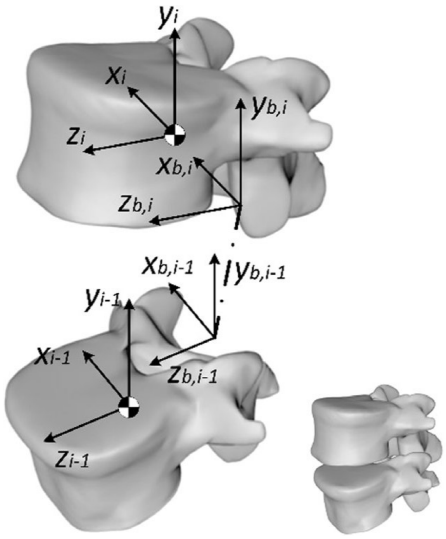

Figure 1: Reference systems for the definition of the interaction between vertebrae. From Valentini and Pennestrì [41]

widely investigated, also the role of seat design and sitting posture has been studied.

Fairley and Griffin [12] analyzed the vertical apparent mass of 60 seated subject including 24 men, 24 women and 12 children. The measurements were performed using as input a random acceleration at frequencies up to 20 Hz. In this work the effect of the footrest, the backrest, posture, muscle tension and vibration magnitude were also investigated. As result was found that the resonance frequencies generally increased with the use of a backrest, an erect posture and increased muscle tension. Also, the magnitude of the input acceleration plays an important effect: the resonance frequencies decreases from 6 to 4 Hz when the input acceleration magnitude was increased from 0.25 to 2 m/s^2. The apparent mass normalized with respect to the sitting mass shows very similar trends: the first resonance peak was found around 5 Hz with a magnitude of 1.5 times the static mass.

In Boileau and Rakheja [8] the driving-point mechanical impedance was evaluated using 7 male subjects seated on a rigid seat and subjected to ten different acceleration excitation. The evaluation was performed considering three sitting postures: sitting erect with the lower back in contact with the backrest, sitting erect with most of the back in contact with the backrest and sitting in a slouched posture. Most of the experiments were conducted with a seat backrest angle of 0° and few experiments were conducted with an inclination of 14°. The whole body resonance frequency was predicted at 4.875 Hz for a seated driver of 75.4 kg mass maintaining a slouched posture. The response variability among the subjects were observed to be larger around the resonance peak and at higher frequencies, but usually within 10% of the mean values.

In Kitazaki and Griffin [20] eight subjects were exposed to vertical

random vibration while adopting three different postures on a rigid seat without backrest. 8 modes were extracted in the frequency bandwidth under 10 Hz. The principal resonance of the human body was observed at about 5 Hz: it consisted of an entire body mode, in which the skeleton moves vertically due to axial and shear deformations of buttocks tissue, in phase with a vertical visceral mode, and a bending of the upper thoracic and cervical spine. The second principal resonance was found at about 8 Hz corresponded to pitching modes of the pelvis and a second visceral mode. When the subjects changed posture from erect to slouched, the natural frequency of the entire body mode decreased, resulting in a decrease in the principal resonance frequency. These experimental results were used by the author to validate the FEM model presented in [19].

In Toward and Griffin [38] the vertical apparent mass of 80 seated adults (41 males and 39 females aged 18-65) were measured at frequencies between 0.6 and 20 Hz with four backrest condition and three magnitude of random vibration (0.5, 1.0 and 1.5 m/s^2). With a multiple regression models the relationship between the subject physical characteristics, such as age, gender, weight and and gender, were investigated. The strongest parameter that influenced the resonance mass was the body weight; the other parameters showed in a marginal effect. The age had an influence in the resonance frequency: in fact as the age increased from 18 to 65 years old, the resonance frequency increased by 1.7 Hz. The Body Mass Index (BMI) had also an influence: when increased from 18 to 34 kg/m^2 the resonance frequency decreased by up to 1.7 Hz.

In Mandapuram et al. [22] the apparent mass and STHT of the seated human body were investigated under whole body vibration exposures to fore-aft, lateral, and vertical applied individually and simultaneously. The experiments were performed with 9 adult male subjects to measure the biodynamic responses to single and uncorrelated three-axis vibration with and without hands and back supports under different magnitudes of random vibration. The results revealed significant effects of hands and back support conditions on the coupling effects of multiple axis vibration and measured responses.

The International Standard Organization [34] defined the ideal ranges of Apparent mass (AM) and STHT magnitude and phase responses of the human body seated without a back support and exposed to vertical vibration of magnitude up to $5m/s^2$. This standard did not provide limits for the back supported by the backrest and for responses to fore-aft and lateral vibration. The data ranges in the document were derived from synthesis of data reported in different studies where the standing body mass or total body mass of the subject varied from 49 to 93 kg with a mean mass of 75 kg. The standard identified the higher primary resonance frequencies near 4 Hz. In contrast all the considered models show a primary resonance peak at 4.6-4.8

Hz. The considerable lower primary frequency of the standardized ranges is attributable to the considerations of data sets obtained under relatively higher magnitudes of vibrations [31] as shown in figure 2. The mean and limits of the AM data exhibitd some differences with respect to the standardized values. Even larger deviation were found in the STHT magnitude and phase.

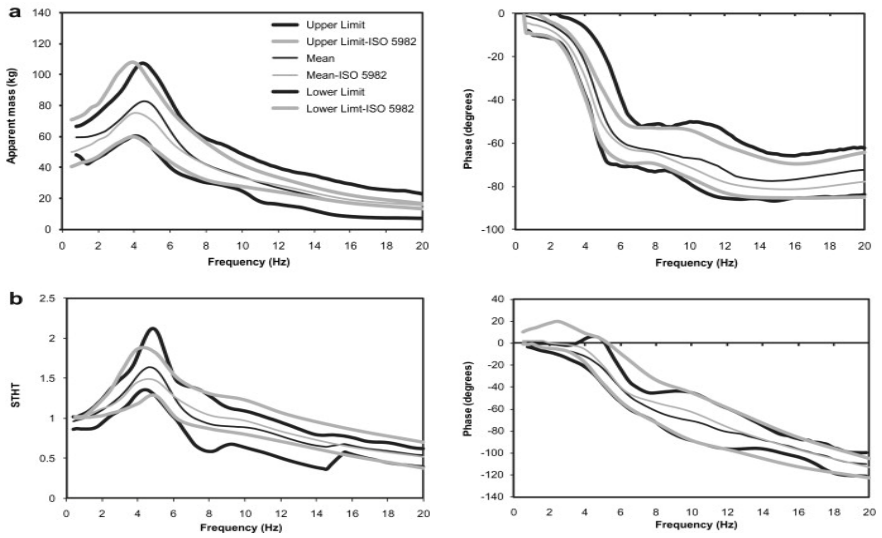

Figure 2: Comparisons of ranges of biodynamic responses with those defined in ISO [34]: (a) Vertical apparent mass magnitude and phase; (b) Vertical STHT magnitude and phase. From Rakheja et al. [31]

1.3 MULTIBODY VS FINITE ELEMENTS APPROACH

In this work the Finite Elements and the Multibody approach are both used in order to develop an accurate spine model. The FEM formulation offers quite good results with respect to the experiments in particular in frequency response and modal analysis. The need of a multibody model of the spine has been dictated to overcame the limitation of the Finite Element approach. The FEM in fact solves a linear system, so then the solution does not take into consideration the non-linearity that are presented in the model. This approach is then more adapted to capture the non-linearities of the system, at least the geometric one. Moreover the MBD solver is able to solve also problems of inverse kinematics and dynamics: this capability can be used to place the model in "*strange*" configuration for example with the reclined backrest and constraining the head to watch in front, then with an inverse dynamic procedure the pre-strain of the joints can be evaluated as function of the new configuration of the spine. Since the kinematic problem is highly undetermined, the pre-strain of each joint is determined using a minimization problem. With the FEM approach instead this procedure is not applicable: when the an

inclination of the backrest is imposed a rigid rotation of the node coordinates is applied, without performing any inverse kinematic and dynamic problem. This simplifies the computational costs of the FEM model, but, on the other hand, may lead to more inaccurate results. The two approaches can be also joined together modelling the components in which the non-linear effect can be neglected with the FEM approach, and the remaining with the MBD approach. In the present work the coupling has been performed in paragraph 4.4.

1.4 THESIS OVERVIEW

This work is organized as follows:

- *Chapter 2*: a brief review of the the anatomy of the spine is done, with a particular focus on the types of articulation that compose this body structure.
- *Chapter 3*: an accurate description and validation of the FEM model is performed. The validation is done performing both modal and frequency response analysis and comparing the results with the models and of the experiments, that are already presents in literature.
- *Chapter 4*: the MBD model of the spine and of the upper limb are presented. Then a CMS is done connecting the FEM model of the spine with the MBD upper limb model. The validation is performed comparing the FRF of the FEM model with the FRF of the CMS model.
- *Chapter 5*: it presents the strategy used in order to permit to both the FEM and MBD models to be able to represents the human population variety, taking as a input the anthropometric parameters such as age, BMI, stature and gender. The results are then compared to the experimental result provided by Toward and Griffin [38].
- *Chapter 6*: the thesis results are presented. The different biomechanical model are placed the state space model of a medium size helicopter in order to evaluate the response to the vibration coming from the rotorcraft.
- *Chapter 7*: In this chapter conclusions and further development are discussed.

2 SPINE ANATOMY AND BIOMECHANICS

2.1 ANATOMY

2.1.1 *Anatomical planes*

To describe the biomechanics of the human body, especially the biomechanics of the spine, it is useful to set a Cartesian reference system. This system is originated from the intersection of the three anatomical planes. These planes are:

1. *Sagittal plane*: it is perpendicular to the ground, dividing the left from the right into two equal sections.
2. *Transverse plane*: it is parallel to the ground, dividing the head from the feet.
3. *Frontal plane*: it is perpendicular to the ground, dividing the anterior from the posterior, the front from the back, the ventral from the dorsal.

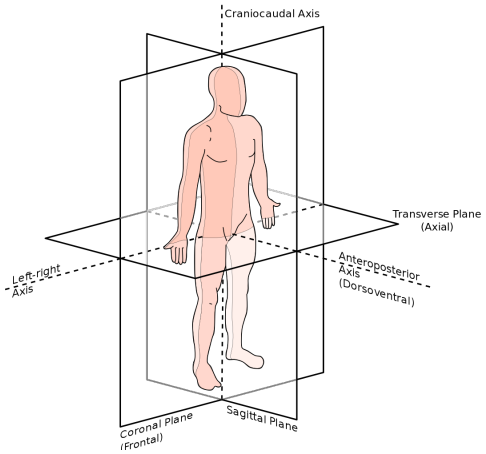

Figure 3: Anatomical plane

2.1.2 *Structure of the spine*

The human spine is a bone structure composed by 33 individual vertebrae stacked one on top of the other. The vertebrae are numbered and divided into 5 regions:

- *Cervical*: the main function of the cervical region is to support the weight of the head (about 4 kg). The vertebrae are numbered

from C1 to C7. The neck has the greatest range of motion because of two specialized vertebrae that connect to the skull: C1 is the ring shaped *atlas* that connects directly to the skull. This joint allows for the nodding motion of the head. C2 is the peg-shaped *axis*, which has a protection called the odontoid, that the atlas pivots around. This joint allows for the side-to-side motion of the head.

- *Thoracic*: the main function of the thoracic region is to hold the rib-cage and protect the heart and lungs. The twelve thoracic vertebrae are numbered from T1 to T12. This region does not a have a great range of motion.

- *Lumbar*: the main function of the lumbar region is to bear the weight of the body. The five lumbar vertebrae are numbered from L1 to L5: they are much larger in size in order to absorb the stresses, for example, of lifting and carrying heavy objects.

- *Sacrum*: the main function of the sacrum is to connect the spine to the hip bones. There are five sacral vertebrae from S1 to S5 which are fused together. This region with the iliac bones forms a ring called pelvic girdle.

- *Coccyx*: the four fused bones of the coccyx provide attachment for the ligaments and muscles of the pelvic floor.

Taking a midsagittal section of the body, it can be seen that an adult spine has a natural S-shaped curve: the cervical and lumbar regions have a slight concave curve, instead the thoracic and sacral regions have a gentle convex curve. These curves work like a coiled spring to absorb shock, maintain balance, and allow range of motion throughout the spinal column. The muscles and correct posture maintain the natural spinal curves.

2.1.3 *Articulations of the Vertebral Column*

The articulations of the spine are divided into two types:

- *Amphiarthrodial joints*: these are the joints between the vertebral bodies that permits only a slight movement. When this slight degree of movement between the pairs of bones take place in all the joints of the vertebral column, the total displacement that can be achieved is considerable. There are three ligaments of these articulations:

    1. *Anterior Longitudinal*: It consists of a strong band of dense longitudinal fibers. It extends along the anterior surfaces of the bodies of the vertebrae, from the axis (C2) to the sacrum.

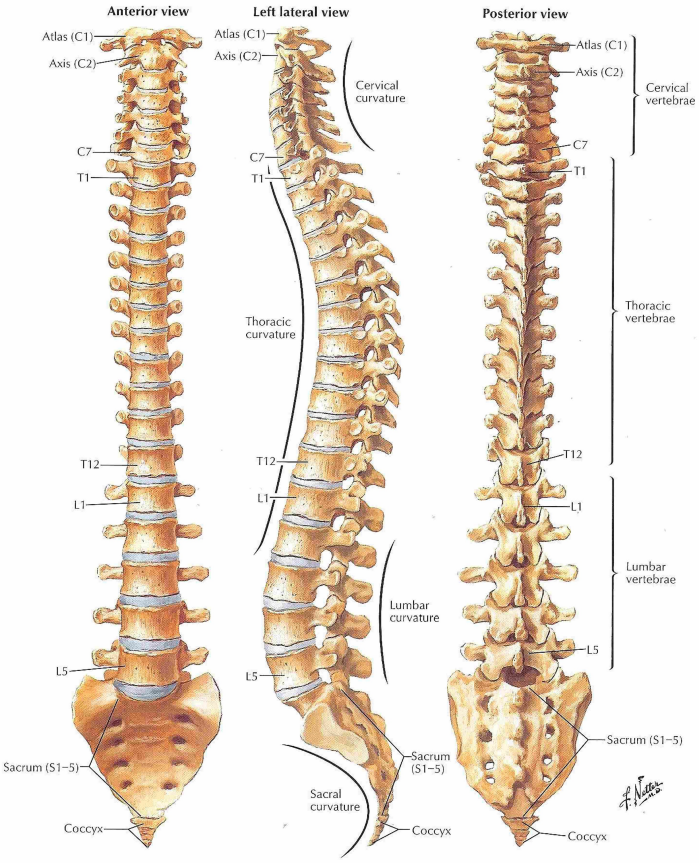

Figure 4: Spine subdivision. From Netter and Colacino [27]

2. *Posterior Longitudinal*: this ligament is situated within the vertebral canal, and extends along the posterior surfaces of the bodies of the vertebrae, from the body of the axis to the sacrum. It is composed of smooth, longitudinal fibers, denser and more compact than those of the anterior ligaments.

3. *Intervertebral Fibrocartilages*: these ligaments are placed between the adjacent surfaces of the bodies of the vertebrae, from the axis to the sacrum, and form the chief bonds of connection between the vertebrae. The intervertebral fibrocartilages constitute about one-fourth of the length of the vertebral column, taking off the first two vertebrae; but this amount is not equally distributed between the various bones, the cervical and lumbar portions having, in proportion to their length, a much greater amount than the thoracic region, with the result that these parts possess greater pliancy and freedom of movement.

Diarthrodial joints: these are the articulation that permit a large displacement between two bones. The vertebrae are enveloped

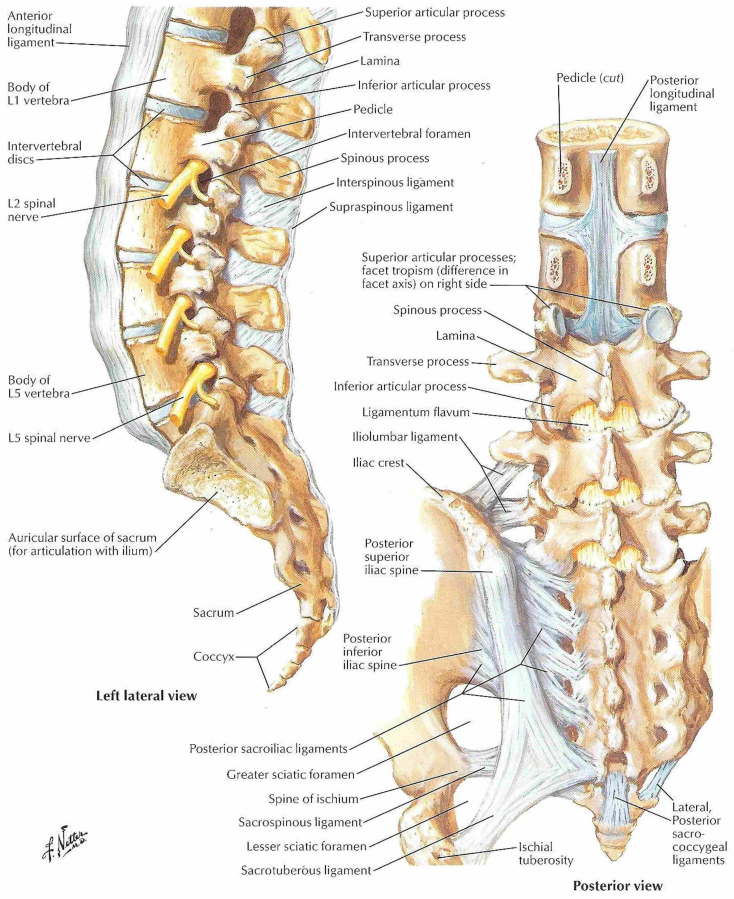

Figure 5: Spine lumbar ligaments. From Netter and Colacino [27]

by capsules lined by synovial membranes, while the laminae, spinous and transverse processes are connected by 5 ligaments:

1. *Ligamenta Flave*: It connect the laminae of adjacent vertebrae, from the axis to the first segment of the sacrum. In the cervical region the ligaments are thin, but broad and long; they are thicker in the thoracic region, and thickest in the lumbar region. Their marked elasticity serves to preserve the upright posture, and to assist the vertebral column in resuming it after flexion.
2. *Ligamentum Nuchae*: it extends from the external occipital protuberance and median nuchal line to the spinous process of the seventh cervical vertebra.
3. *Supraspinal*: this ligament is a strong fibrous cord, which connects together the apices of the spinous processes from the seventh cervical vertebra to the sacrum.
4. *Interspinal*: these ligaments are thin and membranous, connect adjoining spinous processes and extend from the root to the apex of each process. They meet the ligamenta flava

in front and the supraspinal ligament behind. They are narrow and elongated in the thoracic region; broader, thicker, and quadrilateral in form in the lumbar region; and only slightly developed in the neck.

5. *Intertransverse*: they are interposed between the transverse processes. In the cervical region they consist of a few irregular, scattered fibers; in the thoracic region they are rounded cords intimately connected with the deep muscles of the back; in the lumbar region they are thin and membranous.

Part II

MODEL

The second part of the work is dedicated to the presentation and validation of the Finite element spine model as well as the multibody model. Secondly the upper limbs multibody model is presented and coupled with the reduced spine model, using a CMS technique. In the last chapter a scaling procedure of the subjected has been proposed and validated using experimental data.

3

FEM MODEL

In this chapter the FEM model, developed using the software NASTRAN, is described, and the choice of its parameters is explained. A seat model is also proposed. To validate this model a frequency response analysis is performed and the results are compared with the experimental one.

3.1 TOPOLOGY

3.1.1 *Spine model*

A finite element model of a sitting human, for comfort purposes, has been originally developed by the work Kitazaki and Griffin [19], which was based on the previous work of Belytschko and Privitzer [5]. In the Kitazaki and Griffin model the dynamic behavior of the spine is represented section-wise, each section consisting of the corresponding vertebra: 25 vertebral components are taken into account. To them, elements representing the head, buttocks, visceral, masses and pelvic masses, are added. The Kitazaki and Griffin model is limited to the planar behaviour in the sagittal plane, instead the model presented here is able to capture the complete 3D behaviour of the spine: it is a developed version of the model proposed by Tunesi [39]. The model is divided into eight parts:

1. Head
2. Cervical vertebrae: C1,...,C7
3. Thoracic vertebrae: T1,...,T12
4. Lumbar vertebrae: L1,...,L5
5. Sacrum: S1
6. Buttocks
7. Viscerae

The origin of the system is placed in the buttock down point as shown in figure 6. The *x-axis* corresponds to the sagittal axis, the *y-axis* represents the transverse axis and the *z-axis* the longitudinal one.
The center of gravity of each vertebra is associated to a node of the model: henceforth these nodes will be referred to as *vertebral nodes*. To represent the vertebral articulation two coincident nodes were defined and placed between two adjacent vertebrae: henceforth these nodes will be referred to as *intravertebral node*. These nodes are joined

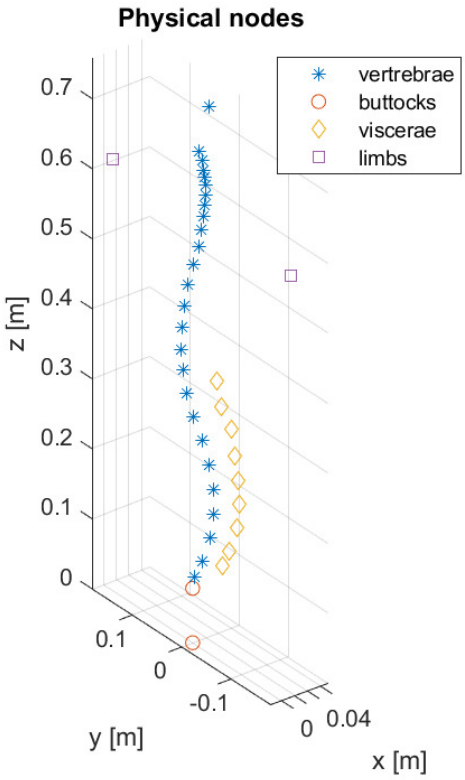

Figure 6: Physical nodes of the model

together by six springs and six dampers acting on each relative degree of freedom in order to have fully 3D model. The approach to use a 6D viscoelastic element was previously used in the work of Valentini and Pennestrì [41]. To link the intravertebra nodes to the vertebral one a rigid element is used: RBE2 in Nastran.
Regarding the visceral part of the model, 7 nodes is defined and placed with an offset in the positive direction of the sagittal axis from the T11 vertebra to the L5. They are linked to the corresponding vertebra by using a rigid element (RBE2): this link constraints the three rotation and the translation along the transverse axis, instead the translation along the longitudinal and the sagittal axis are constrained two dampers and two springs. Moreover, the viscerae are joined together by a spring and a damper that acts in the longitudinal direction. Following the Belytschko and Privitzer [5] idea, two nodes are added with an offset from the T10 and S1 vertebra and linked to this vertebrae through a rigid element (RBE2) that constraints the three rotations and translation.
The upper limbs are linked to the spine, at the T2 vertebra, by using a rigid element. The arms are represented as two point masses.
The buttocks area is composed by 8 nodes placed at the vertices of a two squares having an offset in the longitudinal direction. The nodes with the same coordinates in the sagittal and traversal axis are linked

together by three axial springs and dampers that act in the direction of the three axes. The buttock up nodes and S1 node are joined together by rigid elements. In order to be able to apply a concentrated force at the buttocks down, these node are linked by rigid element to the origin.
Regarding the mass properties of the model, a lumped mass is associated to each node which has a proper offset from the reference vertebra. At the end the FEM model appears as illustrated in figure 7. In table 2 the node locations in the reference configuration are shown,

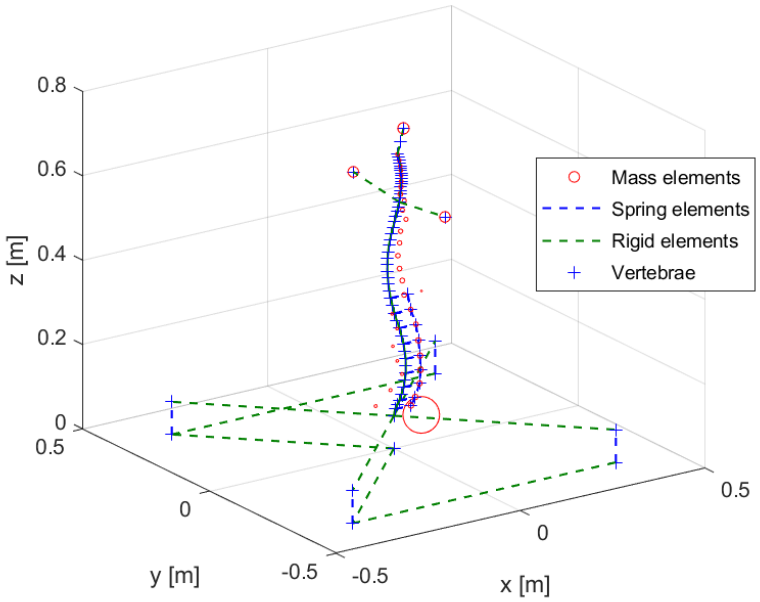

Figure 7: FEM model of the spine: synthetic representation

in table 3 the number of elements present in the model are shown and in table 4 the total number of DOF in the model is calculated.

Nodes	
Vertebral	25
Intravertebral	25
Double intravertebral	25
Head	1
Limbs	2
Buttocks	10
Visceral	9
Total	97

Table 2: Node distribution

Elements	
Spring intravertebra	$6 \cdot 25$
Spring buttock	$3 \cdot 8$
Spring viscerae	8+9
Rigid element vertebrae	$25 \cdot 2$
Rigid element viscerae	9
Rigid element limbs	2
Rigid element buttock	9
Mass element vertebrae	25
Mass element viscerae	8
Mass element head	1
Mass element limbs	2
Damping intravertebrae	$6 \cdot 25$
Damping buttock	$3 \cdot 8$
Damping viscerae	$8 + 9$
Total springs	191
Total rigid	70
Total mass	36
Total dampers	191

Table 3: List of the element used in the FEM model

DOF calculation	
Available	$97 \cdot 6$
Constraints	
Butt down	$4 \cdot 6$
Butt up	$4 \cdot 6$
Vertebrae	$25 \cdot 6 \cdot 2$
Viscerae	$4 \cdot 7 + 6$
Limbs	$2 \cdot 6$
Head	6
Total constraint	417
Dof available	153

Table 4: DOF calculation for the FEM model

3.1.2 *Seat model*

A FEM seat model has been developed in order to interface the spine model with the ground. It is composed by three main elements:

1. Seat
2. Cushion
3. Backrest

The seat and the cushion are modelled as lumped masses, joined together by a spring and a damper, as shown in figure 8. The value for the system are taken according to Choi and Wereley [9]. The connection between the spine and the backrest is performed using a RBE3 element which connects a desired number of vertebrae to a node which is placed with an offset with respect to a specific vertebra. The RBE3 element defines the motion of a reference node as a weighted average of the motion of a set of other nodes. The element is implemented as a set of constraint equations in which the motions of the reference node *REFGRID* are constrained to the motions of the other nodes G_{ij}. This node is connected to a slider through a spring and a damper having the same characteristics of the cushion. The seat data are listed in table 5.

	m_i (kg)	c_i (N s m^{-1})	k_i (kN m^{-1})
Seat	13.5[1]	750.00[1]	22.6[1]
Cushion	1.0[2]	159.00[1]	37.7[1]

Table 5: Numerical values for the seat-cushion model.
[1]From Ref. Choi and Wereley [9]; [2]assumed

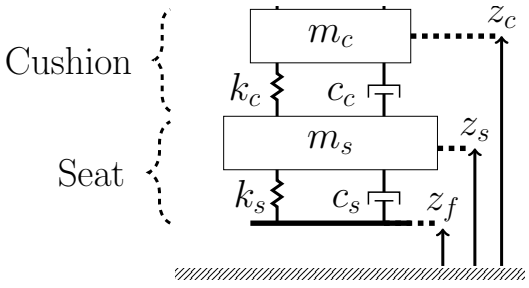

Figure 8: Lumped parameter seat and cushion model

3.2 PARAMETER (FOR REFERENCE SUBJECT)

The parameters refer to a subject which has the following anthropometric characteristics:

- Age: 30 years old
- Stature: 1.80 m
- Weight: 80 kg
- Gender: Male

In table 8 the coordinates of each vertebra, limbs and viscera are reported; these coordinates are used to write the GRID card in NASTRAN. The value are taken from Kitazaki and Griffin [19] model in erect position.
In table 10 the value of the damping used to write the PDAMP card in NASTRAN are reported. The $_{ii}$ subscript refers to the component to which the damping is associated: $\mathbf{c_{11}}$ means that the damper is placed in x direction axially, $\mathbf{c_{22}}$ in y direction and $\mathbf{c_{33}}$ in z direction; $\mathbf{c_{44}}$ means that the a rotational damper acts about the x axis, $\mathbf{c_{55}}$ about y axis and $\mathbf{c_{66}}$ about the z axis. The unit of measurement for the axial damping is $\mathrm{N\,s\,m^{-1}}$, instead for the rotational one the unit of measurement is $\mathrm{N\,m\,s\,rad^{-1}}$.
In table 11 the values used to write the PELSAS card in NASTRAN are reported. The subscripts $_{ii}$ follow the same conventions used for the damping. The unit of measurements are: $\mathrm{N\,m^{-1}}$ for the axial spring and $\mathrm{N\,m\,rad^{-1}}$ for the rotational one. The value are taken from the model of Valentini and Pennestrì [41] for the components $\mathbf{k_{33}}$, $\mathbf{k_{44}}$, $\mathbf{k_{55}}$ and $\mathbf{k_{66}}$; for $\mathbf{k_{11}}$ and $\mathbf{k_{22}}$ a value of 1×10^7 $\mathrm{N\,m^{-1}}$ is assumed, supposing a very stiff link in those directions.
In table 9 the mass properties used to write the CONM2 card in NASTRAN are reported. Column **G** refers to grid point to which the lumped mass is connected, columns $\mathbf{X_1}$, $\mathbf{X_2}$, $\mathbf{X_3}$ express in m the offset in x, y, z direction of the lumped mass respect to the reference grid point **G**. Column **Mass** lists the values in kg of the lumped masses. The columns $\mathbf{I_{11}}$, $\mathbf{I_{22}}$, $\mathbf{I_{33}}$ report in $\mathrm{kgm^2}$ the diagonal terms of the inertia tensor that is associated to each lumped mass; the extra diagonal terms are null.
The parameters identification of this system is a very difficult task. In order to obtain a model that presents modes shapes and FRF as similar as possible to the one found in literature a manual optimization process has been done. In particular the damping values are been modified with respect to the original one presented in Valentini [40] and Valentini and Pennestrì [41]: $\mathbf{c_{44}}$ has been augmented of a value of 10 times, $\mathbf{c_{55}}$ of a value of 4 times, and $\mathbf{c_{33}}$ of a value of 3 times. The most critical and sensible part of the model was the identification of the buttocks parameter: in order to optimize this value the stiffness and damping on the three direction has been varied in order to achieve the best trade-off with the experimental data. The final selected values are the one showed in tables 10 and 11.

3.3 MODEL VALIDATION

In order to validate the model, a modal analysis and a frequency response analysis were performed. The results are then compared with the data available in literature.

3.3.1 *Modal Analysis*

The modal analysis has bee performed using the NASTRAN SOL103: this analysis extracts the eigenvalues and eigenvectors of the system that are requested from the EIGRL card, using the Lanczos algorithm. For the purpose of the work, the range between 0 and 50 Hz is requested, and the mode shapes are then normalized to unit value of the corresponding modal mass. In figures 9 and 10 the firsts eight mode shapes of the spine are plotted and in table 6 the modes are summarized and compared with the model of Kitazaki and Griffin [19] the frequency of the firsts 14 modes. In total, in the requested range, 55 mode are found.

Mode	**Freq. FEM** Hz	**Freq. model** [1] Hz	**Freq. meas.** [2]Hz	**Type**
1	0.39	0.28	1.1	Sym.[3]
2	0.78	-	-	A-sym. [4]
3	1.45	-	-	A-sym.
4	2.41	1.49	2.2	Sym.
5	3.28	-	-	Sym.
6	3.34	2.81	3.4	Sym.
7	3.55	-	-	A-sym.
8	5.21	5.06	4.9	Sym.
9	5.62	-	-	A-sym.
10	5.94	-	-	A-Sym.
11	6.20	5.77	5.6	Sym.
12	9.06	7.51	8.1	Sym.
13	9.73	8.96	8.7	Sym.
14	10.95	-	-	Sym.

Table 6: Mode frequencies of the FEM model, the Kitazaki model, and experimental one

[1]Kitazaki and Griffin [19]
[2]Kitazaki and Griffin [20]
[3]Symmetric: mode that behaves to the sagittal plane
[4]Anti-symmetric: mode that do not behaves to the sagittal plane

3.3.1.1 *Modes description*

The first mode is a fore-and-aft motion of the head and the entire spine with the pelvis caused by a bending deformation of the spine: it corresponds to the first mode of a beam with the lower end fixed; in fact the mass of the pelvis, since it is much higher with respect to the other masses, works as a clamp constraint in this case. The frequency of this mode in our FEM model is close to the one proposed in Kitazaki and Griffin [19]. The second mode is still a bending mode, but in the lateral direction. It is not present in the Kitazaki and Griffin [19] spine since it is a 2D model. The third mode is torsion mode of the spine around the longitudinal axis of z axis in the model reference system. The fourth mode shape lies in the sagittal plane and and corresponds to the second bending mode of a free-end beam. The fifth mode is analogous to the fourth but it lies in the coronal plane. The sixth mode is an axial mode of the buttocks and viscerae. The seventh mode correspond to the second bending mode in the coronal plane of a clamped-free beam. The eight mode is an axial mode of the buttock combined to a bending mode on the sagittal plane of the spine. In figure 9 the first eight mode shape of the FEM model are represented. The frequencies are quite similar to the one reported in Kitazaki and Griffin [19] and [20], even if they are in general a little bit higher.

3.3.2 *Frequency response*

The acceleration transmissibility curves of the buttocks-head channel have been evaluated. The simulation has been performed using the NASTRAN SOL111. The forcing term has been imposed through the SPCD card at the buttock down node, which selects the direction of the forcing term, and through the RLOAD1 and DLOAD card, which impose the kind of the forcing term: for this work an acceleration of 1 m/s^2 has been imposed. The data are then sampled using the the FREQ1 card, spacing the frequency range between 0.1 and 20 Hz, using a resolution of 0.05 Hz, in order to avoid aliasing and to correctly reconstruct the peak of resonance.
The problem that has been solved is the following:

$$\left(-\omega^2 \varphi^T \mathbf{M} \varphi + i\omega \varphi^T \mathbf{B} \varphi + \varphi^T \mathbf{K} \varphi\right) \{\xi(\omega)\} = \varphi^T \{P(\omega)\} \tag{6}$$

where φ are the mode shapes, and $P(\omega)$ is the forcing term in frequency domain. In order to solve this problem a sufficiently rich set of eigenvector has to be chosen: this is done through the PARAM LMODES that permit us to select number of modes used in equation 6. For this work the first 100 modes are selected, which lie in the bandwidth of approximately 0.4 - 100 Hz. The STHT is calculated as the ratio between the cross-spectral-density of the accelerations at the

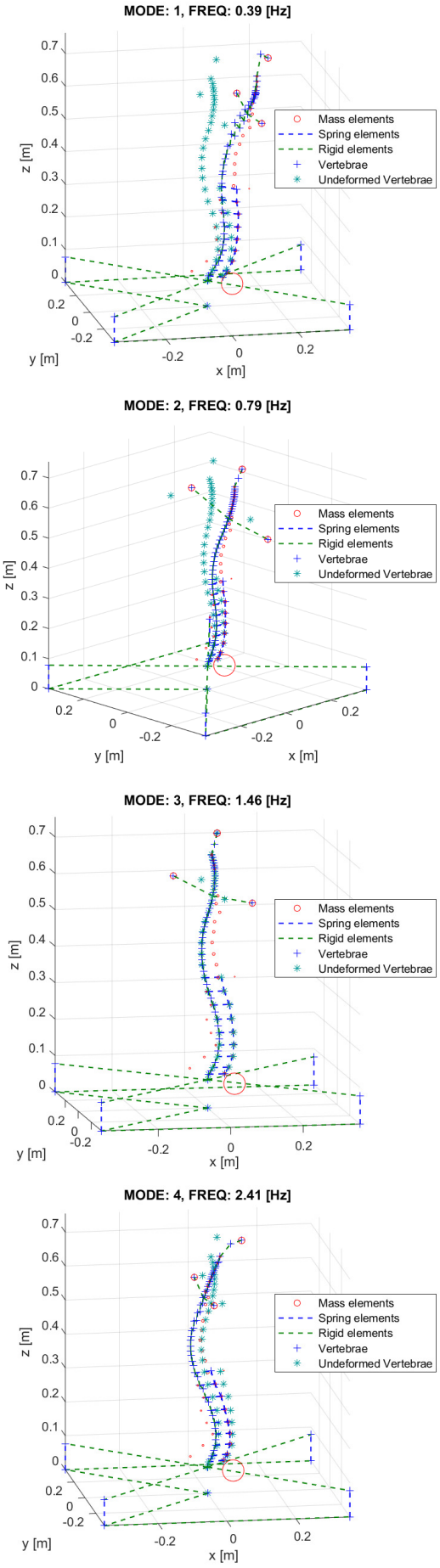

Figure 9: Firsts 4 modes shapes

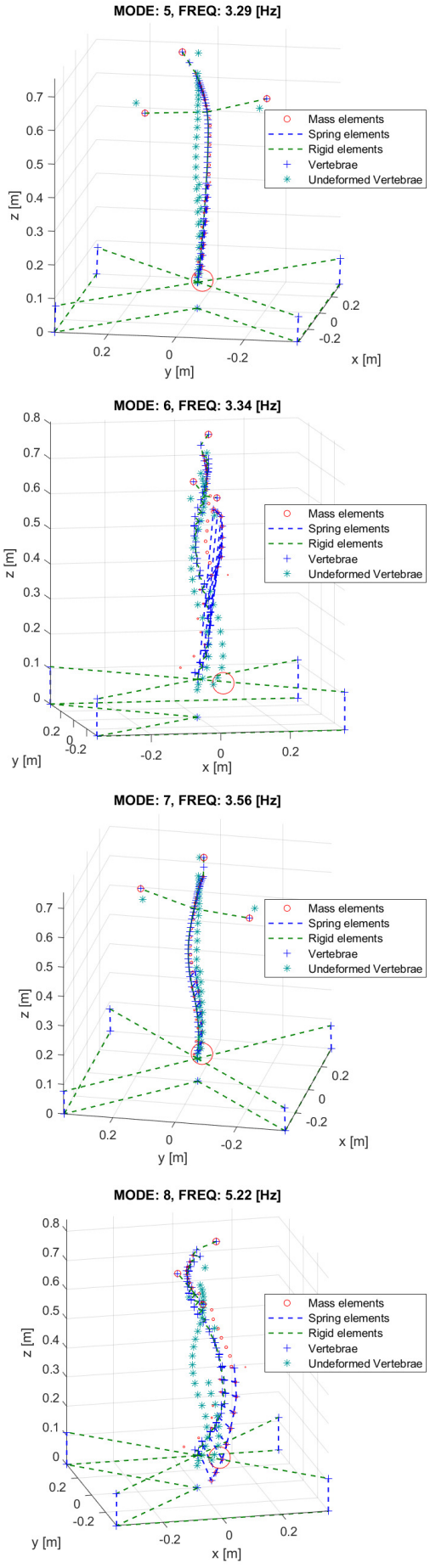

Figure 10: Seconds 4 modes shapes

head A_h and at the buttock down A_b, and the power-spectral-density of the acceleration at the buttock down as shown in equation 7 [1]:

$$H_1 = \frac{A_h \cdot A_b^*}{A_b \cdot A_b^*} \tag{7}$$

From equation 7 a vector of complex number of the size of the sampled frequency is obtained.
Figure 11 shows the frequency response function of the model as a combination of the three translations in input and the three translations in output: index $_i$ of H_{ij} refers to the direction of the input (1 for x axis, 2 for y axis and 3 for the z axis), instead index $_j$ refers to the direction of the output.
The module result are compared with the experimental work of Mandapuram et al. [22] and with the model of Valentini and Pennestrì [41].

3.3.2.1 *FRF discussion*

In the H_{11} graph of figure 11 the FEM model presents a primal peak at 0.62 Hz with a magnitude of 2.1 m/s^2, this resonance can be associated with the first bending mode of the spine. The experimental result of Mandapuram et al. [22] and the model of Valentini and Pennestrì [41] present a smoother shape. The experiment has the primal resonance at peak at 2.8 Hz with a magnitude of 2.6 m/s^2, over 10 Hz the response is almost null. The Valentini and Pennestrì [41] model presents two resonance peaks: the first is at 4 Hz with an amplitude of 1.9 m/s^2, the second is at 12 Hz with an amplitude of 1.1 m/s^2. In this direction the three models are not well correlated, even if at frequency greater than 10 Hz the FEM model and the experimental data are quite similar. However if the backrest is included, as illustrated in figure 12, the model shows a primal resonance peak at 2.83 Hz with an amplitude of 2.28 m/s^2.
In the H_{22} graph of figure 11 the FEM model presents a peak at 1 Hz with an amplitude of 1.98 m/s^2, while in the Mandapuram et al. [22] experiment the primal resonance peak is at 1.65 Hz with an amplitude of 1.96 m/s^2, after this resonance the experiment and the FEM model share the same trend. The Valentini and Pennestrì [41] model presents two peaks: the first at 3.5 Hz and the second at 11.5 Hz with an amplitude of 1.8 m/s^2 and 1.1 m/s^2.
The H_{33} will be analyzed in more detail in paragraph 3.3.4.
The experimental results show a significant coupling when the input is given in the fore-aft direction and the output is measured in the vertical one (H_{13}) . The FEM model is not able to capture this coupling. Other such strong coupling are not present neither in the model neither in the experiment.

1 * is used to indicate the complex conjugate

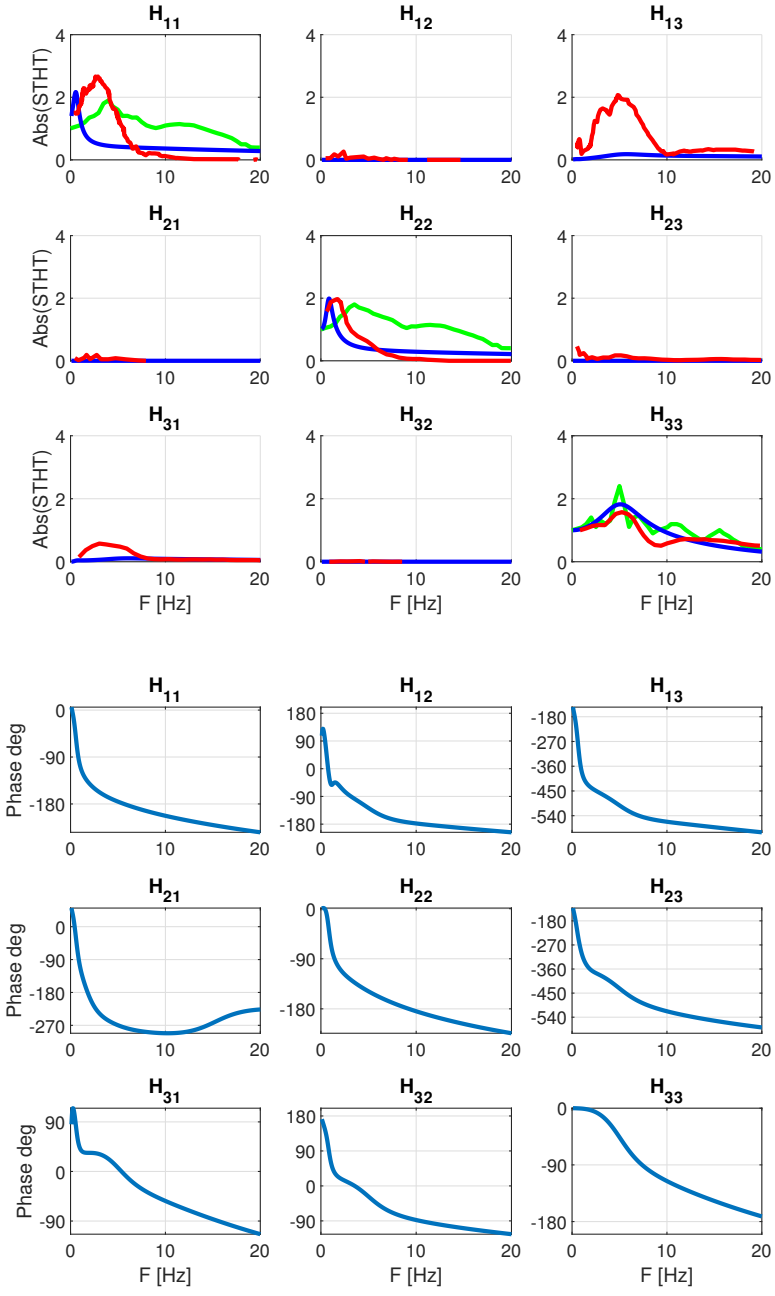

Figure 11: STHT in the three translation. In the module plot in blue are the FEM FRF, in green the Valentini and Pennestrì [41] FRF and in red the Mandapuram et al. [22] FRF

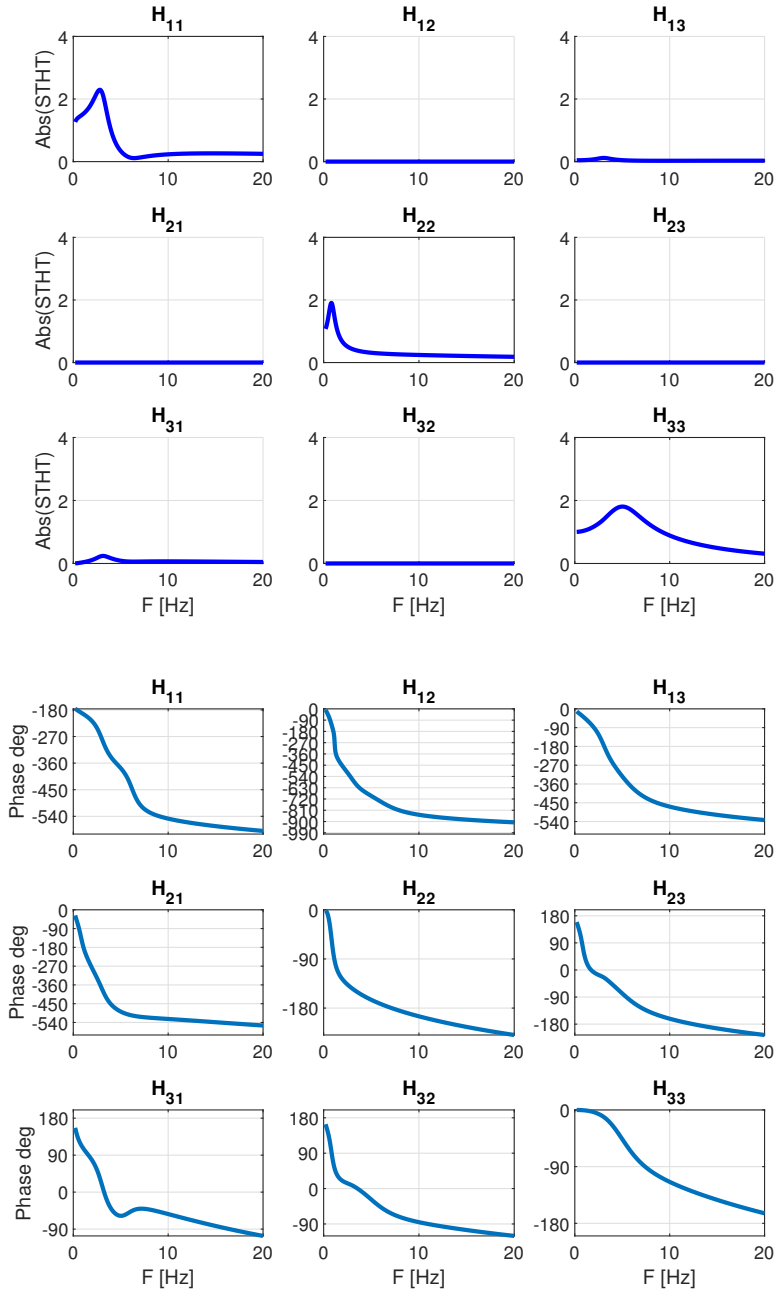

Figure 12: STHT of the FEM model in the three translation including the backrest

3.3.3 *Comparison with with lumped parameters models*

The model has also been compared to some 4 DOF lumped models available in literature. In figure 13(a-b) the $4DOF_{12-6}$ and $4DOF_{14-9}$ are represented, reported in Bai et al. [3] respectively, in figure 13(c) the model of Wan and Schimmels [42] and Abbas [1], and in figure 13(d) the model of Boileau and Rakheja [8] and Zhang E [46]. The parameters of each lumped element, for each model, are reported in 7. In every model the z_0 DOF is the one associated to the floor, to which the forcing term is imposed, instead the z_1 DOF is the one associated the head displacement. In figure 14 is then compared the STHT be-

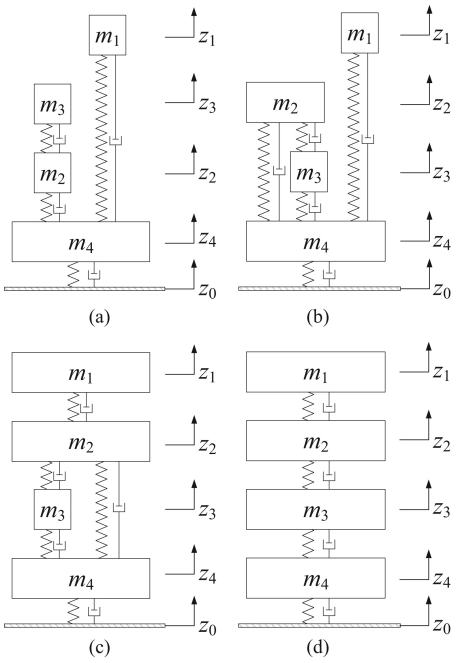

Figure 13: Lumped models, from [3]

tween each lumped parameter models, the FEM model, the Valentini and Pennestrì [41] model, and the experimental results of Mandapuram et al. [22]. It can be observed from figure 14 that the LPM models provide similar levels of acceleration at head. Therefore, all these models are suitable for a LPM biodynamic input. However, among them the Boileau and Rakheja [8] one provides the anthropometric parameters for which the LPM is defined for. Since this parametrization is necessary for the FEM model and also for the multibody one, the Boileau and Rakheja [8] is selected as the reference LPM human biodynamic model. The average of the Boileau-Rakheja experiment population is considered as the target percentile of the population in this work and are given in [8] as:

- Age: 27.3 years old
- Height: 175.7 cm

- Total mass: 75.4kg
- Sitting mass: 55.5 kg

In order to have a more reliable model, the Driving point mechanical impedance (DPMI) and the AM of the FEM model have been compared to the one of the LPM. The DPMI has been calculated as the ratio between the Cross spectral density (CSD) between the force at the buttock down (driving point) F_b and the velocity at the same point V_b, and the Power spectral density (PSD) of the velocity at the buttock down.

$$H_1 = \frac{F_b \cdot V_b^*}{V_b \cdot V_b^*} \tag{8}$$

The AM has been calculated as the ration between the CSD between the force at the buttock down (driving point) F_b and the acceleration at the same point A_b, and the PSD of the acceleration at the buttock down.

$$H_1 = \frac{F_b \cdot A_b^*}{A_b \cdot A_b^*} \tag{9}$$

In 17 the FRF of the lumped models and the FRF of the FEM model between the floor and the head including the seat model described in paragraph 3.1.2 are compared.

3.3.4 *Results discussion*

In figure 14 the STHT of the FEM model is represented compared with the LPM, the Valentini and Pennestrì [41] model, and the experimental result of Mandapuram et al. [22]. The response of the FEM model is quite similar to the lumped model of Boileau and Rakheja [8], which was set as a target model. The other lumped models present a resonance peak highly damped with an amplitude around 1.3 m/s^2), while the experimental results is at 1.5 m/s^2. The FEM model and the Boileau and Rakheja [8] model present the resonance peak at 1.7 m/s^2 while the Valentini and Pennestrì [41] model has the peak at 2.4 m/s^2 and it seems to be not sufficiently damped. All the models agree on the primal resonance frequency around 5 Hz. The Valentini and Pennestrì [41] model presents other secondary resonance peaks that all the other models do not capture. The experiment captures a secondary resonance highly damped at 12 Hz.
In figure 15 the apparent mass of the LPM with the FEM model are compared. The FEM model matches almost perfectly the Boileau and Rakheja [8] model. The amplitude of the apparent mass at resonance around 90 kg for the Boileau and Rakheja [8] and for the FEM model, instead the other models show a maximum around 80 kg. In chapter 5 this parameter will be further analyzed, comparing the module of

the FEM model with the experimental results presented by Toward and Griffin [38].
In figure the DPMI of the LPM and of the FEM model are compared. The systems behaves as a second order model with a maximum transmitted force around 5 Hz of 3000 $N\,s\,m^{-1}$ for the FEM model, the other models have lower peak modules. Also in this case the closest model is the Boileau and Rakheja [8].
In figure 17 the STHT of the LPM and the FEM models including the seat model are compared. In order to better visualize the differences in the module the semi-logarithmic scale has been chosen[2]. In this case all the models present almost identical responses meaning that the dynamic of the seat plays an important role on the dynamic of system. The primal resonance frequency is at 2.1 Hz with a magnitude of 3.5 m/s^2.

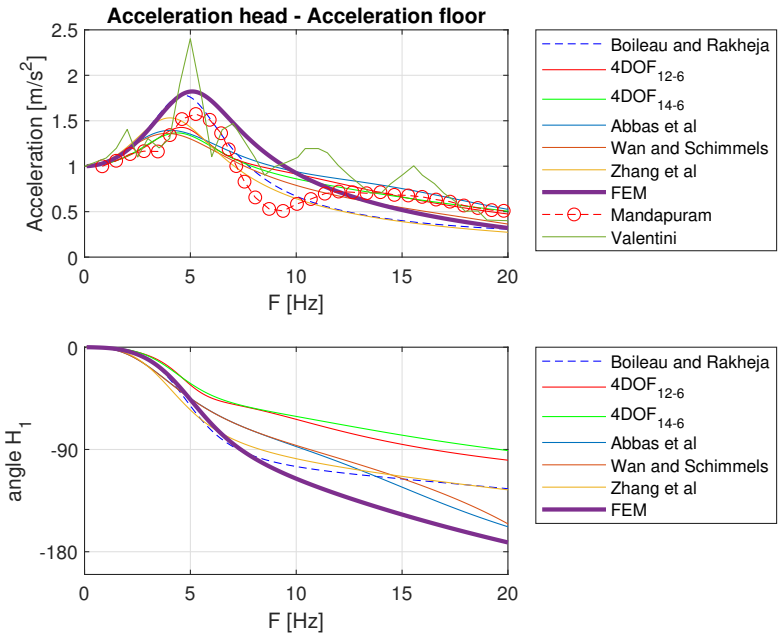

Figure 14: Seat to head transmissibility in vertical direction

2 In the other plots a linear scale has been used to be coherent with the works [22], [41] and [3]

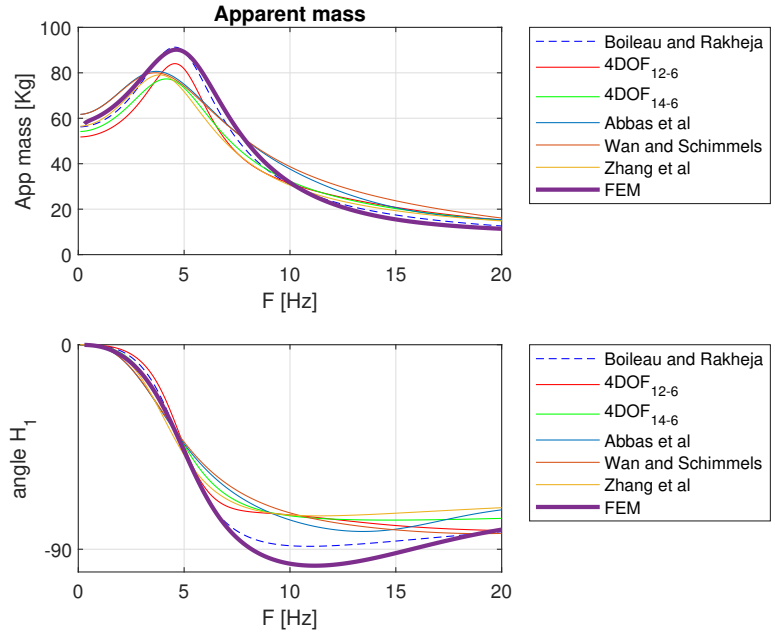

Figure 15: Apparent mass comparison

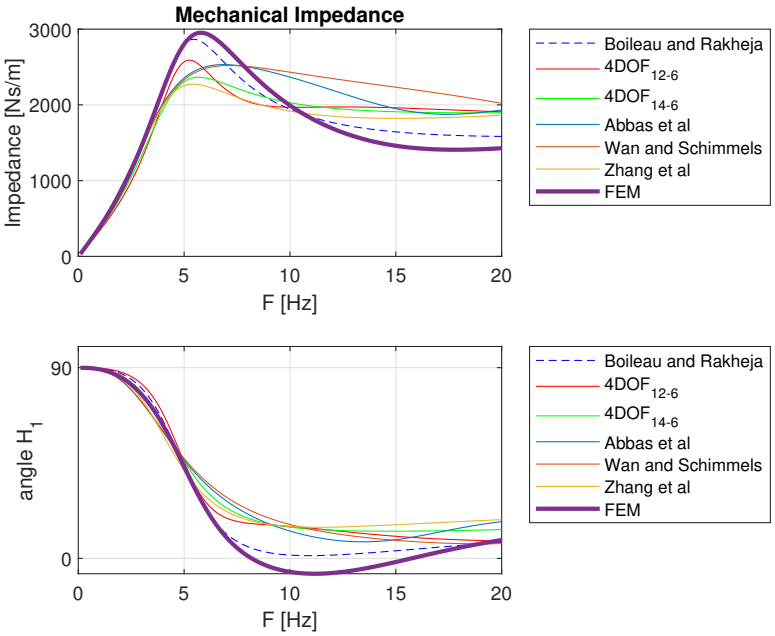

Figure 16: Mechanical impedance comparison

Model	**Stiffness**						kN m^{-1}
	k12	k23	k34	k40	k13	k14	k24
4DOF 12-6	-	31.24	-	120.7	-	18.67	41.52
4DOF 14-6	-	22.74	20.41	92.75	-	59.19	22.28
Abbas et al.	167	10	20	49.34	-	-	144
Boileau and Rakhjea	-	183	-	90	310	-	162.8
Wan and Schimmels	134.4	10	20	49.34	-	-	192
Zhang et al.	-	150.1	-	70.04	310	-	111.5
	Damping						N s cm^{-1}
	c12	c23	c34	c40	c13	c14	c24
4DOF 12-6	-	8.37	-	18.5	-	11.94	9.564
4DOF 14-6	-	18.51	8.456	23.58	-	9.497	8.619
Abbas et al.	3.1	2	3.3	24.75	-	-	9.091
Boileau and Rakhjea	-	47.5	-	20.64	4	-	45.85
Wan and Schimmels	2.5	2	3.3	24.75	-	-	9.091
Zhang et al.	-	40	-	26.98	40	-	40
	Mass			kg			
	m1	m2	m3	m4			
4DOF 12-6	6.184	10.76	12.65	21.16			
4DOF 14-6	6.142	8.578	20.59	17.79			
Abbas et al.	4.17	15	5.5	36			
Boileau and Rakhjea	5.31	28.49	8.62	12.78			
Wan and Schimmels	4.17	15	5.5	36			
Zhang et al.	5.31	24.14	10.45	15.6			

Table 7: Lumped models parameters, from Bai et al. [3]

Label	ID	X m	Y m	Z m
Head	1	0.02617	0.00000	0.75375
C1	2	0.01000	0.00000	0.69528
C2	3	0.01456	0.00000	0.68031
C3	4	0.01751	0.00000	0.66619
C4	5	0.01898	0.00000	0.65527
C5	6	0.01987	0.00000	0.64323
C6	7	0.02001	0.00000	0.62968
C7	8	0.01934	0.00000	0.61617
T1	9	0.01748	0.00000	0.59953
T2	10	0.01430	0.00000	0.58151
T3	11	0.00918	0.00000	0.56034
T4	12	0.00187	0.00000	0.53674
T5	13	-0.00672	0.00000	0.51145
T6	14	-0.01325	0.00000	0.48395
T7	15	-0.01695	0.00000	0.45476
T8	16	-0.01754	0.00000	0.42330
T9	17	-0.01514	0.00000	0.39346
T10	18	-0.00895	0.00000	0.35826
T11	19	0.00153	0.00000	0.31999
T12	20	0.01488	0.00000	0.28235
L1	21	0.02629	0.00000	0.24275
L2	22	0.03220	0.00000	0.20571
L3	23	0.03247	0.00000	0.17166
L4	24	0.02691	0.00000	0.13996
L5	25	0.01481	0.00000	0.11020
S1	26	0.00331	0.00000	0.09246
Butt down	27	0.00000	0.00000	0.00000
Butt up	28	0.00000	0.00000	0.07735
L_{arm}	63	0.01430	0.18114	0.59953
R_{arm}	64	0.01430	-0.18114	0.59953
T10V	46	0.03788	0.00000	0.35826
T11V	47	0.04584	0.00000	0.31999
T12V	48	0.06000	0.00000	0.28235
L1V	49	0.06646	0.00000	0.24275
L2V	50	0.07120	0.00000	0.20571
L3V	51	0.07255	0.00000	0.17166
L4V	52	0.06971	0.00000	0.13996
L5V	53	0.05801	0.00000	0.11020
S1V	54	0.04651	0.00000	0.09246

Table 8: Grid point coordinates of the FEM model

G	Mass	X_1	X_2	X_3	I_{11}	I_{22}	I_{33}
1	4.33	0.0000	0	0.0000	0.0225	0.0215	0.0262
2	0.78	0.0000	0	0.0000	0.0007	0.0006	0.0012
3	0.78	0.0000	0	0.0000	0.0007	0.0006	0.0012
4	0.78	0.0000	0	0.0000	0.0007	0.0006	0.0012
5	0.78	0.0000	0	0.0000	0.0007	0.0006	0.0012
6	0.78	0.0000	0	0.0000	0.0007	0.0006	0.0012
7	0.87	0.0000	0	0.0000	0.0010	0.0006	0.0016
8	1.15	0.0000	0	0.0000	0.0033	0.0007	0.0041
9	1.31	0.0000	0	0.0000	0.0049	0.0007	0.0161
10	1.03	0.0136	0	0.0000	0.0096	0.0019	0.0115
11	1.12	0.0136	0	0.0000	0.0011	0.0027	0.0133
12	1.02	0.0311	0	0.0000	0.0010	0.0029	0.0127
13	1.13	0.0252	0	0.0000	0.0108	0.0036	0.0139
14	1.15	0.0291	0	0.0000	0.0109	0.0041	0.0145
15	1.26	0.0283	0	0.0000	0.0114	0.0050	0.0155
16	1.28	0.0325	0	0.0000	0.0113	0.0052	0.0156
17	1.36	0.0385	0	0.0000	0.0115	0.0058	0.0161
18	1.30	0.0367	0	0.0000	0.0106	0.0056	0.0154
19	0.31	-0.0064	0	0.0000	0.0003	0.0012	0.0003
20	0.32	-0.0056	0	0.0000	0.0003	0.0012	0.0003
21	0.27	-0.0294	0	0.0000	0.0005	0.0010	0.0006
22	0.33	-0.0225	0	0.0000	0.0006	0.0012	0.0007
23	0.42	-0.0102	0	0.0000	0.0006	0.0014	0.0008
24	0.54	-0.0358	0	0.0000	0.0009	0.0013	0.0012
25	0.45	-0.0639	0	0.0000	0.0005	0.0009	0.0008
26	16.23	0.0712	0	-0.0279	0.0872	0.1324	0.1076
46	0.00	0.0367	0	0.0000	0.0000	0.0000	0.0000
47	1.23	0.0000	0	0.0000	0.0113	0.0048	0.0160
48	1.29	0.0000	0	0.0000	0.0121	0.0048	0.0157
49	1.61	0.0000	0	0.0000	0.0142	0.0055	0.0179
50	1.61	0.0000	0	0.0000	0.0153	0.0057	0.0181
51	1.65	0.0000	0	0.0000	0.0151	0.0056	0.0172
52	1.56	0.0000	0	0.0000	0.0151	0.0039	0.0177
53	1.71	0.0000	0	0.0000	0.0163	0.0035	0.0200
54	1.64	0.0000	0	0.0000	0.0009	0.0009	0.0009
63	4.01	0.0000	0	0.0000	0.0000	0.0000	0.0000
64	4.00	0.0000	0	0.0000	0.0000	0.0000	0.0000

Table 9: Mass properties of the FEM model

Bushing	c_{11}	c_{22}	c_{33}	c_{44}	c_{55}	c_{66}
Head-C1	2.50E+08	2.50E+08	15570	560	336	119
C1-C2	2.50E+08	2.50E+08	5870	360	216	77
C2-C3	2.50E+08	2.50E+08	8915	110	64	23
C3-C4	2.50E+08	2.50E+08	9345	120	72	26
C4-C5	2.50E+08	2.50E+08	9205	130	76	27
C5-C6	2.50E+08	2.50E+08	10190	150	88	31
C6-C7	2.50E+08	2.50E+08	10515	170	104	37
C7-T1	2.50E+08	2.50E+08	15025	280	168	60
T1-T2	2.50E+08	2.50E+08	13900	220	132	47
T2-T3	2.50E+08	2.50E+08	16770	290	172	61
T3-T4	2.50E+08	2.50E+08	19225	360	216	77
T4-T5	2.50E+08	2.50E+08	22190	460	272	97
T5-T6	2.50E+08	2.50E+08	22035	480	284	101
T6-T7	2.50E+08	2.50E+08	21450	480	284	101
T7-T8	2.50E+08	2.50E+08	16545	400	240	85
T8-T9	2.50E+08	2.50E+08	15775	400	240	85
T9-T10	2.50E+08	2.50E+08	16300	420	248	88
T10-T11	2.50E+08	2.50E+08	16865	450	268	95
T11-T12	2.50E+08	2.50E+08	7995	190	116	41
T12-L1	2.50E+08	2.50E+08	8915	190	112	40
L1-L2	2.50E+08	2.50E+08	9005	170	104	37
L2-L3	2.50E+08	2.50E+08	9735	190	116	41
L3-L4	2.50E+08	2.50E+08	11075	220	132	47
L4-L5	2.50E+08	2.50E+08	12050	230	140	50
L5-S1	2.50E+08	2.50E+08	35400	270	164	58
Butt front	75567	1700	567	0	0	0
Butt rear	75567	1700	567	0	0	0

Table 10: Damping values of the FEM model

Bushing	K_{11}	K_{22}	K_{33}	K_{44}	K_{55}	K_{66}
Head-C1	1E+10	1E+10	565573.7	399.1	419.1	51.1
C1-C2	1E+10	1E+10	308494.8	399.1	942.9	51.1
C2-C3	1E+10	1E+10	719821.1	389.2	83.8	92.0
C3-C4	1E+10	1E+10	781520.1	429.1	104.8	122.7
C4-C5	1E+10	1E+10	816482.8	479.0	125.7	143.2
C5-C6	1E+10	1E+10	994381.5	578.8	167.6	184.1
C6-C7	1E+10	1E+10	1042712.3	608.7	230.5	204.6
C7-T1	1E+10	1E+10	1371773.4	838.2	387.6	296.6
T1-T2	1E+10	1E+10	719821.1	440.0	146.7	143.2
T2-T3	1E+10	1E+10	1233979.1	726.4	293.4	214.8
T3-T4	1E+10	1E+10	1542473.9	852.2	440.0	286.4
T4-T5	1E+10	1E+10	2159463.4	1264.3	733.4	429.6
T5-T6	1E+10	1E+10	1953800.2	1173.5	733.4	429.6
T6-T7	1E+10	1E+10	1850968.6	1131.6	733.4	429.6
T7-T8	1E+10	1E+10	1542473.9	1110.6	733.4	429.6
T8-T9	1E+10	1E+10	1542473.9	1229.3	806.7	501.2
T9-T10	1E+10	1E+10	1542473.9	1348.1	806.7	501.2
T10-T11	1E+10	1E+10	1542473.9	1704.3	880.1	572.8
T11-T12	1E+10	1E+10	1542473.9	1634.5	733.4	715.9
T12-L1	1E+10	1E+10	1850968.6	1585.6	660.0	859.1
L1-L2	1E+10	1E+10	2190312.9	1536.7	660.0	859.1
L2-L3	1E+10	1E+10	2056631.8	1508.7	660.0	859.1
L3-L4	1E+10	1E+10	2056631.8	1529.7	660.0	859.1
L4-L5	1E+10	1E+10	1922950.7	1264.3	586.7	787.5
L5-S1	1E+10	1E+10	1511624.4	1096.6	73.3	644.3
Butt front	3022683.2	22670.1	22670.1	0.0	0.0	0.0
Butt rear	3022683.2	22670.1	22670.1	0.0	0.0	0.0

Table 11: Stiffness value for the FEM reference model

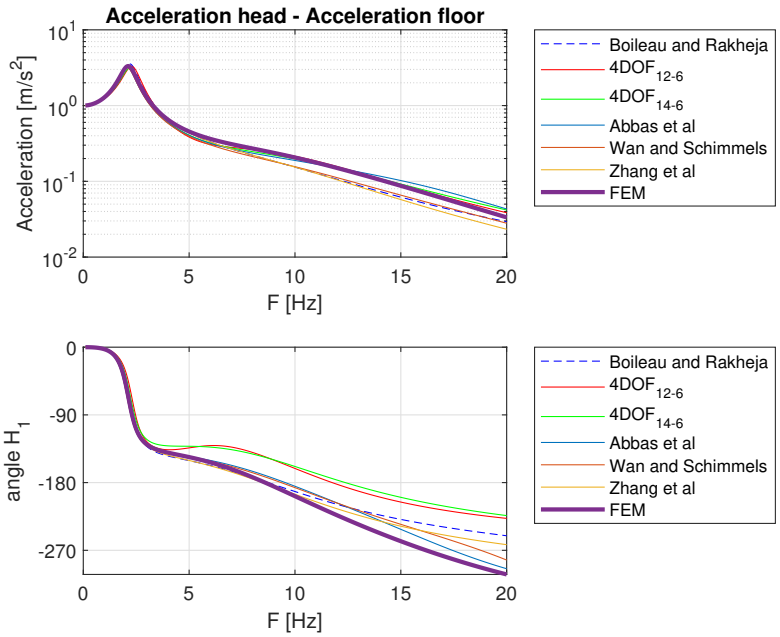

Figure 17: Floor to head trasmissibility, including the seat model

Viscerae	K_{33}	C_{33}
T10V-T11V	29409.8	2941.0
T11V-T12V	26941.8	2694.2
T12V-L1V	24885.2	2488.5
L1V-L2V	23034.2	2303.4
L2V-L3V	19640.8	1964.1
L3V-L4V	16864.3	1686.4
L4V-L5V	17275.7	1727.6
L5V-S1V	13265.2	1326.5

Table 12: Visceral parameters: stiffness and damping

4 MULTIBODY MODEL

In this chapter will be shown first the multibody model of the spine, using the free software MBDyn, second it is presented the upper limb multibody model developed by Ing. Zanoni and third it is explained how the the FEM model is reduced and linked to the upper limb model using a Craig and Bamptom approach.

4.1 INTRODUCTION TO MBDYN

MBDyn[1] is the first and possibly the only free[2] general purpose Multibody dynamics analysis software released under GNU's GPL 2.1. It has been developed at the *Dipartimento di Scienze e Tecnologie Aerospaziali* of the *Politecnico di Milano*.
MBDyn features the integrated multidisciplinary simulation of multibody, multi-physics systems, including nonlinear mechanics of rigid and flexible bodies (component mode synthesis elements, lumped elements) subjected to kinematic constraints, along with smart materials, electric networks, active control, hydraulic networks and essential fixed wing and rotorcraft aerodynamics.

4.2 SPINE MODEL

4.2.1 *Topology*

The MBDyn spine model uses the same philosophy adopted for the development of the spine FEM model. It follows the idea proposed by Kitazaki and Griffin [19] for a model that only allows motion in sagittal plane. The model has been transformed back into a three dimensional one using as starting reference the database provided by Privitzer and Belytschko [30] and Valentini and Pennestrì [41].
The model includes 34 rigid bodies associated with the section of the trunk corresponding to each vertebra from C1 to S1, and to 8 visceral masses. The relative displacements between each vertebral node is allowed only in the local z direction, assumed to lie in the local tangent direction to the spine axis. Instead the relative displacement in the x direction, which corresponds to the anatomical antero-posterior direction, and in the y direction, which corresponds to the anatomical medio-lateral direction, are constrained: the FEM model instead allows the motion in x and y direction, but the vertebrae in these di-

1 http://www.mbdyn.org/
2 https://www.gnu.org/philosophy/free-sw.html

rection are connected by very stiff spring (10^7 N m^{-1}).
As in the FEM model, the vertebrae are interconnected by linear viscoelastic elements, acting on all the remaining, unconstrained degrees of freedom. The visceral masses are connected to the corresponding vertebrae: from T11 to S1, and between them, through linear viscoelastic element. As in the FEM model, the other lumped masses are placed in correspondence to centers of the shoulder girdles, of the pelvis and of the head. For what concerns the buttocks, this area is modelled adding a mass and a viscoelastic element. As in the FEM model, the last vertebra S1 of the spine is connected to the cushion surface by viscoelastic elements representing the buttocks tissue. The node representing the buttock degree of freedom is constrained as to allow only the vertical relative displacement with respect to S1 and the rotation in the sagittal and coronal plane. Before constraints are enforced

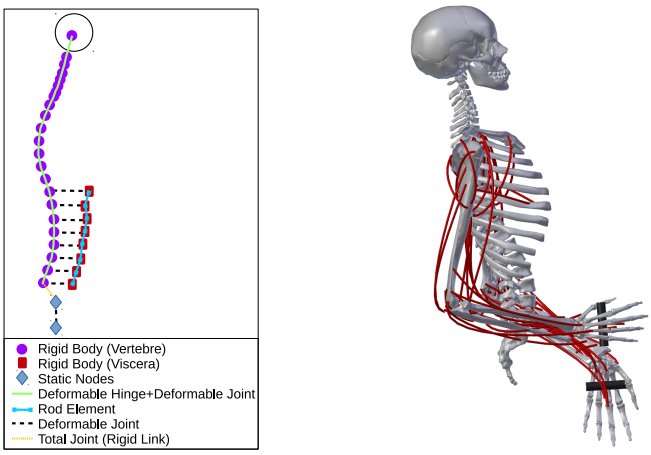

Figure 18: The multibody model

the total number of DOF is 228. After applying the constraining, the model has 103 DOF, fifty less than the FEM model: this is due to the fact that in the MBD model the intravertebra nodes are constrained in the x and y translational direction, instead in the FEM this constrain is simulated with 2 highly stiff springs and dampers. These modeling choices are motivated by the anatomical traits of the intervertebral joints: the posterior processes of the vertebrae are connected via the *facet joint*, a synovial plane joint that allow for almost null relative displacement between the facet of the joint, thus constraining almost completely the relative displacement of the vertebrae in the transverse plane.
In order find the reference position of the spine an inverse kinematic analysis is needed: the pose of the spine is determined in relation with imposed position of head and buttocks: the head is placed over C1 in order simulate that the subject is looking ahead. Since the problem is undetermined a set of dummy springs is introduced: they act as penalty coefficients for the motion of the relative DOF. For the purpose of this work the muscular fascicles are not modelled in detail

neither in the MBD model neither in the FEM model, but their presence is replaced by the generic linear viscoelastic elements. The pre-strain of each viscoelastic element is determined by the relative position of each vertebra.

4.2.2 *Inverse kinematics analysis*

As mentioned before, the spine problem is highly undetermined: it has 103 DOF but only the 6 of the head are imposed, so the 97 DOF are free. In order to solve the problem the procedure proposed in Masarati, Quaranta, and Zanoni [24] is followed. This problem has n kinematic variables that prescribes b kinematic parameters by means of c actuators, with $c > b$. The algebraic constraint representing the passive constraint of the system $n - c$ are written as:

$$\phi(q) = 0 \tag{10}$$

The $b = 6$ rehomic constraints that prescribe the position of the head are written as:

$$\psi(q) = \alpha(t) \tag{11}$$

The DOF of the constrained system when the motion of the head is not prescribed are $n - m = 103$, where m is the number of scleronomic constraints, and they can be collected in a vector θ:

$$\theta = \theta(q) \tag{12}$$

They represent the motor degrees of freedom. At the velocity level, equation 12 can be formally inverted, leading to:

$$\dot{q} = \theta^{+}_{/q}\dot{\theta} \tag{13}$$

The inverse is indicate as $\theta^{+}_{/q}$ because it is a pseudo-inverse matrix that has to be used since the problem is undetermined. The resulting motion intrinsically complies with the passive constraints:

$$\phi_{/q}\dot{q} = \phi_{/q}\theta^{+}_{/q}\dot{\theta} = 0 \qquad \forall\dot{\theta} \tag{14}$$

Which implies:

$$\phi_{/q}\theta^{+}_{/q} = 0 \tag{15}$$

In order to solve the kinematic undetermination the procedure proposed by Fumagalli, Gaias, and Masarati [13] is followed. A set of dummy spring are placed on the unconstrained DOF. The equilibrium configuration is found in the condition of minimum potential energy of the springs. The introduction of these ergonomic sprigs lead, using Lagrange multipliers, to the minimization of a cost function $J(x)$:

$$J(q) = W(\theta - \theta_{ergo}) + \lambda^{T}\Psi + \mu^{T}(\psi - \alpha) \tag{16}$$

where θ represents the generic joint space coordinate associated with a generic articular function. The intermediate position of the joint is considered to represent the ergonomic position.

$$\theta_{ergo} = \frac{\theta_{max} - \theta_{min}}{2} \tag{17}$$

The condition of minimum potential energy of the springs corresponds to an ergonomic solution of the problem. At the position level, the problem is the following:

$$\theta_{/q}{}^{T} K(\theta - \theta_{ergo}) + \phi_{/q}^{T}\lambda + \psi_{/q}^{T}\mu = 0 \tag{18}$$

$$\phi = 0 \tag{19}$$

$$\psi = \alpha \tag{20}$$

For the velocity and acceleration, analogous functions can be written. In the velocity case, this function minimizes the difference between velocity and the corresponding estimated value $\dot{q}_0$ obtained from the numerical differentiation of position. For the acceleration case, the reference value $\ddot{q}_0$ is obtained from the differentiation of velocity. In both cases the mass matrix $\mathbf{M}$ is used for weighting. Regarding the velocity:

$$f'(\dot{q}) = \frac{1}{2}(\dot{q} - \dot{q}_0)^{T} M(\dot{q} - \dot{q}_0) + \lambda'^{T}\phi_{/q}\dot{q} + \mu'^{T}(\psi_{/q}\dot{q} - \dot{\alpha}) \tag{21}$$

which yields to:

$$M(\dot{q} - \dot{q}_0) + \phi_{/q}^{T}\lambda' + \psi_{/q}^{T}\mu' = 0 \tag{22}$$

$$\phi_{/q}\dot{q} = 0 \tag{23}$$

$$\psi_{/q}\dot{q} = \dot{\alpha} \tag{24}$$

Regarding the acceleration:

$$f''(\ddot{q}) = \frac{1}{2}(\ddot{q} - \ddot{q}_0)^{T} M(\ddot{q} - \ddot{q}_0) + \lambda''^{T}(\phi_{/q}\dot{q} + (\phi_{/q}\dot{q})_{/q}\dot{q}) \tag{25}$$

$$+ \mu''^{T}(\psi_{/q}\ddot{q} + (\psi_{/q}\dot{q})_{/\dot{q}} - \ddot{\alpha}) \tag{26}$$

which yields to:

$$M(\ddot{q} - \ddot{q}_0) + \phi_{/q}^{T}\lambda'' + \psi_{/q}^{T}\mu'' = 0 \tag{27}$$

$$\phi_{/q}\ddot{q} = -(\phi_{/q}\dot{q})_{q}\dot{q} \tag{28}$$

$$\psi_{/q}\ddot{q} = \ddot{\alpha} - (\psi_{/q}\dot{q})_{/q}\dot{q} \tag{29}$$

4.2.3 *Parameters (for reference subject)*

The model uses the same parameter used for the FEM model listed in 3, regarding the intravertebral springs and dampers, the masses with the relative inertial properties. The only relevant difference is

the buttocks stiffness. For the MBD model the vertical stiffness, for the reference subject is 58.8 $\mathrm{kN\,m^{-1}}$ and a proportional damping factor of 0.025 is introduced. The resulting damping is 1.47 $\mathrm{kN\,s\,m^{-1}}$. The rotational stiffness around the x axis and the y axis is equal to 7.40 $\mathrm{kN\,m\,rad^{-1}}$, and the same proportional damping factor used for the vertical direction is applied, resulting in an isotropic rotational damping of 0.185 $\mathrm{kN\,m\,s\,rad^{-1}}$.

4.3 UPPER LIMB MODEL

The multibody model of the upper limbs was developed by Zanoni [44] based on the work of Pennestrì et al. [29] and subsequently improved by Masarati, Quaranta, and Zanoni [25]. Each limb is composed of four rigid bodies that represent the humerus, the radius the ulna and the hand. They are joined together by ideal kinematic constraints, using the MBDyn cards *total joint* and *spherical hinges*. The total number of degree of freedom is then $6 \cdot 4 = 24$. The hand is represented by a single body: this simplification was made because the target simulations involve only grasping tasks.
The shoulder complex is not modeled in detail, disregarding the clavicle and the scapula. In fact piloting tasks are typically performed with very low elevation angles of the humerus for both the limbs; therefore the expected effect of the scapula and clavicle motion on the shoulder kinematics is very limited.
The glenohumeral joint is represented by a spherical joint located at the glenoid fossa, removing 3 degrees of freedom: since the rotation are not transmitted from the spine to arms, thanks to the spherical joint, the inertia tensor of the arm was not included in the arm body part of the spine model, but only the mass was included.
A revolute hinge represents the humeroulnar joint in correspondence to the center of the trochlea, allowing the rotation of the ulna with respect to the humerus only about the local lateral axis: this removes 5 degrees of freedom. The humereroradial joint is represented by a spherical hinge, located at the humeral capitulum: it removes 3 degrees of freedom. The proximal and distal radioulnar joints are modeled by single inline joint between a point P and the mechanical axis of the ulna. The position of the point is offset from the radius mechanical axis in the lateral direction: the offset is such as to leave the two bones' mechanical axes parallel in the rest position: the arm are extended anteriorly and the palm are facing upward. This joint removes 2 degrees of freedom. At its distal end, the radius connects with the hand by means of a cardanic joint, allowing the wrist radioulnar deviation and flexion-extension rotations: this joint is composed by two simple hinges which have the axis rotated by 90°. It removes 4 more degree of freedom. At the end the model has 7 degrees of freedom and its kinematics are underdetermined even if the motion is com-

pletely prescribed.
For this model a muscle card was developed based on the simplified Hill muscles model, described in Pennestrì et al. [29]. The force exerted by a muscle is a function of the muscle deformation $x = l/l_0$, its normalized velocity $v = \dot{l}/v_0$ and a voluntary activation a:

$$f = f_0[f_1(x)f_2(v)a + f_3(x)] \tag{30}$$

where f_0 is the peak isometric contraction force exerted by the muscle, l_0 represents the length at which f_0 is produced, while v_0 is the maximum contraction velocity of the muscle. This reference value are taken from Holzbaur, Murray, and Delp [15].
Moreover

$$\begin{aligned} f_1 &= e^{[-40(x-0.95)^4+(x-0.95)^2]} \\ f_2 &= 1.6 - 1.6^{\left[\frac{-1.1}{(-v+1)^4}+\frac{0.1}{(-v+1)^2}\right]} \\ f_3 &= \arctan[0.1(x-0.22)^{10}] \end{aligned} \tag{31}$$

For each limb 25 muscles were modeled. So the model is underconstrained (it has 7 degree of freedom) and overactuated since we have 25 muscles acting on 7 degrees of freedom. The muscular activation is a-priori unknown for a given task because it depends, among other parameters, on the strategy of the nervous control system. In order to estimate the activation of each muscle for a given task a non-linear optimization problem is solved at each step: the total squared activation is minimized in a given configuration, under the constraint that the torques produced by the muscles must be equal to the ones required to guarantee the dynamic equilibrium of the limb and compliance with the bound: $0 \leqslant a_i \leqslant 1$.

$$\min \sum_{i=1}^{n_m} a_i^2 \qquad \text{where } n_m \text{ is the total number of muscle bundles} \tag{32}$$

This contribution to the total activation goes to the *passive* or *involuntary* characteristics of the pilot. The *active* or *reflexive* part of the muscular activation is estimated considering a quasi-steady approximation:

$$\Delta a = K_p \Delta x + K_d \Delta v \tag{33}$$

and the force perturbation can be expressed as:

$$\Delta f = f_0[(f_{1/x}a + f_1 K_p)f_2 + f_{3/x}]\Delta x + f_0 f_1 (f_{2/v}a + f_2 K_d)\Delta v \tag{34}$$

The upper limb model is used to perform a cascaded analysis:

- An *inverse kinematic analysis*: it is needed to determine the configuration of the arm for tasks prescribed to the hand. It basically takes the hand from the position, in which the model is assembled, to the cyclic and collective levers.

- An *inverse dynamic analysis*: it determines the joint torques required to perform the specified tasks.
- The solution of the non-linear optimization problem needed to determine the activation pattern required to produce the required torques for each configuration.
- A singular value decomposition used to determine the activation modes that do not alter the joint torques produced by the muscles.

In Masarati, Quaranta, and Zanoni [24] the complete solution strategy is explained in greater detail.

4.4 CONNECTING TORSO AND UPPER LIMB

In order to connect the upper limb model to the seated spine model in MBDyn a modal reduction of the spine model has been performed.

4.4.1 *Reduced model*

The modal reduction of the FEM spine model is performed using the *boundary masses* approach proposed by Karpel and Raveh [18] which derives from the sub-structuring method developed by Bampton and Craig Jr [4].
To be able to apply the *boundary masses* method, first the backrest of the spine model has been simulated by using a large mass instead of the slider constraint built using the SPC card. The mass was attached at the REFGRID of the REB3 element: the viscoelastic element representing the backrest cushion has been removed as well as the bottom part of the seat (the one that connects the buttock down to the ground). The buttock down is clamped in the ground using the SPC card. Both seat and backrest will be then modelled in MBDyn. In order to verify that the mass is able to constrain the backrest as well as the SPC, two modal analysis were performed using the SOL 103 of Nastran: one using the SPC constraint and one using the boundary mass. It turns out that a mass of 1000 kg, inserted with the CONM2 card, is sufficient to preserve the frequencies of the flexible modes of the spine.
The parameters needed to generate the reduced model are then extracted by Nastran through the usage of the ALTER file that is provided in the MBDyn package. This file runs a eigneanalysis in Nastran (SOL103) in order to extract the information needed to generate the flexible element. The data are then collected in two binary files:

- The file *mbdyn.mat* contains the initial position, velocity and acceleration of the grid points of the FEM spine model.

- The file *mbdyn.tab* contains the mass matrix and stiffness matrix.

Using the MBDyn routine *femgen* an ASCII *.fem* file is obtained which is structured in the following parts:

- RECORD GROUP 1: it contains the general information on the model, in particular:
  - NMODES is the number of FEM nodes in the FEM model
  - NNORMAL is the number of normal modes
  - NATTACHED is the number of *attached* modes
  - NCONSTRANINT is the number of constraint modes
  - NREJECTED is the number of rejected modes

  The number of available modes is then:

$$\begin{aligned} \text{NMODES} = &\text{NNORMAL} + \text{NATTACHED} + \\ &\text{NCONSTRAINT} - \text{NREJECTED} \end{aligned} \tag{35}$$

  In this case the mode up to 50 Hz are considered.
- RECORD GROUP 2: it contains a listing of the NMODES labels of the FEM nodes.
- RECORD GROUP 3: it contains the initial values of the NMODES modal unknowns
- RECORD GROUP 4: it contains the initial values of the NMODES modal unknowns derivatives
- RECORD GROUP 5: it contains the X component of the position of the NNODES FEM nodes in the reference frame attached to the modal node.
- RECORD GROUP 6: it contains the Y of the NNODES FEM nodes.
- RECORD GROUP 7: it contains the Z of the NNODES FEM nodes.
- RECORD GROUP 8: it contains the non-orthogonalized components of the NMODES modes, for each mode the X, Y, Z component of the modal displacement, and the three components RX, RY, RZ of the linearized modal rotation.
- RECORD GROUP 9: it contains the modal mass matrix $\mathbf{m}$ that results from equation 36.

$$\mathbf{m} = \{X\}^T [M] \{X\} \tag{36}$$

- RECORD GROUP 10: it contains the modal stiffness matrix $\mathbf{k}$ that results from equation 37.

$$\mathbf{k} = \{X\}^T [K] \{X\} \tag{37}$$

  The matrix is positive definite because the model in clamped at the buttocks down, by using the SPC card.

- RECORD GROUP 11: it contains the lumped inertia matrix associated to the NNODES FEM nodes: for each the *X*, *Y*, *Z*, *RX*, *RY*, *RZ*, inertia coefficients are listed.

The modal form obtained from the FEM model are used to reconstruct the displacements of the boundary nodes: these nodes then influence the movement of the structure to which they are linked.
Since we are using the *boundary mass* method the mass matrix obtained directly from the ALTER contains the contributions of the lumped mass of the arms and the lumped mass that represents the backrest constraint.

- The arms nodes are rigidly connected to the T2 vertebra through the RBE2 card.

- The backrest node is located at the same y and z direction of the T8 vertebra with an offset of 0.1 m in the negative x direction. This position can be freely changed using a *Matlab* script developed to generate the spine model. This node is then linked to the spine through the RBE3 element.

In order to link the reduced spine model to the MBDyn upper limb model and to the MBDyn seat model, the contributions of the arms and backrest masses have to be removed from the mass matrix.
The effect of a single lumped mass can be seen in the whole mass matrix as a (3x3) block placed in correspondence of the coordinate of the node as shown in equation 38:

$$\mathbf{M_N} = \begin{bmatrix} \ddots & & & & \\ & m_N & 0 & 0 & \\ & 0 & m_N & 0 & \\ & 0 & 0 & m_N & \\ & & & & \ddots \end{bmatrix} = m_N \begin{bmatrix} \ddots & & \\ & \mathbf{I}^{3x3} & \\ & & \ddots \end{bmatrix} \tag{38}$$

So the mass matrix, resulting from the *.fem* file is composed as shown in equation 39:

$$\begin{aligned} &\mathbf{M_A} = \mathbf{X}^T \left(\mathbf{M}^{(S)} + \mathbf{M}^{(A)} + \mathbf{M}^{(B)}\right)\mathbf{X} = \mathbf{I} \rightarrow \\ &\mathbf{M}^{(S)} = \mathbf{I} - \mathbf{X}^T \left(\mathbf{M}^{(A)} + \mathbf{M}^{(B)}\right)\mathbf{X} \end{aligned} \tag{39}$$

where $\mathbf{M_A}$ is the mass matrix that comes from the Alter file, $\mathbf{X}$ is the matrix that contains the displacement of the mode shapes associated

to the node of the arms and of the backrest, $\mathbf{M}^{(S)}$ is the mass matrix associated to the spine, $\mathbf{M}^{(A)}$, is the mass matrix associated to the arm, $\mathbf{M}^{(B)}$ is the mass matrix associated to the backrest. In equation 40 the matrix of the modes shape related to one arm is shown. For the other node the concept is the same.

$$\mathbf{X}_a = \begin{bmatrix} x_{a_1} & \dots & x_{a_i} & \dots & x_{a_{50}} \\ y_{a_1} & \dots & y_{a_i} & \dots & y_{a_{50}} \\ z_{a_1} & \dots & z_{a_i} & \dots & z_{a_{50}} \end{bmatrix} \tag{40}$$

So then the mass matrix related to a single boundary node becomes 41:

$$\mathbf{X}^T \mathbf{M}_a \mathbf{X} = m_a \left(\mathbf{X}^T \begin{bmatrix} \ddots & & \\ & \mathbf{I}^{3x3} & \\ & & \ddots \end{bmatrix} \mathbf{X} \right) = m_a (\mathbf{X}_a^T \mathbf{X}_a) \tag{41}$$

As last step of the process equation 41 is plugged into equation 39 obtaining the matrix of the spine purged 42:

$$\begin{aligned} \mathbf{M}^{(S)} = \mathbf{I} - [m_{a_L} (\mathbf{X}_{a_L}^T \mathbf{X}_{a_L}) + m_{a_R} (\mathbf{X}_{a_R}^T \mathbf{X}_{a_R}) + \\ + m_b (\mathbf{X}_b^T \mathbf{X}_b)] \end{aligned} \tag{42}$$

where m_{a_R} is the mass of the right arm, m_{a_L} is the mass of the left arm and m_b is the mass of the backrest. $\mathbf{X}_{a_R}$ contains the the mode shape related to the right arm, $\mathbf{X}_{a_L}$ contains the the mode shape related to the left arm and $\mathbf{X}_b$ contains the the mode shape related to the backrest. After having purged the mass matrix of the spine, it can be observed that it is no more diagonal. Finally a new *.fem* file is rewritten with the purged mass matrix and this is that file that MBDyn will read.

4.4.2 *Modal joint*

The *.fem* file that has been just created is read from MBDyn through the card *Modal joint*. This kind of joint implements a Component Mode Synthesis CMS of a flexible body. Its interface with multibody domain is represented by clamps that constrain the multibody interface nodes to the position and orientation of the corresponding FEM nodes. The modes shapes can be selected as well as a damping factor can be associated to each single mode. The boundary nodes are placed in a way to have the same coordinate both in MBDyn and in the *.fem* file.
The advantage of using the CMS approach is that the problem dimension is reduced and as also the time needed to perform the analysis. In fact the stiffness and mass matrices of the initial model have the dimension of the total degrees of freedom of the system, instead in the

modal model the matrices have the dimension of the mode used for the reduction. In order to have good dynamic reconstruction a small number of modes is generally needed.
This element solves the equation of the motion of the spine in the modal coordinate $\mathbf{q}$ and then the physical displacement are reconstructed through the mode shape matrix $\mathbf{X}$ using the well known transformation shown in equation 43:

$$\mathbf{u} = \mathbf{X}\mathbf{q} \qquad \text{where } \mathbf{u} \text{ is the physical displacement} \tag{43}$$

4.4.2.1 *Setup of the modal joint*

First of all a *modal* node is placed in the origin of the system: this node has the same characteristics of a *dynamic* node. A *dynamic* node is a node to which inertia can be attached, so it provides linear and angular momenta degrees of freedom. The *modal* node is required in order to handle the rigid body motion of the spine.
Moreover, three *static* nodes are placed in correspondence of the *.fem* boundary nodes: two representing the shoulder and one representing the backrest. Their coordinates are the same of the initial coordinate of the *.fem* model and in MBDyn they are expressed in the reference system of the *modal* node.
Finally the mode shape are chosen: this is a critical part because the stability and accuracy of the simulation depends on this choice. For the purpose of this work only the axial modes, the ones that acts primarily on the z axis, in the band from 0 to 50 Hz are chosen, as listed in table 13.

Mode	**Frequency** Hz	**Damping** %
7	3.29	0.30
12	9.21	0.15
19	15.92	0.10
30	29.78	0.05
42	41.2	0.03

Table 13: Modes used for the modal joint

4.4.2.2 *Seat model*

As last step a more sophisticated seat model is developed. For what concerns the bottom part of the seat the same approach used in the FEM model is followed: two masses representing the cushion and the seat are added under the buttocks down node with an offset of 0.1 m from this node. The node are connected to each other using a *rod element* to which is associated a linear viscoelastic law having the same parameters reported in 5.

Two nodes forms the backrest: one is the boundary node of the *.fem* file, the other has 0.1 m of negative x offset from the first node and is connected to the seat node through the *total joint* card which constraints all translations and rotations (the seat is considered as a rigid body). The two nodes are joined together through a *rod element* that uses in this case a non-linear viscoelastic law having the expression reported in equation 44[3]:

$$\begin{aligned} &F(\varepsilon) = 250 \cdot \frac{1}{3} \cdot \left(\varepsilon^3 - \varepsilon^3 \tanh(15\varepsilon)\right) \\ &\text{where} \qquad \varepsilon = \frac{l - l_0}{l_0} \\ &\text{where} \quad l \text{ is the deformed length of the rod} \\ &\qquad\quad l_0 \text{ is the non-deformed one} \end{aligned} \tag{44}$$

A unilateral constraint is implemented with this kind of law. When the deformation ε is zero, meaning that the spine is detached from the backrest, the elastic force is null, instead the higher is the penetration of the spine interface node in the backrest, higher will be the elastic force produced by the rod. A bilateral constraint can be easily implemented in the model using the law of equation 45:

$$F(\varepsilon) = 250 \cdot \frac{1}{3} \cdot \left(\varepsilon^3 - \varepsilon^3 \tanh(15\varepsilon)\right) + 250 \cdot \frac{1}{3} \cdot \left(\varepsilon^3 + \varepsilon^3 \tanh(15\varepsilon)\right) \tag{45}$$

The bilateral law can be used to simulate the seat-belt effect on the body.

4.5 ANALYSIS

4.5.1 *Frequency sweep analysis*

In order to verify the behaviour of the system a frequency response analysis was performed in MBDyn.
In order to get the acceleration from the head a *dynamic* node was placed as a dummy boundary node in correspondence of the head node of the FEM model. Then, using the card *total pin joint*, a vertical displacement was imposed at the ground. This displacement varies as a linear chirp: the frequency sweep card was used in order to control the amplitude during the simulation. In order to correctly set up this card these parameters are required:

- Starting frequency f_i = 0.2 Hz
- Ending frequency f_{end} = 50 Hz
- Starting time T_i = 4 s. This time is needed in order to permit to system to stabilized itself after the introduction of the gravity: at the beginning of the simulation the system must be stationary.

3 The law works with odd power of ε

- Ending time T_{end} = 300 s. This time must be great enough in order to permit to the system to take gradually the next frequency: the simulation has to be at most quasi-static as possible.
- Sample time dt = 0.002 s. In order to have a clean signal in output, avoiding aliasing, 10 sample per period are taken at the highest frequency: this correspond to a sample frequency of 500 Hz.

In the simulation the frequency varies linearly as:

$$f(t) = f_i + kt \tag{46}$$

Where *k* is the *chirpiness* defined as:

$$k = \frac{f_{end} - f_i}{T_{end} - T_i} \tag{47}$$

For an harmonic signal:

$$x(t) = \sin(\varphi(t)) \tag{48}$$

The instantaneous frequency is then defined as:

$$f(t) = \frac{1}{2\pi}\frac{d\varphi(t)}{dt} \tag{49}$$

The value of $\varphi(t)$ can be obtained after the integration along the simulation of the $f(t)$ as follows:

$$\begin{aligned}\varphi(t) &= \varphi_0 + 2\pi\int_{T_i}^{T_{end}}(f_i + k\tau)d\tau \\ &= \varphi_0 + 2\pi\left[f_i(T_{end} - T_i) + \frac{k}{2}\left(T_{end}^2 - T_i^2\right)\right]\end{aligned} \tag{50}$$

The time domain linear chirp sine is then:

$$x(t) = \sin\left[\varphi_0 + 2\pi\left(f_i(T_{end} - T_i) + \frac{k}{2}\left(T_{end}^2 - T_i^2\right)\right)\right] \tag{51}$$

Since the quadratic term has $\frac{k}{2}$ as coefficient this justify why in MBDyn the corresponding term is written as:

$$k_{MBDyn} = \frac{1}{2}\frac{f_{end} - f_i}{T_{end} - T_i} \tag{52}$$

Since the input signal has to be transformed in the frequency domain using the Fast Fourier Transform, for the first semi-period the amplitude of forcing term is pre-multipied by a $\left(1 - \cos\left(\frac{2\pi}{T}\right)\right)$ factor. The same is done at the end of the simulation. This is done in order to obtain a smooth forcing signal without any angular point.
The input and output signal are then processed in Matlab through the function *fft*. To obtain the frequency response function (FRF) from

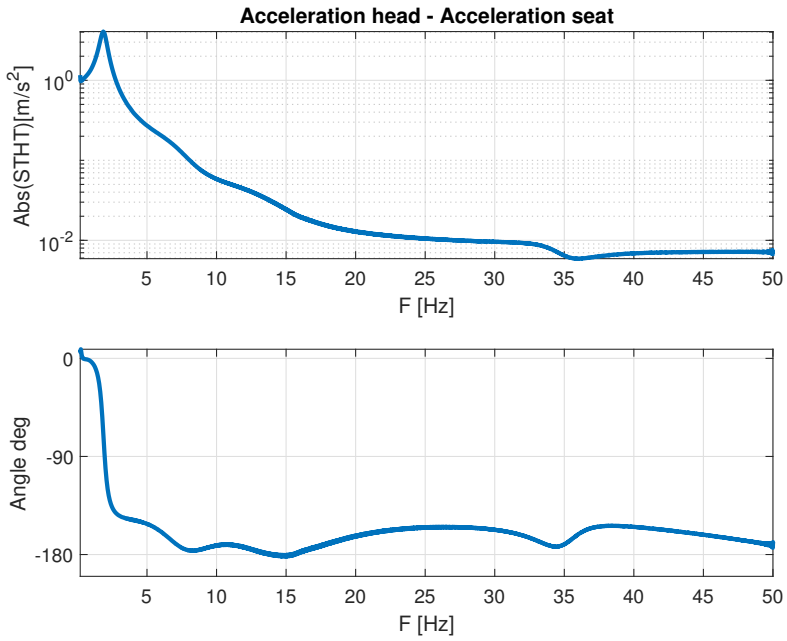

Figure 19: FRF seat-to-head non filtered for a reference subject

the acceleration on the seat A_s to the acceleration on the head A_h, the H_1 estimator has been used:

$$H_1 = \frac{A_s \cdot A_h^*}{A_s \cdot A_s^*} \tag{53}$$

The figure 19 shows the frequency response function of a subject that has the following biomechanical parameters:

- Age: 25 years
- Height: 1.80 m
- Weight: 58.34 kg
- Gender: male

Since in the band between 10 Hz and 20 Hz some noise is present, a 6^{th} order Butterworth, with cutting frequency at 100 Hz has been implemented. The filtered signal is showed in figure 20.

In figure 21 are compared the STHT of the FEM model and the CMS model. The primal resonance frequency for the FEM model is found at 2.1 Hz instead for the CMS model it is found at 1.85 Hz. The module at resonance is equal to 3.5 m/s^2 for the FEM model and to 4 m/s^2 for the CMS. Considering the module diagram the two model are quite well correlated at least up to 35 Hz then the module of the CMS tends to remain constant, while in the FEM model it continues to decrease. Regarding the phase diagram, the two models are almost identical up to 10 Hz then in the CMS model the phase remains constant at

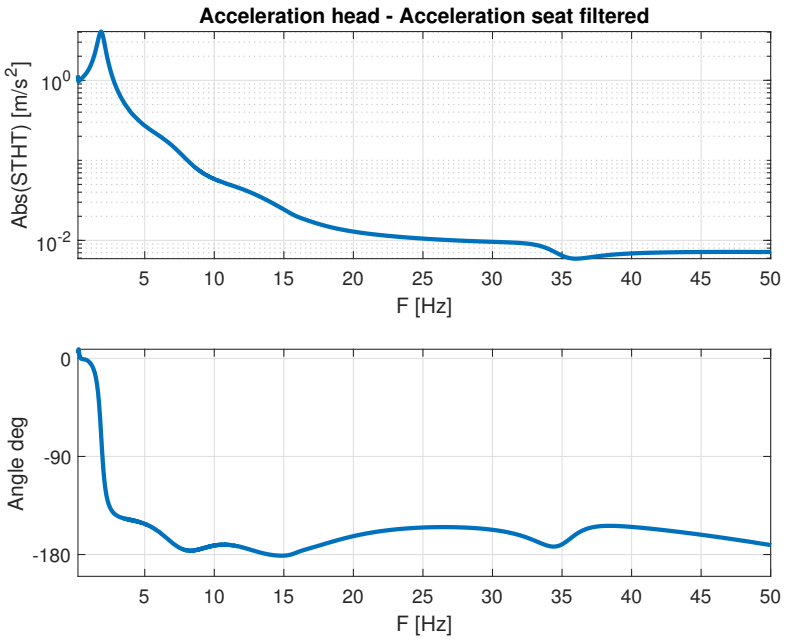

Figure 20: FRF seat-to-head filtered for a reference subject

180°, while in the FEM it continues to decrease to value lower than 360°. The reduction process can be validated: in fact in the range 0-10 Hz they are almost identical for both the phase and amplitude. The differences can be attributed to the fact that the CMS is using only five axial modes, while the complete mode base of the FEM model is formed by 55 modes until 50 Hz. Also the backrest model is modelled with the unilateral spring in the CMS model while in the FEM model with a traditional spring. Finally CMS model has the complete upper limbs model, while in the FEM the limbs are represented with two concentrated masses without inertia.

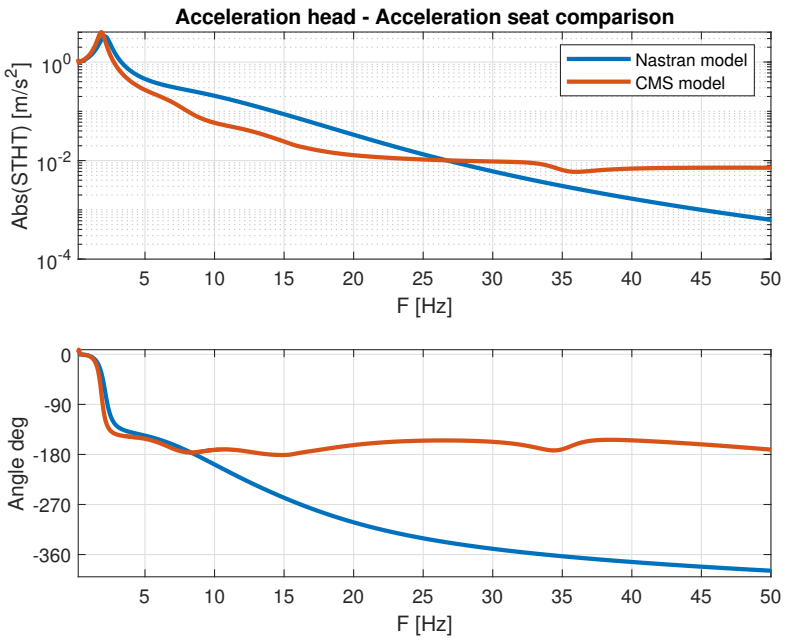

Figure 21: Comparison between the STHT of the FEM model and the one coming from the CMS procedure

5

PARAMETER SCALING ON SUBJECT ANTHROPOMETRIC PARAMETERS

In this chapter the procedure used to scale the spine model is described as a function of the anthropometric parameter age, body mass index BMI, stature and height. The results are then compared with the experimental data reported in Toward and Griffin [38].

5.1 MODEL PARAMETRIZATION

One of the big advantage of Finite element model FEM as well as MBD one, with respect to the lumped parameter LPM, is the possibility to be parametrized. In fact lumped parameter models do not respect the physical characteristics of the model, for example its geometry, but they are tuned in a order to match the experimental data that comes from a single subject or the average response of a group of subjects, as for example the model of Boileau and Rakheja [8]. On the other hand, the FEM and MBD models are more representative of the geometrical and physics characteristics of the subject: for example the geometric coordinates of the vertebral nodes are locate in the same position of the vertebrae of the real subject. Thanks to this feature a scaling procedure has been implemented in Zanoni and Masarati [45] in order to adapt the FEM and MBD models to represent subject with different anthropomorphic characteristics: the model can be generated starting from a generic anthropometric dataset $\mathbf{s}$ that contains: age a, Body Mass Index BMI, stature h, and gender g:

$$\mathbf{s} = \begin{bmatrix} a & \text{BMI} & h & g \end{bmatrix}^T \tag{54}$$

The scaling procedure is based on the parametric ribcage model proposed by Shi et al. [32]. In this work, a statistical rib cage geometry model that takes into consideration the parameters listed in 54 was developed. First of all clinical thorax scans were obtained from 89 subjects evenly distributed over both sexes with ages of 18-89 years, stature 1.5-2.0 m, and BMIs 16-55 kg/m^2. To describe the size and shape of the rib cage as well as the cross-sectional geometry of each rib, a total of 464 landmarks on the left side of each subject's ribcage were collected as displayed in figure 22. The positions of the landmarks were subjected to a principal component analysis (PCA) following the procedure reported in Allen, Curless, and Popović [2]. After having generated the ribcage landmarks, a bounding box is fitted to the left side of the ribcage, and its dimensions x, y, z are compared to those of the subject used in the paper of Kitazaki and Griffin [19].

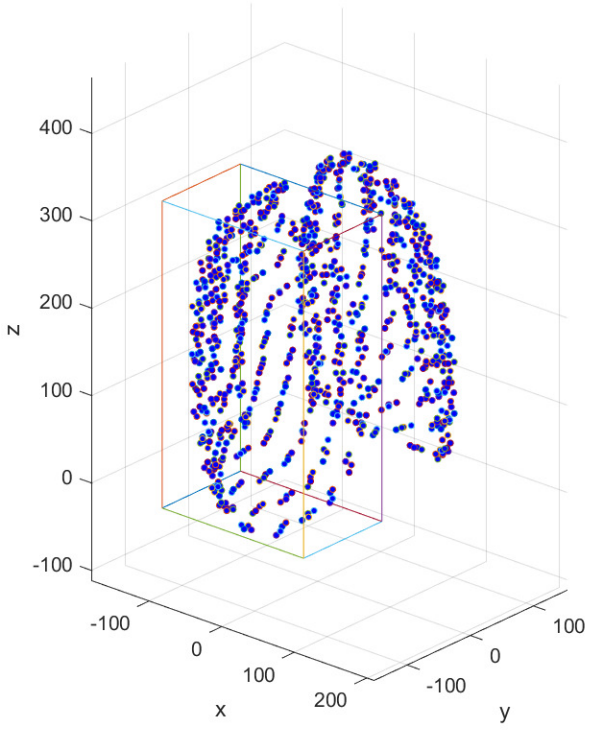

Figure 22: Generated ribcage landmarks point cloud for a male subject of 33 years, 1.80 m, 70 kg. Values on the axes are in mm

Since the anthropometric parameters of the Kitazaki model are unknown, these parameters are estimated by minimizing the sum of the square of the distance between the single vertebrae of the model of [19] and the one predicted by the ribcage model of Shi et al. [32]:

$$\min \sum_i \left(d_i^k - d_i^s\right)^2 \tag{55}$$

where d_i^k is the position of the i vertebra in the Kitazaki model and the d_i^s is the position of the i vertebra predicted by the ribcage model of Shi et al. [32]: d_i^s changes with the anthropometric parameters. At the end of the iterative process, it turns out that the most probable anthropometric dataset is: 34 years old male, 1.78 m, 84 kg so 26.5 BMI. The three scaling coefficients are then:

$$\lambda_x = \frac{x}{x_0} \qquad \lambda_y = \frac{z}{z_0} \qquad \lambda_z = \frac{z}{z_0} \tag{56}$$

where x_0, y_0 and z_0 are the reference values that come from Kitazaki and Griffin [19] model. The scaling parameters are used to estimate the variation of the other model parameters, such as the mass param-

eters, the stiffness and damping. For example the axial stiffness is scaled as:

$$K'_a \sim \frac{EA'}{L'} = \frac{EA}{L} \cdot \frac{\lambda_x \lambda_y}{\lambda_z} = K_a \frac{\lambda_x \lambda_y}{\lambda_z} \tag{57}$$

Where K'_a represents the value of the axial stiffness of the subject to be modeled, while K_a represents the reference value taken from the Kitazaki and Griffin [19] model. The other structural parameters are scaled following the same philosophy.
For what concerns the geometry a parametric spline (NURBS) representing the spine axis is fitted in the thoracic part to the ribcage model, using as control points the estimated locations of the ribs heads. The remaining parts of the spine are adapted by scaling the reference shape identified using the vertebrae of the *erect* pose of the Kitazaki and Griffin [19] model.

5.2 MODEL VALIDATION

To evaluate the efficiency of the scaling procedure a comparison between the FEM model and the experimental results presented in Toward and Griffin [38] was performed.
In the following analysis the transfer functions were calculated between the vertical seat acceleration and the vertical force at the seat surface to give the apparent masses of the subjects. The apparent mass was calculated from the ratio of the cross-spectral density between the force F_{z_s} and acceleration at the seat A_{z_s}, to the power spectral density of the acceleration at the seat, the H_1 estimator was then obtained 58:

$$H_1 = \frac{F_{z_s} \cdot A^*_{z_s}}{A_{z_s} \cdot A^*_{z_s}} \tag{58}$$

For the FEM model the F_{z_s} was obtained from the z component of the reaction force of the SPC (single point constraint) placed at the buttock down.
The frequency resolution was 0.05 Hz for the FEM model, instead the experimental data had a resolution of 0.195 Hz. For both cases the band of interest was spaced from 0.6 to 20 Hz. The forcing term was introduced in the FEM model by applying an acceleration of 1 m/s^2 at the buttock down node. The primary resonance frequency was defined as the frequency at which the apparent mass was greatest. The normalized apparent mass was obtained by dividing the apparent mass obtained from $||H_1||$ by the value of the apparent mass at 0.6 Hz.

5.2.1 *Different Seat condition*

The first kind of comparison was made by measuring the apparent mass of the subject listed in 14. Different backrest condition were simulated:

1. Sitting upright with no backrest.
2. Sitting upright with a rigid backrest.
3. Sitting with a rigid backrest reclined to 15°.
4. Sitting with a foam backrest reclined to 15°.

The backrest has been built in the FEM model with an RBE3 which has the REFGRID node positioned at the same z and y of the T7 vertebra, with an offset of 0.1 m in the negative x direction. The REFGRID point is then connected to the vertebral node that spaced from T1 to T10.
In the case of rigid backrest, the constraint between spine and the backrest is simulated using a SPC card that allows the displacement only in z direction, the other components of translation and rotation are constrained.
In the case of foam backrest a viscoelastic element, using the CDAMP2 and CELAS2 card, is added between the REFGRID element and another node that is placed with a negative x offset of 0.2 m from the T7 vertebra. This element has the same proprieties of the foam reported in Toward and Griffin [38]: a stiffness of 21 $\mathrm{kN\,m^{-1}}$ and a damping of 109 $\mathrm{N\,s\,m^{-1}}$.

Subject	**Gender**	**Age**	**Weight** kg	**Stature** cm	**BMI**
FEM max	Male	33.7	103	180	31.79
FEM mean	Male	33.7	70.5	171	24.11
FEM min	Female	33.7	46	158.94	18.2

Table 14: Parameter of the subject used for different backrest condition

5.2.2 *Discussion of the results*

In table 15 and figure 23 the results of the experiment and analysis conducted without backrest, using the anthropometric parameters of table 14, are resumed. The FEM model shows an increasing of the primal resonance frequency as the BMI decrease. In the experimental work of Toward and Griffin [38] the maximum frequencies varies from 3.5 Hz to 6.4 Hz and is in agreement with the inverse proportionality between the resonance frequency and the BMI. Considering

Model	**Res. Freq.** Hz **FEM**	**Res. Freq.** Hz **Exp**
Model max	4.55	4.351654898
Model mean	4.75	4.561938618
Model min	5.05	4.721075514

Model	**App. mass at res. FEM** kg	**App. mass at res. Exp** kg
Model max	101.624	117.8246075
Model mean	86.18325	92.13482919
Model min	62.41259	68.25719291

Model	**App. mass static FEM** kg	**App. mass static Exp** kg
Model max	64.08415	75.39916448
Model mean	55.9839	62.28778384
Model min	41.33262	49.60278957

Table 15: Results of the no backrest condition and comparison with the experimental results

the amplitude, for subject with higher BMI the ratio between the apparent mass at resonance and the static mass in bigger than for the one that have a smaller BMI, and this tendency is supported also by the experimental results: the FEM normalized apparent mass at resonance varies from 1.57 to 1.51, instead for the experiment from 1.56 to 1.38.
In table 16 and figure 24 are showed the results of the experiment and analysis conducted considering a reclined backrest with an inclination of 15°. The experiment highlights a reduction in the values of the apparent mass at resonance and in the static value, and an increasing in the resonance frequency with respect to the experiment conducted without backrest. The model is not able to capture this reduction, in fact the value are almost the same of the no backrest case.
In table 17 and figure 25 the results of the experiment and analysis conducted considering a rigid backrest with 0° inclination are resumed. The experiment shows a reduction of the resonance apparent mass related to an increasing of the resonance frequency with respect to the no backrest condition. Instead, these values are higher if compared to the inclined rigid backrest. The model instead shows a slight reduction on these values compared to the no backrest condition, but the differences in this case are not as relevant as in the experiment.
In table 18 and figure 26 the results of the condition with a foam backrest inclined of 15° are resumed. The experimental results shows a reduction of the apparent mass at resonance with respect to the

Model	**Res. Freq.** Hz **FEM**	**Res. Freq.** Hz **Exp**
Model max	4.55	5.597071037
Model mean	4.75	5.53350194
Model min	5	5.427553444

Model	**App. mass at res. FEM** kg	**App. mass at res. Exp** kg
Model max	102.4673	100.4302918
Model mean	86.61503	77.19406167
Model min	62.3659	56.31357839

Model	**App. mass static FEM** kg	**App. mass static Exp** kg
Model max	63.98861	68.41355076
Model mean	55.92552	55.02862558
Model min	41.49308	43.14281202

Table 16: Results of the reclined rigid condition and comparison with the experimental results

Model	**Res. Freq.** Hz **FEM**	**Res. Freq.** Hz **Exp**
Model max	4.55	5.007465121
Model mean	4.8	5.172068888
Model min	5.05	5.219857078

Model	**App. mass at res. FEM** kg	**App. mass at res. Exp** kg
Model max	101.3738	109.0692358
Model mean	86.01709	83.99847594
Model min	62.39323	60.52797736

Model	**App. mass static FEM** kg	**App. mass static Exp** kg
Model max	64.35031	69.91617679
Model mean	56.22032	57.86087524
Model min	41.83184	45.59220553

Table 17: Results of the upright rigid condition and comparison with the experimental results

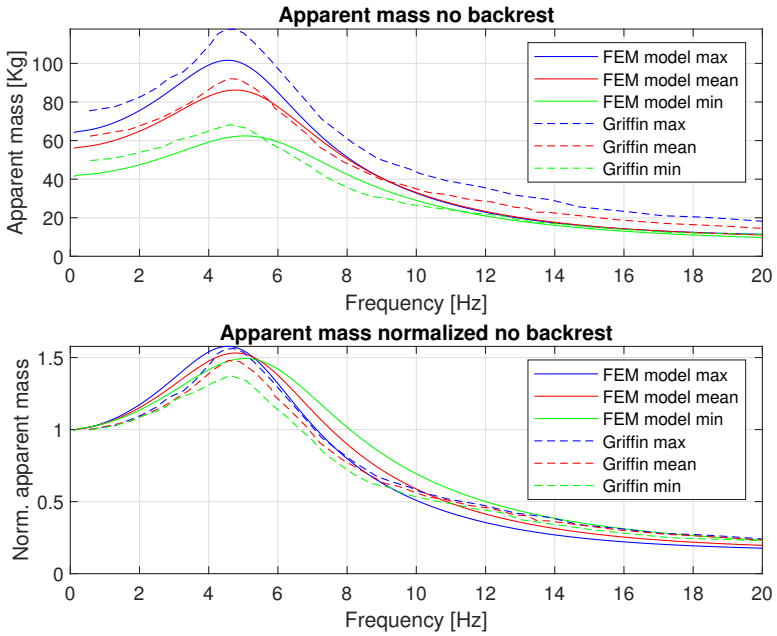

Figure 23: Apparent mass with no backrest

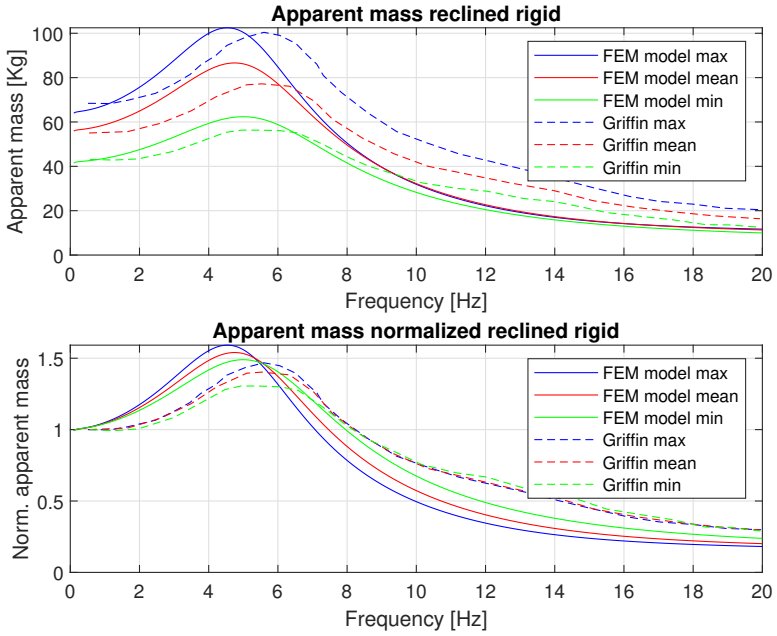

Figure 24: Apparent mass reclined rigid

no backrest condition: the normalized increment is between 1.55 and 1.43, in this case also the FEM model shows a reduction on the value of apparent mass: normalized it varies from 1.53 to 1.46. The resonance frequency of the experiment and the models are quite similar. These results can validate the complete backrest model.

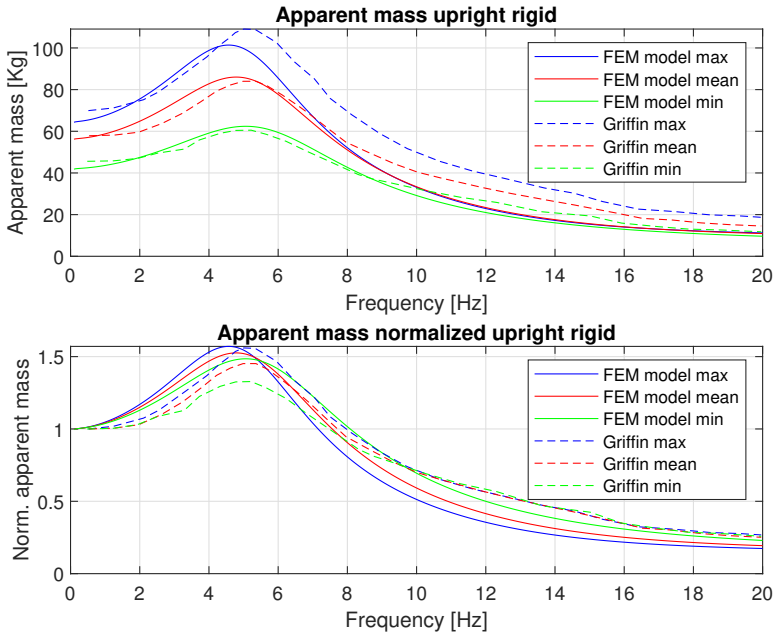

Figure 25: Apparent mass upright rigid

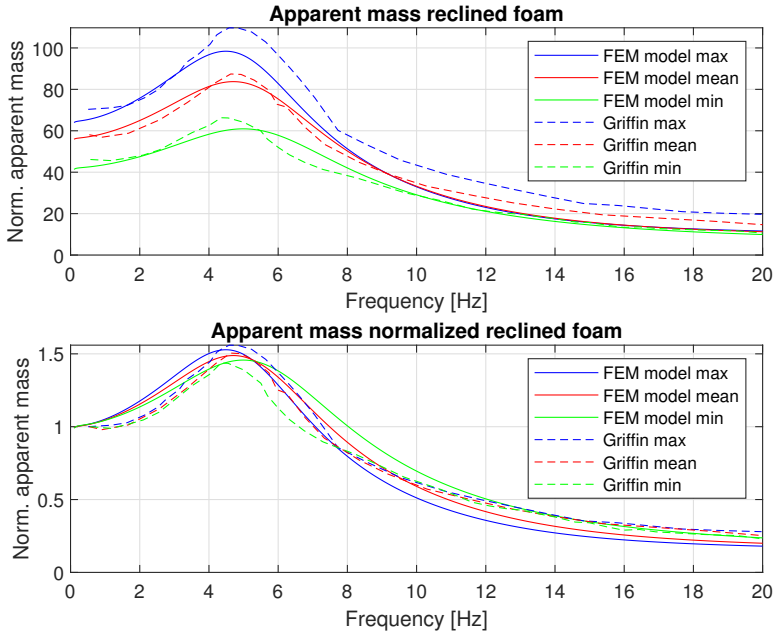

Figure 26: Apparent mass reclined foam

5.2.3 *Effect of the single parameter*

In this section the effect of the change in a single anthropometric parameter is evaluated. The other parameter remains unchanged from the Toward and Griffin [38] mean subject. The subject has no backrest

Model	**Res. Freq.** Hz **FEM**	**Res. Freq.** Hz **Exp**
Model max	4.5	4.586951132
Model mean	4.7	4.629414083
Model min	5	4.853404902

Model	**App. mass at res. FEM** kg	**App. mass at res. Exp** kg
Model max	98.40928	109.7231472
Model mean	83.72991	87.42243536
Model min	60.93369	66.29544517

Model	**App. mass static FEM** kg	**App. mass static Exp** kg
Model max	64.01688	70.35012006
Model mean	55.94893	58.07939343
Model min	41.37673	46.12877272

Table 18: Results of the reclined foam condition and comparison with the experimental results

and the excitation is produced by an acceleration of 1.0 m/s^2 at the buttock down.

Subject	**Gender**	**Age**	**Weight** kg	**Stature** cm	**BMI**
1	Male	33.7	58.48	171	20
2	Male	33.7	64.33	171	22
3	Male	33.7	73.1	171	25
4	Male	33.7	90.64	171	31

Table 19: BMI used for the mean subject

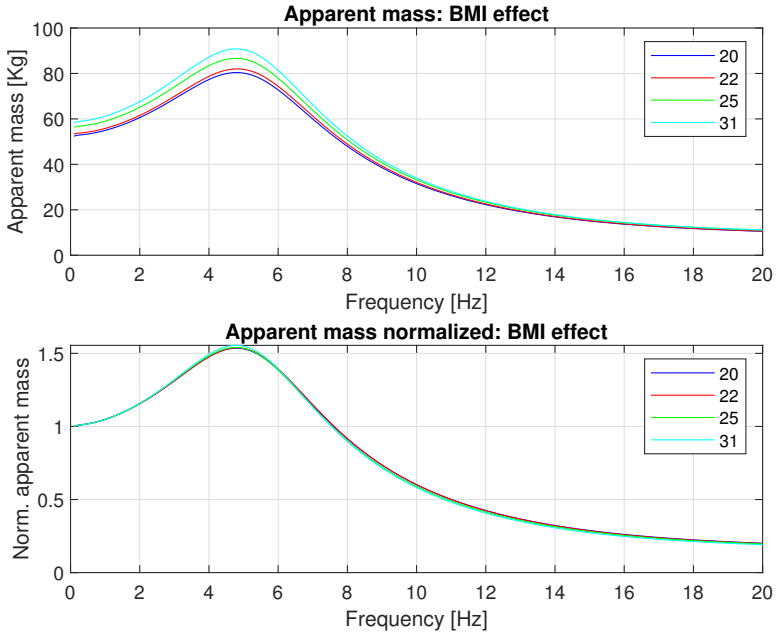

Figure 27: Apparent mass: BMI effect

Subject	Gender	Age	Weight kg	Stature cm	BMI
1	Male	21	70.5	171	24.11
2	Male	25	70.5	171	24.11
3	Male	35	70.5	171	24.11
4	Male	53	70.5	171	24.11

Table 20: Age used for the mean subject

Subject	Gender	Age	Weight kg	Stature cm	BMI
1	Male	33.7	54	171	18.46
2	Male	33.7	64	171	21.88
3	Male	33.7	74	171	25.3
4	Male	33.7	84	171	28.72

Table 21: Weight used for the mean subject

Subject	Gender	Age	Weight kg	Stature cm	BMI
1	Male	33.7	70.5	156	28.96
2	Male	33.7	70.5	167	25.27
3	Male	33.7	70.5	176	22.76
4	Male	33.7	70.5	185	20.6

Table 22: Stature used for the mean subject

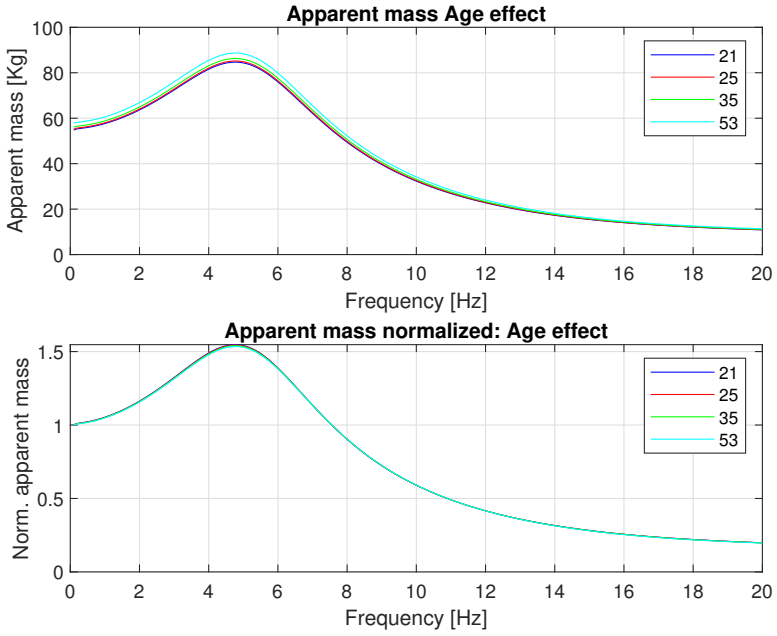

Figure 28: Apparent mass: age effect

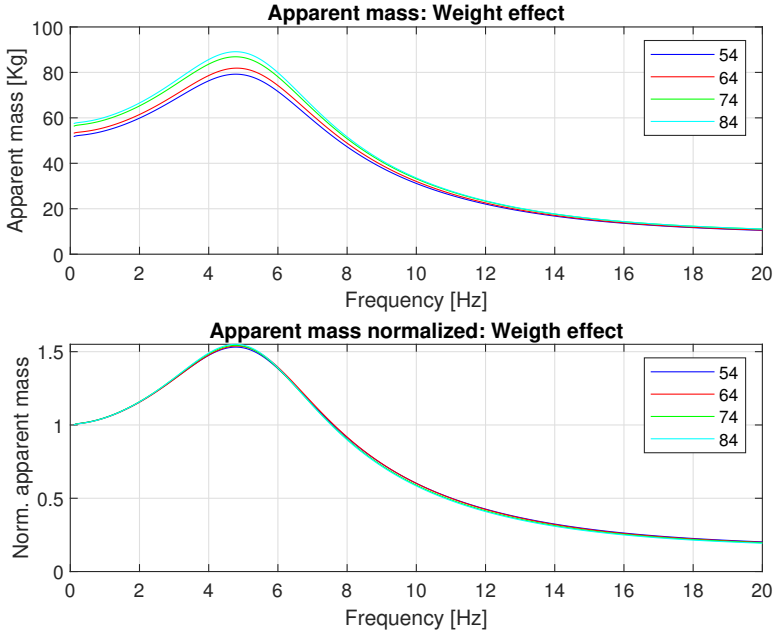

Figure 29: Apparent mass: weight effect

Subject	**Gender**	**Age**	**Weight** kg	**Stature** cm	**BMI**
1	Male	33.7	70.5	171	24.11
2	Female	33.7	70.5	171	24.11

Table 23: Gender used for the mean subject

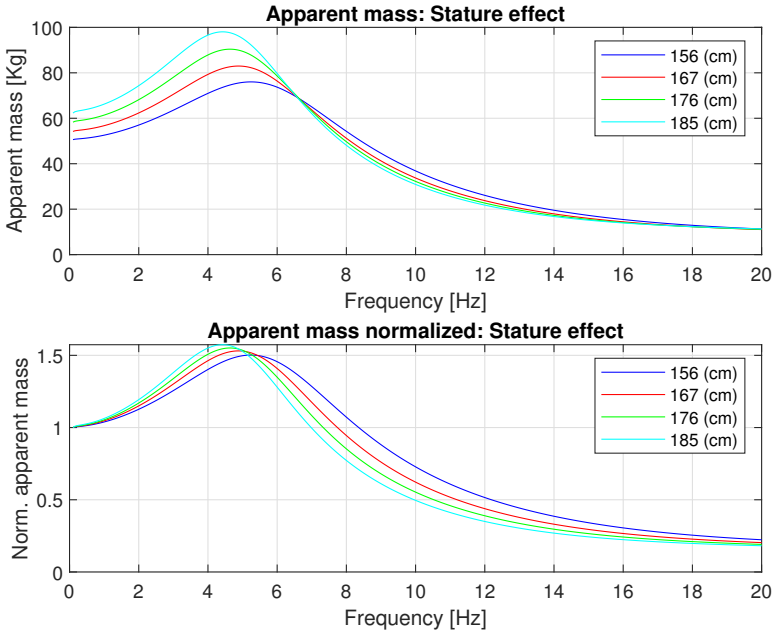

Figure 30: Apparent mass: stature effect

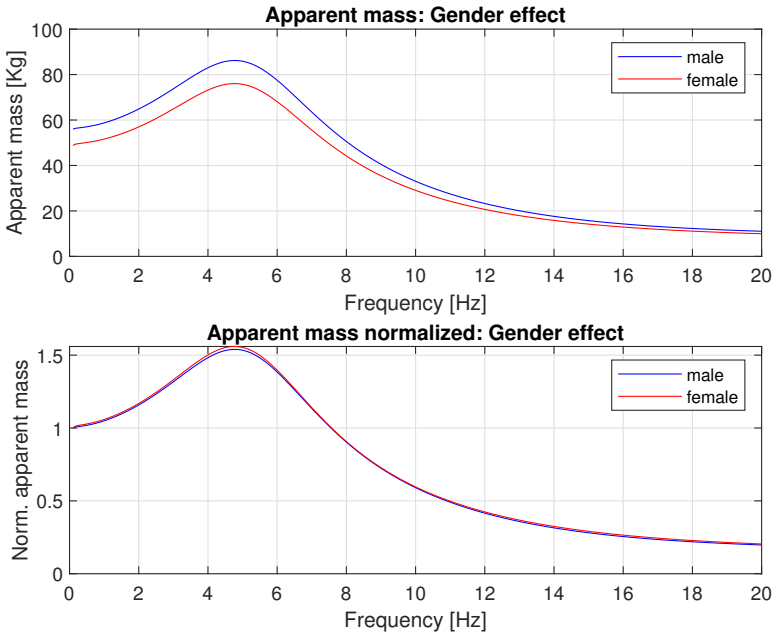

Figure 31: Apparent mass: gender effect

5.2.4 *Result discussion*

In the tables 24 and 25 the results of the experiments and FEM simulations respectively are reported. Concerning the BMI effect, the resonance frequency remains substantially unvaried in the FEM simulation (4.75-4.8 Hz) as in the experiment (4.7-5.1 Hz). The model is not able, instead, to capture the variation on the normalized AM: in the experiment it varies from 1.53 to 1.67 with the maximum related to the 25 BMI subject, but in the model it remains almost constant (1.53-1.55). The same discussion can be done analysing the weight effect, since both simulations were performed varying only the weight of the subject.
Considering the age effect, in the experimental results a direct proportionality between the resonance frequency and the age is highlighted: it passes from 4.6 Hz to 5.5 Hz. The FEM model is not able to capture this increment in the resonance frequency. For what concerns the normalized AM at resonance it tends to remains constant in both the cases: 1.54 for the model and 1.57 for the experiment.
Considering the stature effect, the model shows a great sensibility to this parameter: the resonance frequency decreases as the stature increases: 5.25 to 4.4 Hz); this result is confirmed also from the experiments even if the variation is smaller: 5 to 4.8 Hz. The normalized AM increases as the stature increases from 1.50 to 1.57 in the model, and from 1.52 to 1.67 in the experiment.
Considering the gender effect, in the model the resonance frequency is the same (4.75 Hz) for both male and female, instead in the experiments male tend to have a higher resonance frequency (5 Hz) than the female (4.9 Hz). Also for what concerns the normalized AM the female has a higher value 1.56 than the male 1.54. The experiments instead show that male has higher value 1.65 compared to the one of the female 1.52.
Summarizing, the most sensible parameter in the model turns out to be the stature, instead in the experiments was both weight and BMI. This result can be explained considering that the scaling process has been done taking as input the geometry of the ribcage, and not the weight of the subject. The model then is not able to well capture the extreme weight variation, but if we consider the mean subject the a results are well correlated: for example the 74 kg subject has a resonance frequency of 4.75 Hz in the model and 4.7 Hz in the experiment; with a normalized AM of 1.54 in the model and 1.57 in the experiment.

Effect	**Res freq** Hz	**App. at res** kg	**Static mass** kg
BMI kg/m^2			
20	5,1	77,6	50,5
22	4,7	92,3	59,2
25	5	107,7	64,4
31	4,9	114,8	71,7
Age (years)			
21	4,6	96,8	61,5
25	4,8	99,3	59,6
35	4,9	93,6	59,7
53	5,5	102,6	65,1
Weight kg			
54	5,1	71,2	47,7
64	4,9	88,7	56,4
74	4,7	106	67,3
88	5	126,4	74,6
Stature cm			
156	4,9	79,5	52,3
167	5	89,3	58,7
176	5	104,6	64
185	4,8	119	70,9
Gender			
Female	4,9	86	56,4
Male	5	110,2	66,6

Table 24: Experimental results of the single parameter variation, from [38]

Effect	**Res freq** Hz	**App. at res** kg	**Static mass** kg
BMI kg/m^2			
20	4,8	80,39358	52,37457
22	4,8	82,00476	53,31268
25	4,75	86,65576	56,25829
31	4,8	90,80784	58,40655
Age (years)			
21	4,75	84,66348	54,72354
25	4,75	85,1611	55,14783
35	4,75	86,26462	56,02118
53	4,75	88,68364	57,80306
Weight kg			
54	4,8	79,21115	51,73364
64	4,8	81,877	53,22791
74	4,75	86,87436	56,31168
84	4,8	89,10107	57,47322
Stature cm			
156	5,25	76,00621	50,60572
167	4,9	82,97889	54,20661
176	4,65	90,39858	58,28477
185	4,4	98,03316	62,30023
Gender			
Male	4,75	86,18325	55,9839
Female	4,75	76,0244	48,74956

Table 25: FEM model results of the single parameter variation

Part III

RESULTS

In the last part of the work the multibody model and the finite element one has been compared, then the influence of the spine model on the problem of pilot assisted oscillation, in the end the lumped parameter model, the finite element and multibody have been inserted in a virtual helicopter environment evaluating the amount of vibration that are transmitted to the head.

6 RESULTS

In this chapter the principal results of this work are illustrated. In the first section the FEM seated model and the MBD have been compared. In the second section the helicopter command responses with the CMS spine model and without it. In the last section a comfort ride evaluation has been performed, inserting the FEM, LPM and MBD in a state-space helicopter model.

6.1 COMPARISON OF THE TRANSFER FUNCTION BETWEEN THE FEM AND MULTIBODY MODEL

In this section the FEM and the MBD models have been compared. The FRF of three subjects having respectively 18, 23, and 25 kg/m^2 of BMI have been evaluated, taking as input the acceleration imposed at the floor and as output the accelerations at the seat node, at the pelvis and at the head.
For what concerns the FRF between the acceleration at the floor to the acceleration at the head (shown in figures 34,35 and 38), the two model are quite similar: both models has the first resonance peak at 2 Hz with an amplitude of 3.3 m/s^2 for the FEM model and 3.8 m/s^2 for the MBD model.
For what concerns the FRF between the acceleration at the floor to the acceleration to the pelvis (shown in figures 33, 36 and 39), both models found the primal resonance peak at 2.1 Hz with an amplitude of 2.8 m/s^2 for the FEM model and of 3.5 m/s^2 for the MBD. Around 12 Hz the MBD model found a small resonance peak of 0.12 m/s^2 amplitude. This peak is not captured by the FEM model.
For what concern the FRF between the acceleration at floor to the acceleration to the seat (shown in figure 34, 37 and 40)the models presents and almost identical response both for the FEM model and for the MBD model. The first resonance peak is found at 1.9 Hz for both models, with an amplitude of 1.8 m/s^2 for the FEM model and 2.05 m/s^2 for the MBD model. A second resonance peak, more damped than the first, is found around 10 Hz with an amplitude of 0.75 m/s^2. Between the two resonance peaks at 3 Hz is found the anti-resonance peak with an amplitude of 0.3 m/s^2 for both models.
There are not great difference between the three subjects. This in accordance to the discussion made in chapter 5, in which it was underlined the limitation of the scaling model to well capture the differences between subjects that share the same height and age, but with different weight.

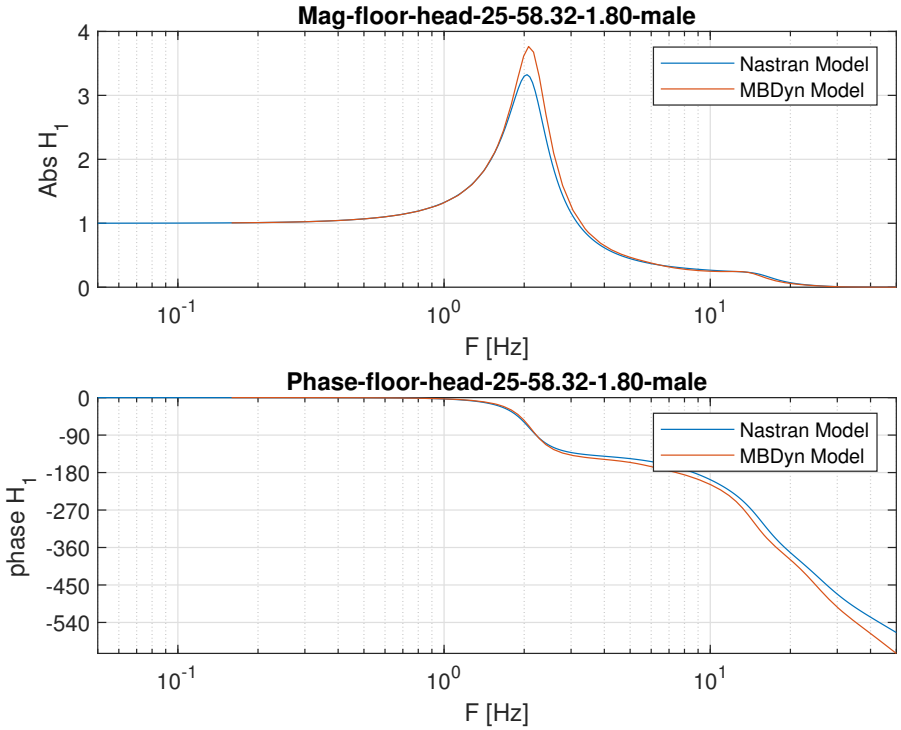

Figure 32: Transfer function between floor and head for a 18 BMI subject

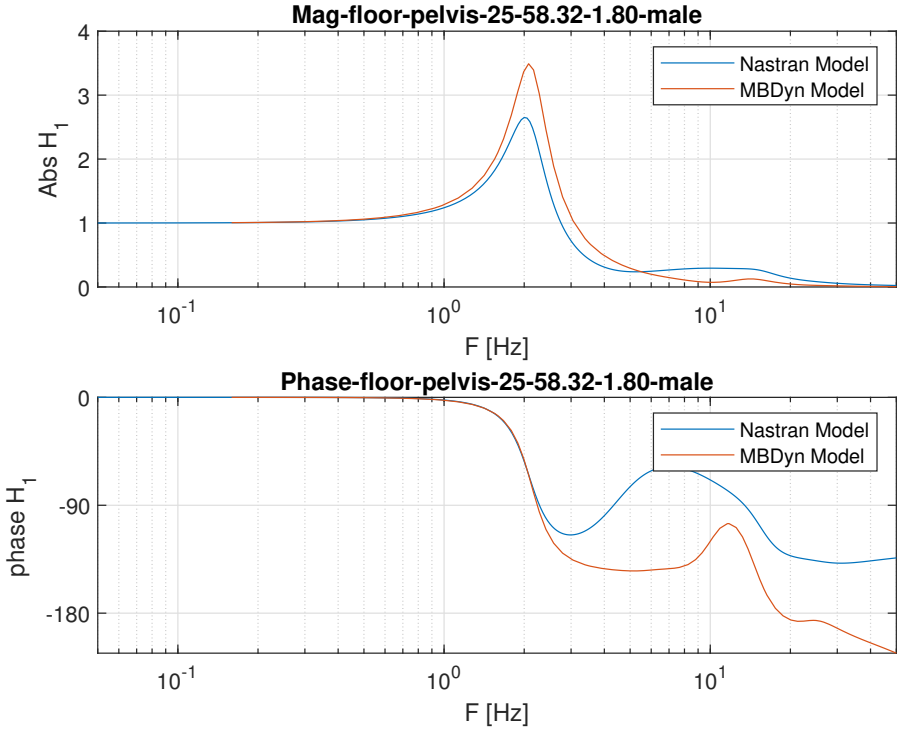

Figure 33: Transfer function between floor and pelvis for a 18 BMI subject

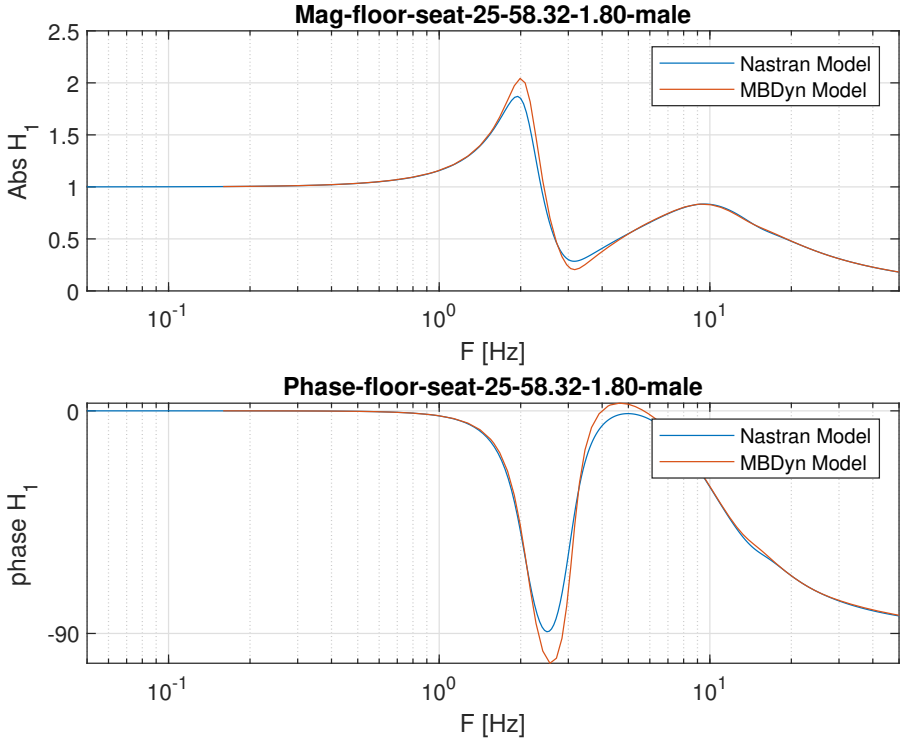

Figure 34: Transfer function between floor and seat for a 18 BMI subject

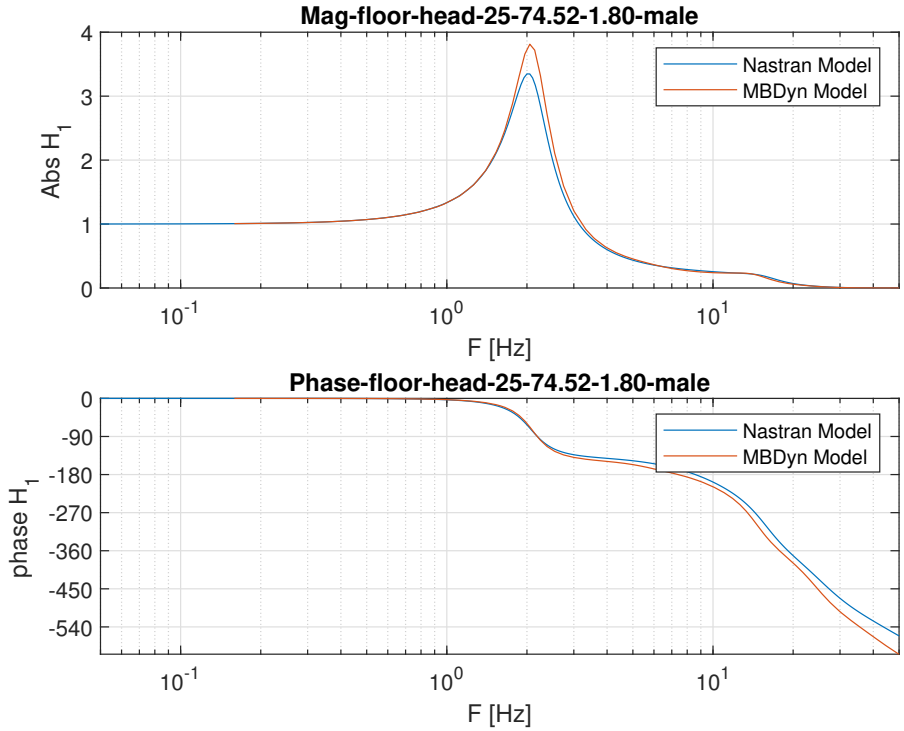

Figure 35: Transfer function between floor and head for a 23 BMI subject

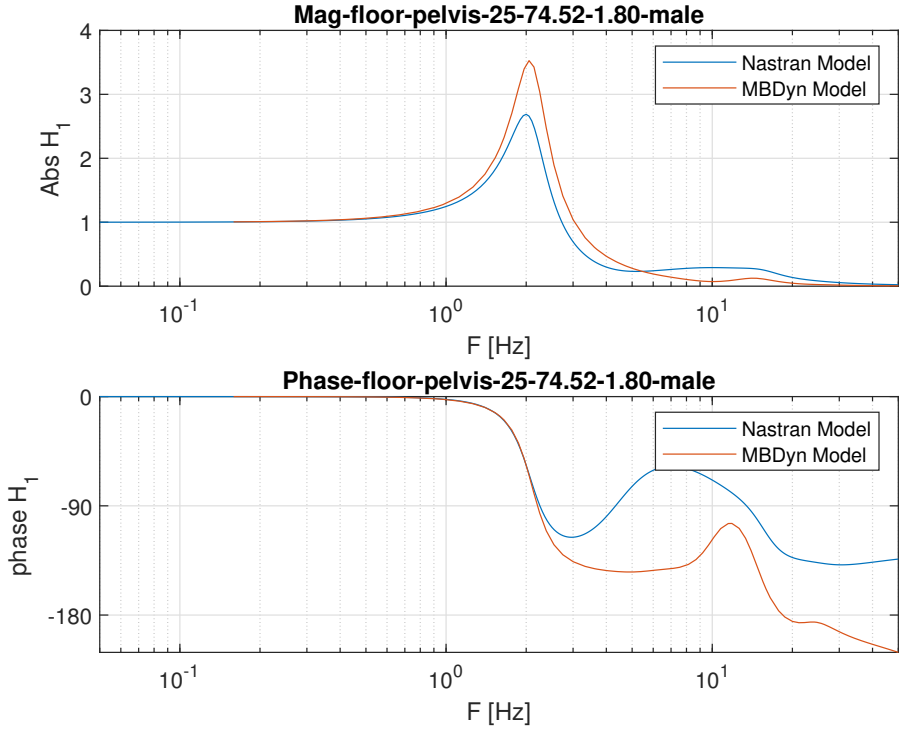

Figure 36: Transfer function between floor and pelvis for a 23 BMI subject

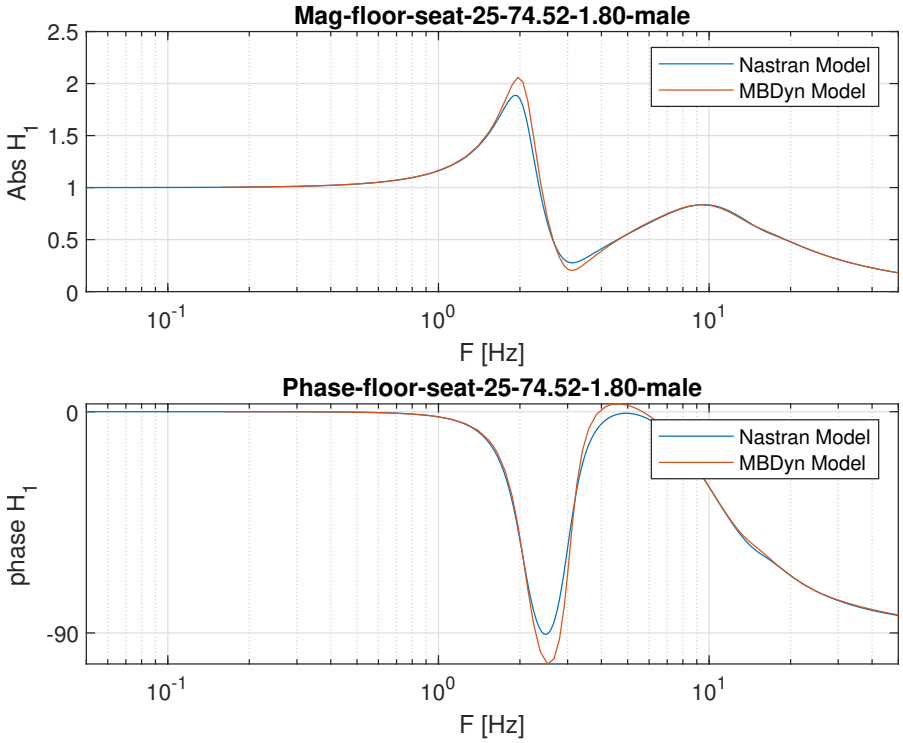

Figure 37: Transfer function between floor and seat for a 23 BMI subject

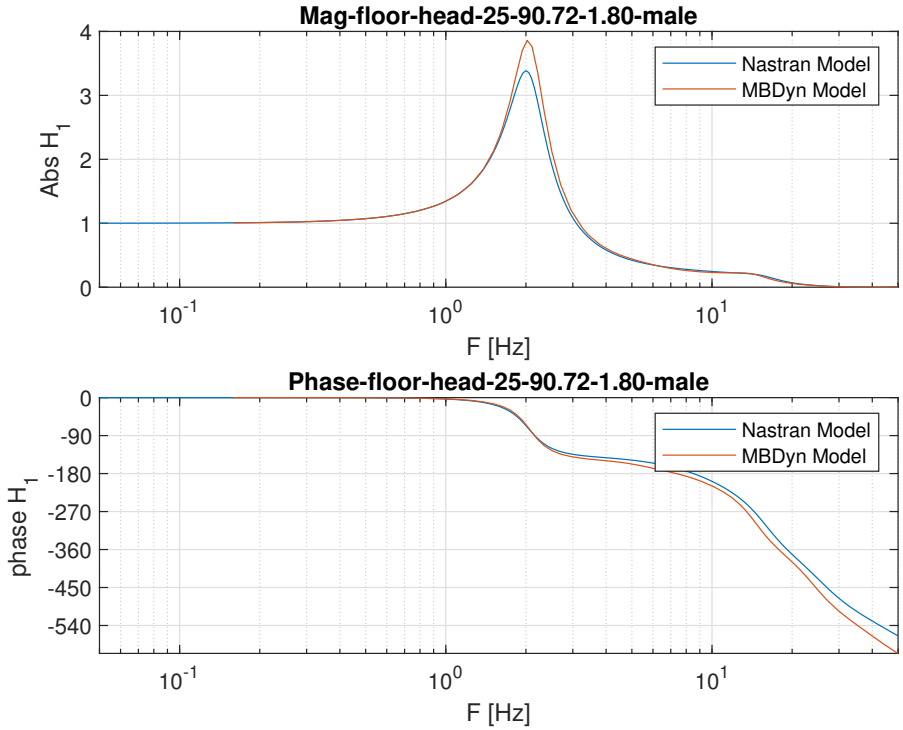

Figure 38: Transfer function between floor and head for a 25 BMI subject

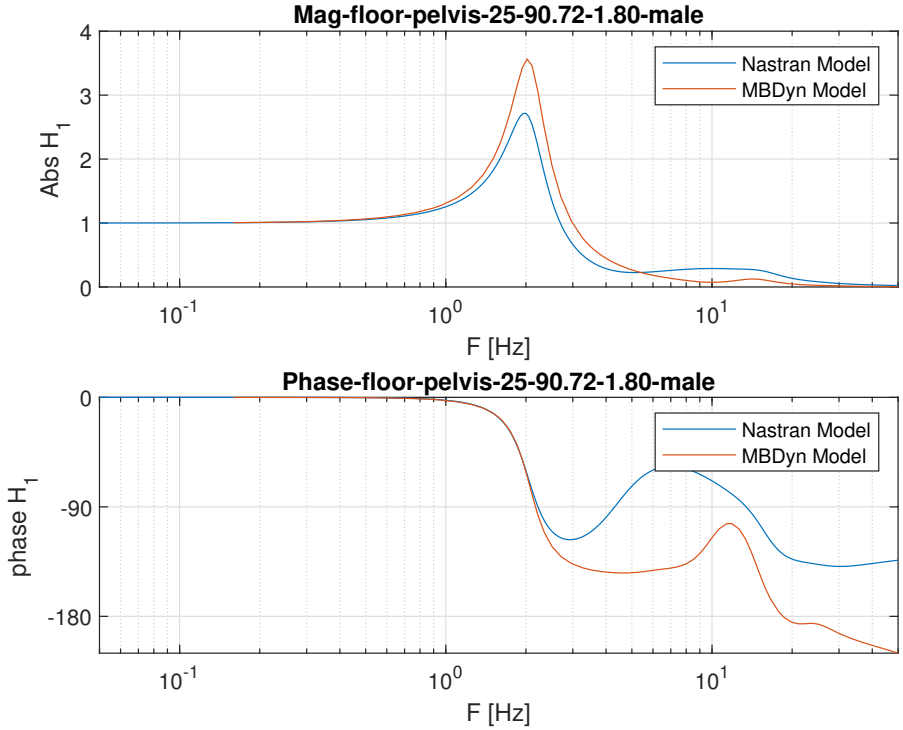

Figure 39: Transfer function between floor and pelvis for a 25 BMI subject

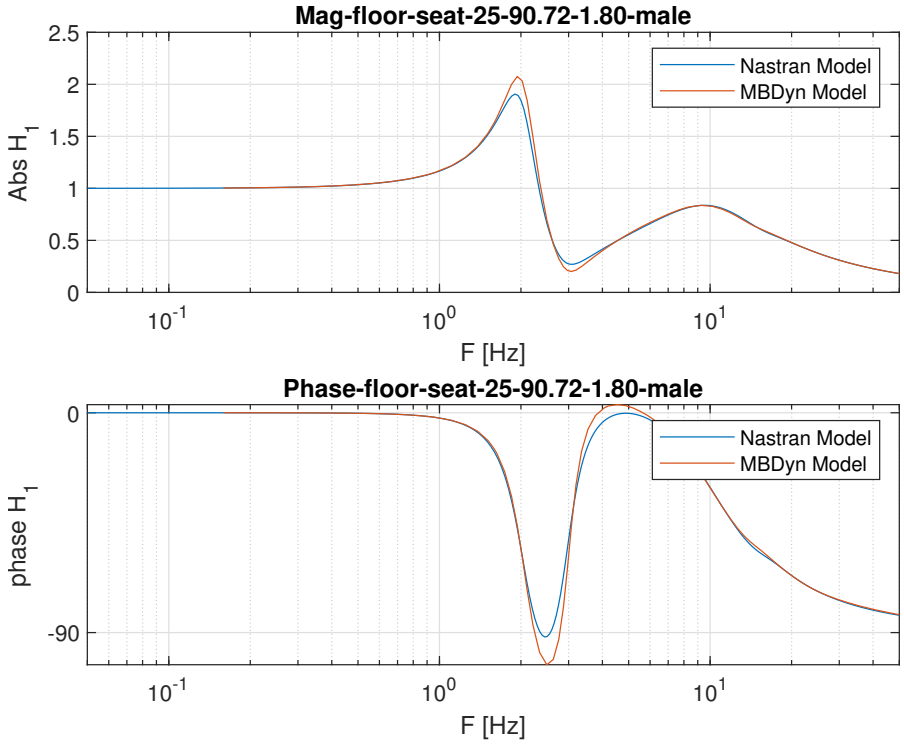

Figure 40: Transfer function between floor and seat for a 25 BMI subject

6.2 COMMAND RESPONSE

In order to establish how the spine dynamic is influencing the system, two models have been analysed. The first model is composed by the upper limbs and the seat: the torso is represented by a concentrated mass of 45 kg, that correspond to the seated mass, attached at the cushion. The limbs are attached to the torso node by a using through spherical joints. The second model is the CMS model described in chapter 4. The simulation was performed from 1 Hz to 15 Hz using a time step of 0.005 s for a total time simulation of 2000 s. Both the displacement and acceleration input has been analyzed: the two transfer functions are related by equation 59:

$$\frac{\theta_s}{\ddot{z}_f} = \frac{1}{s^2}\frac{\theta_s}{z_f} \tag{59}$$

where θ_s is the rotation of the stick, $\ddot{z}_f$ is the acceleration of the floor and z_f is the displacement of the floor. Figure 41 shows the FRF taking as input the acceleration at the floor and as output the rotation of the collective lever, figure 42 instead shows the FRF computed considering as input the floor displacement. Figure 41 shows that the introduction of the deformable element amplifies the rotation of the command: the main resonance peak is found at 1.82 Hz with an amplitude of 3.87 $\mathrm{deg}/\mathrm{m}/\mathrm{s}^2$, instead if only the upper limb model is considered the main resonance peak is found at 2.05 Hz with and amplitude of 2.85

deg /m/s^2. After the resonance peak the amplitude of the model that includes the spine is lower than the one with include only the upper limbs. For what concerns the phase diagram of figure 41, the two system share a similar trend: after the first resonance peak the phase asses at a value of $-270°$.

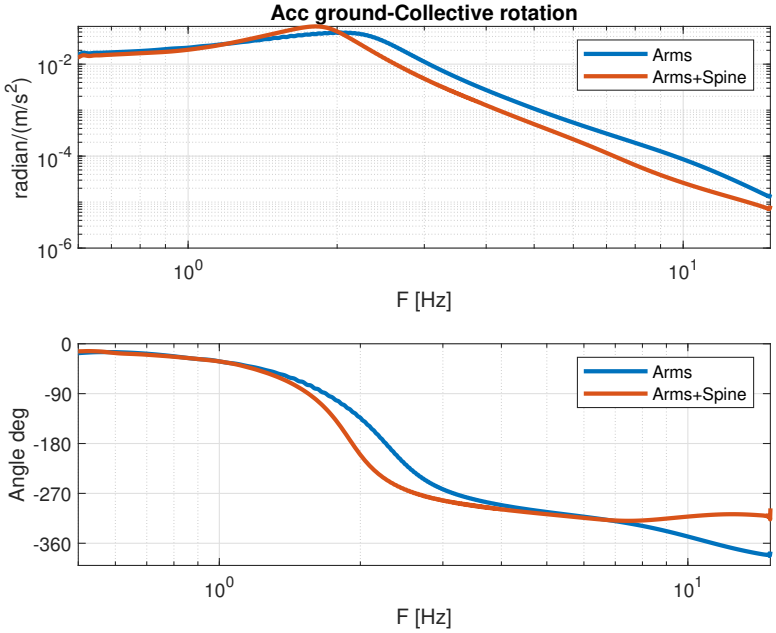

Figure 41: Transfer function between acceleration at the floor and rotation of the collective lever

Figure 43 shows the FRF between the vertical acceleration at the ground and the cyclic rotation in the fore-aft direction. Figure 44 shows the FRF computed considering as input the floor displacement. Considering 43 the complete model shows a damped maximum in the range (1.4-1.8) Hz with a maximum amplitude of 0.5 deg /m/s^2, instead the resonance peak for the upper limbs model is less damped and is located at 1.61 Hz with an amplitude of 0.8 deg /m/s^2. For frequencies above 4 Hz the amplitude of complete model is higher than the upper limbs one.

Figure 45 shows the FRF between the vertical acceleration at the ground and the cyclic rotation in the lateral direction. Figure 46 shows the FRF computed considering as input the floor displacement. Considering 45 the complete model shows a primal resonance peak at 1.37 Hz with an amplitude of 0.87 deg /m/s^2 instead the upper limbs model shows the primal resonance peak at 1.59 Hz with an amplitude of 1.08 deg /m/s^2. It is worth noting that the complete model shows a maximum in the amplitude diagram in the range 1-2 Hz.

Summarizing, adding the spine dynamic to the model increase the amplitude at resonance for the cyclic command. This command, as

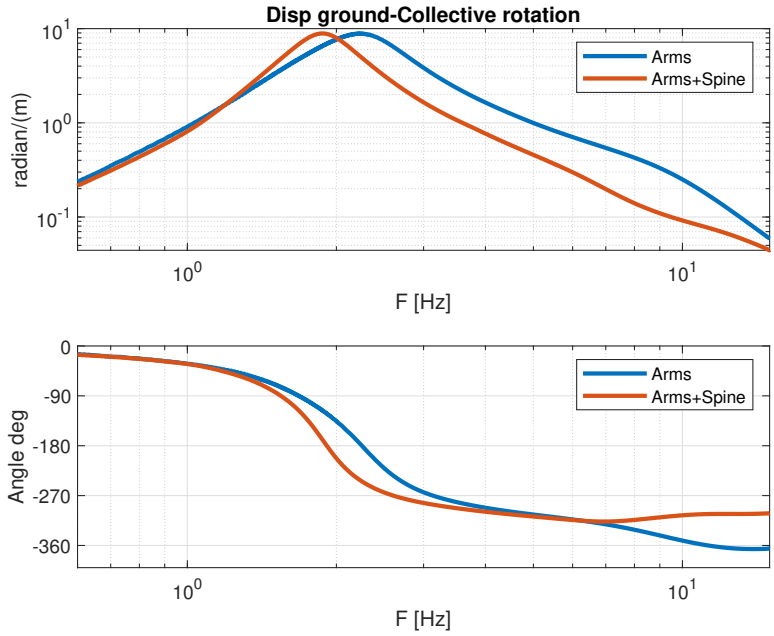

Figure 42: Transfer function between displacement at the floor and rotation of the collective lever

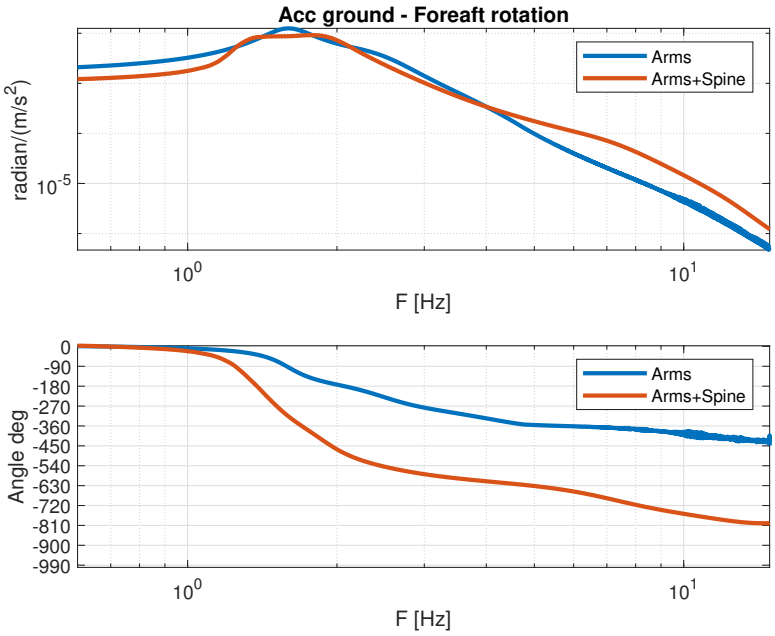

Figure 43: Transfer function between acceleration at the floor and rotation of the cyclic for a fore-aft movement

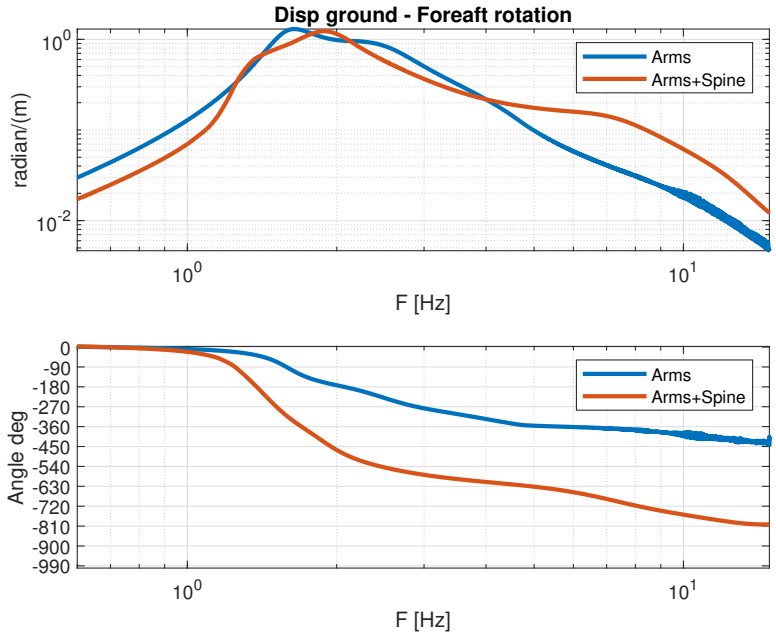

Figure 44: Transfer function between displacement at the floor and rotation of the cyclic for a fore-aft movement

expected, is also the most sensible to vertical accelerations because it moves only vertical direction, controlling the altitude of the rotorcraft. A small coupling between the vertical vibration and the cyclic rotation has been observed in the order of 1° at resonance. In this case the introduction of the spine dynamics alleviates the magnitude of the vibration transmitted to the command at resonance.

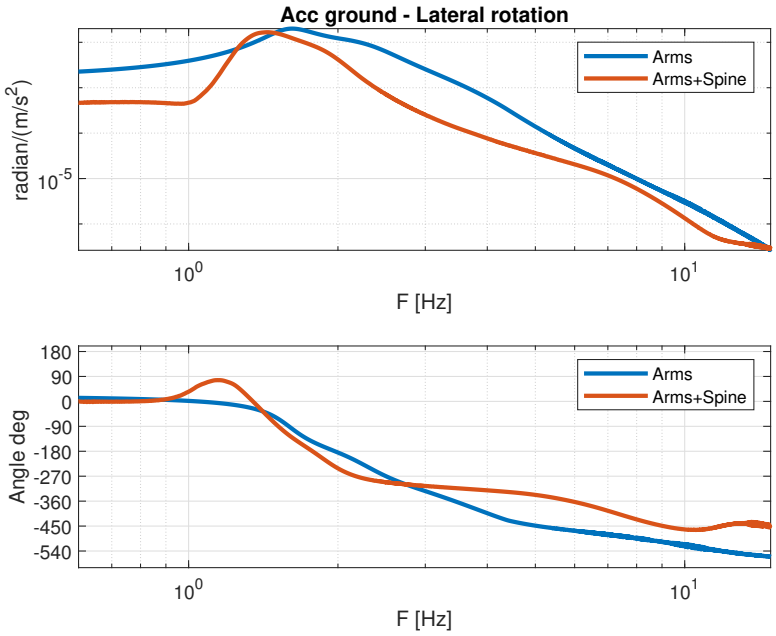

Figure 45: Transfer function between acceleration at the floor and rotation of the cyclic for a lateral movement

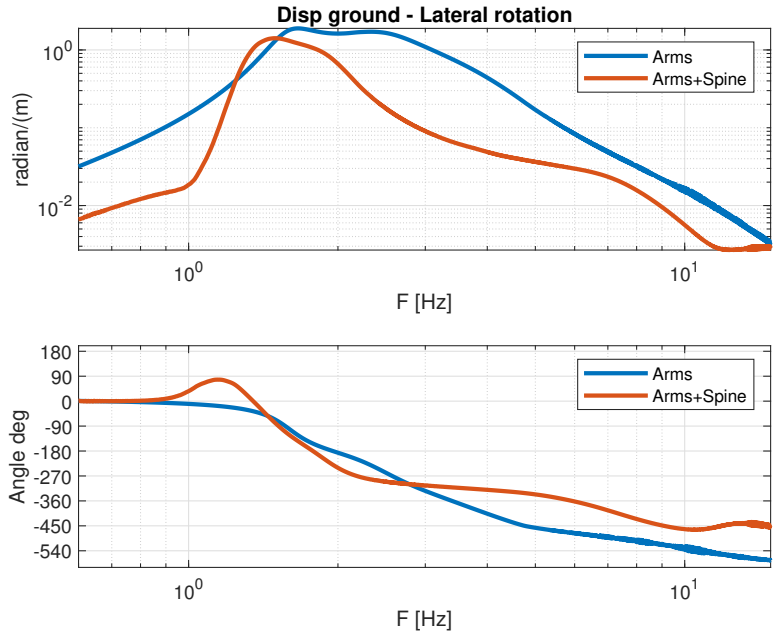

Figure 46: Transfer function between displacement at the floor and rotation of the cyclic for a lateral movement

6.3 AEROSERVOELASTIC ROTORCRAFT MODEL

In this section, the LPM, FEM and MBD spine models are coupled in an aeroservoelastic rotorcraft model in order to evaluate the comfort of the occupants.
Rotorcraft aeroservoelasticity is modeled using Modern Aeroservoelastic State Space Tools (MASST) a tool developed at Politecnico di Milano. MASST analyzes compact, yet complete modular models of linearized aeroservoelastic system [26][23]. In MASST, rotorcraft subcomponents are collected from well-known, reliable and possibly state-of-the-art sources, which are blended together in the scientific computing environment MATLAB. All blocks are cast into state-space form using the Craig-Bamptom CMS method [4]. This approach is crucial to formulate the helicopter subcomponents (rotor, airframe etc..) in their most suitable platform and compose the overall model. In MASST, the assembled model is cast into a quadruple of matrices **A**, **B**, **C**, **D** that define the a state-space system:

$$\begin{cases} \dot{\mathbf{x}} = \mathbf{A}\mathbf{x} + \mathbf{B}\mathbf{f} \\ \mathbf{y} = \mathbf{C}\mathbf{x} + \mathbf{D}\mathbf{f} \end{cases} \tag{60}$$

where vector $\mathbf{x}$ contains the states of the system, $\mathbf{y}$ is the system output, $\mathbf{f}$ includes the inputs. MASST interpolates the state-space model matrices in a generic configuration within the corresponding linear models evaluated in the space of prescribed parameters. In the Laplace domain, the model produces the input-output relationship:

$$\mathbf{y}(s) = \left[\mathbf{C}(s\mathbf{I} - \mathbf{A})^{-1}\mathbf{B} + \mathbf{D}\right]\mathbf{f}(s) = \mathbf{G}(s)\mathbf{f}(s) \tag{61}$$

6.3.1 *Coupling Helicopter and Subjects*

A virtual helicopter model excluding the human biodynamic response can give the necessary insight into the dynamic behavior of the vehicle itself. However, the interface between the human subjects and the vehicle feeds the subjects' dynamic forces and moments induced by vibrations back into the airframe. This feedback might be significant enough to affect the magnitude of the induced acceleration, which in turn cause a different vibration field on the human body than it would be in the uncoupled case.
The combined effect of human biodynamics, seat dynamics and helicopter aeromechanics can only be accurately evaluated using a relatively high-fidelity vehicle model. However, since the mechanical characteristics of a human body change significantly from subject to subject and even within a single subject, and biodynamic models show great diversity, it is required to analyze a broad number of models of variable complexity and large population groups. Therefore, the cost associated with dynamics models is often not affordable.

For this reason, an effective method could take advantage of a platform for high-fidelity aeroservoelastic modeling of rotorcraft, which allows the Noise and Vibration Harshness engineer to modify the dynamics of the baseline plant by adding detailed human feedback models, without the need to re-assemble the coupled model when the biodynamic properties change. Consequently, the common environment supports both fast adaptation of biodynamic models and tracking the effects of design changes on the vibration rating of human occupants.
MASST can export models and proper force-sensor relationships such that any human body can be added as a feedback element that operates from the output of virtual sensors and produces the resulting forces as inputs. For this purpose, it is sufficient to define specific input and output signals in the virtual helicopter model to create the feedback path within the device. According to 47:

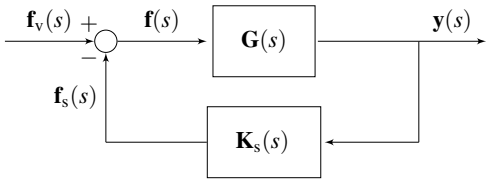

Figure 47: Block diagram representation of the base vehicle, $\mathbf{G}$, and subject feedback, $\mathbf{K}_s$.

- The input for the virtual helicopter model is defined as the vibratory forces (or moments) $\mathbf{f}_v$, acting on any airframe point and/or on the rotors.
- The output $\mathbf{y}$ of the virtual helicopter model is chosen as the sensors of position, velocity, and acceleration of any airframe point (or rotor point in multiblade coordinates); thus it is a linear function of the state and input of the model.
- The subjects create a feedback loop between the sensors corresponding to the motion and the forces exerted by the subjects, $\mathbf{f}_s$, at their attachment points:

$$\mathbf{f}_(s) = \mathbf{K}_s(s)\mathbf{y}(s) \tag{62}$$

such that the total force can be expressed as:

$$\mathbf{f} = \mathbf{f}_v - \mathbf{f}_s \tag{63}$$

where both force vectors have the same sequence of elements. The transfer matrix $\mathbf{K}_s$ represents the synthesis of the human and interface model state-space representation.

Then, the response of the modified system is obtained as:

$$\mathbf{y} = (\mathbf{I} + \mathbf{G}\mathbf{K}_s)^{-1}\mathbf{G}\mathbf{f}_v \tag{64}$$

where matrix $\mathbf{G}$ is the dynamic compliance matrix of the MASST high fidelity tool. The gain matrix $\mathbf{K}_s$ can be easily defined using force-response relationship of the attached human vibration or interface model. The human biodynamic and interface models should be put in state-space form in order to be compatible with MASST:

$$\begin{cases} \dot{\mathbf{x}}_s = \mathbf{A}_s\mathbf{x}_s + \mathbf{B}_s\mathbf{y} \\ \mathbf{f}_s = \mathbf{C}_s\mathbf{x}_s + \mathbf{D}_s\mathbf{y} \end{cases} \tag{65}$$

in which vector $\mathbf{x}_s$ contains the internal state of the subjects, $\mathbf{A}_s$, $\mathbf{B}_s$, $\mathbf{C}_s$, $\mathbf{D}_s$ are the state-space matrices. The state-space form can be made more compact by directly using the transfer function between the problem-specific inputs and outputs:

$$\mathbf{f}_s = \mathbf{K}_s(s)\mathbf{y} = \left[\mathbf{C}_s(s\mathbf{I} - \mathbf{A}_s)^{-1}\mathbf{B}_s + \mathbf{D}_s\right]\mathbf{y} \tag{66}$$

For the Boileau and Rakheja [8] LPM model, the equation of motion were directly written in the state form given in equation 65. The MBD and FEM models input (seat vertical acceleration) to output (head vertical acceleration) transfer functions were numerically estimated. A continuous-time model identification was done using the MATALB system identification toolbox then allowed to determine the most likely Laplace-domain representation of the input-output relationships, that were transferred to state-space form by means of standard canonical realizations.

6.3.1.1 *Helicopter model*

A medium size helicopter showed in figure 48 with an articulated 5 blade main rotor was built in MASST. The state-space model includes:

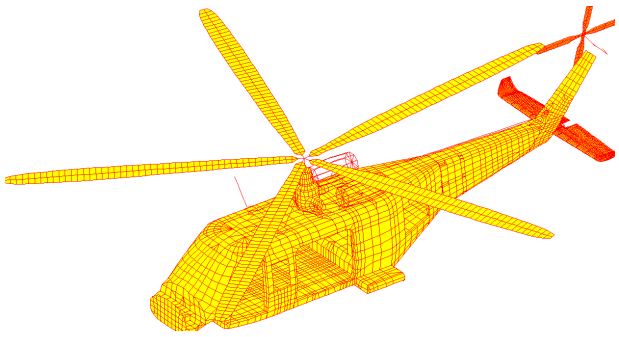

Figure 48: Snapshot of the baseline virtual helicopter model

- Rigid body DOF.
- Flight mechanics derivatives of the airframe, estimated using CAMRAD/JA.
- Elastic bending and torsion modes of the airframe extracted from NASTRAN with 1.5% proportional structural damping added in MASST.
- Transfer functions of main and tail rotor servo actuators directly formulated in Matlab/Simulink, considering servo-valve dynamics and dynamic compliance.
- The node and coordinates for the sensors and the forces, directly defined in MASST.

The vibration performance of the coupled human-interface-helicopter model can be evaluated at any point on the cabin floor. The distribution of occupants within the possible seating locations might have an impact on vibration rating when different combinations of seating arrangements are possible if the number of occupants are less than the number of available seats. However, this variability does not effect the comparison of different biodynamic modeling techniques if the occupied seat remain at the same location of the cabin floor while comparing different biodynamic models. Therefore 10 seats are assembled into the cabin with a uniform distribution as shown in figure 49. At

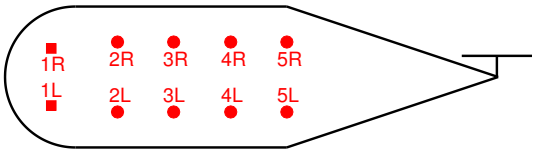

Figure 49: Distribution and labels of seat attachment points on cabin floor

these locations, seats and the biodynamic models obtained using the three model techniques are added, representing the 2 pilots in the cockpit and 8 crew/passenger in vertical seating posture. Based on the acceleration at these 10 points on the cabin floor, an output vector $\mathbf{y}$ is defined as:

$$\mathbf{y} = \begin{Bmatrix} \ddot{z}_{cockpit,1} \\ \ddot{z}_{cockpit,1} \\ \ddot{z}_{cabin,1} \\ \vdots \\ \ddot{z}_{cabin,n} \\ \vdots \\ \ddot{z}_{cabin,8} \end{Bmatrix} \tag{67}$$

Where at each location, $\ddot{z}$ gives the vertical accelerations either of the cushion or of the head. Then, the square of the norm of the accelerations, divided by the number of measurements, is defined as the vibration index:

$$VI = \frac{\sqrt{\mathbf{y}^T\mathbf{y}}}{10} \tag{68}$$

The biodynamics models are added to the aeroservoelastic helicopter model. At the ten locations on the cabin floor shown in figure 49 the accelerations are computed and the vibration index is collected.

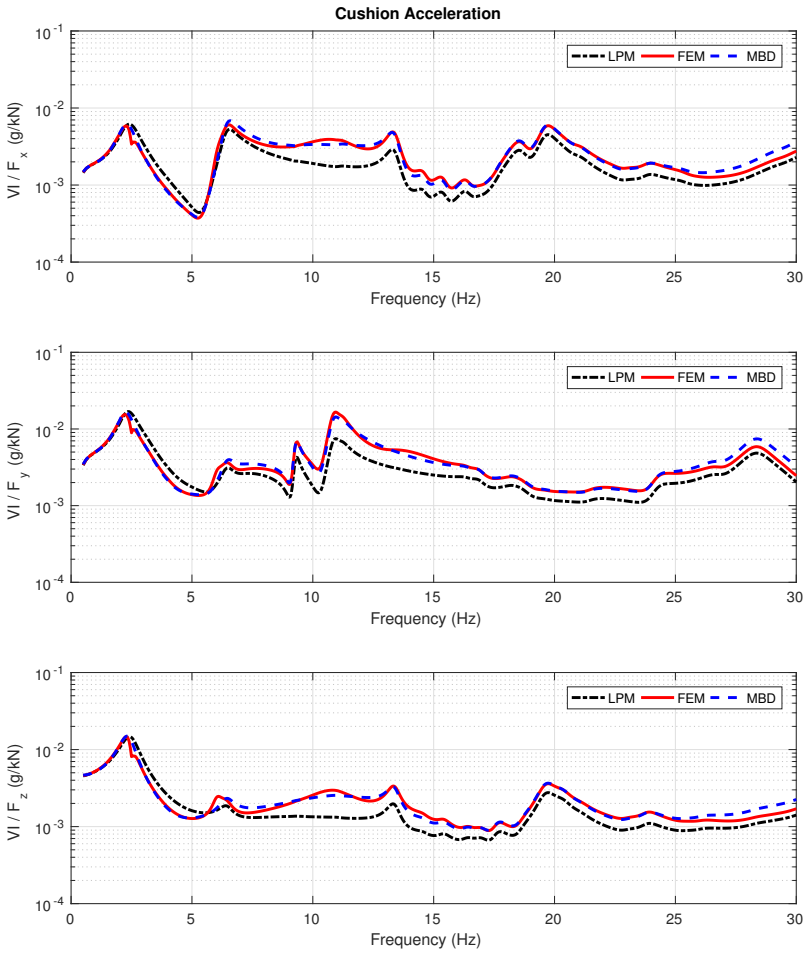

Figure 50: Averaged Frequency Response Function of three biodynamic modeling techniques coupled with seat and helicopter between longitudinal (F_x), lateral (F_y) and vertical (F_z) unit hub forces and the cushion surface.

In figure 50 the results when the acceleration is measured at the cushion surface are shown. All the three models predict the vibrational level within the same order of magnitude, with similar trends. Comparing the results of the isolated models and the one considering the helicopter, the peaks other than the first one slightly above 2Hz, are related to the airframe. In figure 51 presents the results taking as

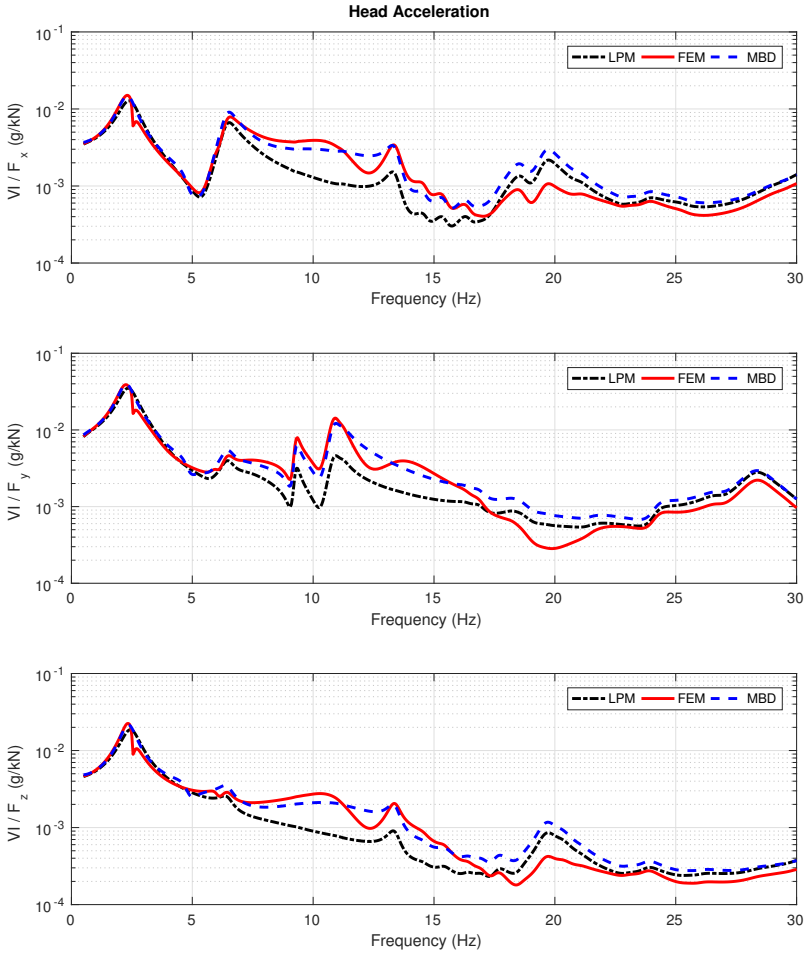

Figure 51: Averaged Frequency Response Function of three biodynamic modeling techniques coupled with seat and helicopter between longitudinal (F_x), lateral (F_y) and vertical (F_z) unit hub forces and the head.

output the head acceleration. In this case the flexibility of the spine influence more the FRF; in fact now the three model presents more differences especially above 5 Hz. High resolution in the spine dynamics are expected to provide better insight: for example the output of these models is far richer with respect to the LPM model, so then the strain between two vertebrae can be evaluated.

7 CONCLUSIONS

7.1 RECAP

The goal of this work was to develop a spine model that can be used for rotorcraft comfort evaluation. In particular in chapter 3 a finite element model based on the one ofKitazaki and Griffin [19] has been developed and validated using experimental data and LPM available in literature that relies on experimental data for the identification of the model. The validation has been done by comparing the modal shapes of the FEM model to the one that are presented in literature; also the frequency response functions, in particular between the buttock down and the head, have been evaluated in the 3 translational directions and the results compared with the experimental results and the LPM models.
One of the great advantages of the FEM models as well as of the MBD models is that are 3 dimensional model, instead the LPM are able to capture only the movement in one direction.
Another great advantage of the FEM and MBD models is that they can be adapted to a specific subject identified by the anthropometric parameters such as gender, age, height and weight.
A validation of this parametrization has been made in chapter 5 in which has been evaluated the apparent mass in the vertical direction of different subjects analysing different seat conditions and the sensitivity to each anthropometric parameter. It turns out that the scaling model is very sensible to stature variation, instead the experiments state that the most sensible parameter is the body weight. The scaling method however well fits the experimental data when a combined variation of the parameters has been made. The scaling process should be improved starting from these results.
In chapter 4 the MBD model of the spine and the upper limb MBD model has been presented. At the end the FEM model and the upper limb one have been coupled together using a CMS approach, also a more sophisticated backrest model that relies on a unilateral nonlinear viscoelastic element, has been proposed. The validation of this coupling has been made comparing the FRF between the ground and the head of the seated FEM model and the CMS model.
In chapter 6 firstly the seated MBD and the seated FEM models have been compared, evaluating, for three different subjects, the FRF between the floor and the head, floor and pelvis, floor and seat. Secondly the FRF response function between the vertical acceleration and displacement applied to the helicopter airframe and the rotation of

control commands, collective and cyclic, have been evaluated, comparing the CMS model to the a MBD model in which the dynamics of the spine has been neglected. The results shows that the collective, as expected, is more sensible to vertical oscillation, in particular by adding the dynamic of the spine, the oscillations of the collective are more pronounce.
At the end the three techniques of human biodynamic modeling have been compared in vertical sitting postures for a rotorcraft comfort evaluation. All three models have been reduced to a state-space form and then coupled to high-fidelity aeroservoelastic model with a seat-cushion interface. The acceleration at the cushion shows similar trends, responses are within the same order of magnitude, therefore it is not easy to justify the modeling and computational cost of FEM and MBD models when the aimed point is only the interface surface. However, the MBD and FEM model are a better choice when the upper body segments are of interest: with respect to the LPM models they are more flexible, and they provide much more detailed outputs, for example the strain between two vertebrae of the spine can be evaluated, and they can be scaled with the anthropometric properties of the subject. In the design phase, however, a conservative approach, considering all the available models to obtain a worst case scenario can be preferable.

7.2 FURTHER DEVELOPMENTS

Up to now the developed spine models show good correlation with the experimental results in particular when the vibration in vertical direction are considered, instead in the lateral, but more significantly in the fore-aft direction the correlation with the experiment is not perfect. In order to obtain a much better correlation an optimization process of the parameter of both FEM and MBD models should be done.
The parameter optimization can be flanked with an experimental campaign in order to have full control on the target subject. In order to improve the scaling methodology, the experimental campaign should be conducted considering a wide spectrum of subjects.
Regarding the coupling between the multibody upper limbs model and the spine one, it would be interesting to evaluate the effects captured by a more detailed modeling of the shoulder in the whole system, starting from the model presented by Zanoni and Masarati [45].

BIBLIOGRAPHY

[1] Wael Abbas. "Optimization of Biodynamic Seated Human Models Using Genetic Algorithms." In: *Engineering* 02 (Jan. 2010), pp. 710–719. DOI: 10.4236/eng.2010.29092.

[2] Brett Allen, Brian Curless, and Zoran Popović. "The space of human body shapes: reconstruction and parameterization from range scans." In: *ACM transactions on graphics (TOG)*. Vol. 22. 3. ACM. 2003, pp. 587–594.

[3] Xian-Xu Bai, Shi-Xu Xu, Wei Cheng, and Li-Jun Qian. "On 4-degree-of-freedom biodynamic models of seated occupants: Lumped-parameter modeling." In: *Journal of Sound and Vibration* 402 (2017), pp. 122–141.

[4] Mervyn CC Bampton and Roy R Craig Jr. "Coupling of substructures for dynamic analyses." In: *Aiaa Journal* 6.7 (1968), pp. 1313–1319.

[5] T Belytschko and E Privitzer. *Refinement and validation of a three-dimensional head-spine model*. Tech. rep. ILLINOIS UNIV AT CHICAGO CIRCLE DEPT OF MATERIALS ENGINEERING, 1978.

[6] T Belytschko, L Schwer, and A Schultz. *A model for analytic investigation of three-dimensional head-spine dynamics*. Tech. rep. ILLINOIS UNIV AT CHICAGO CIRCLE DEPT OF MATERIALS ENGINEERING, 1976.

[7] Richard L Bielawa. *Rotary wing structural dynamics and aeroelasticity*. American Institute of Aeronautics and Astronautics, 2006.

[8] P-É Boileau and Subhash Rakheja. "Whole-body vertical biodynamic response characteristics of the seated vehicle driver: measurement and model development." In: *International Journal of Industrial Ergonomics* 22.6 (1998), pp. 449–472.

[9] Young-Tai Choi and Norman M Wereley. "Biodynamic response mitigation to shock loads using magnetorheological helicopter crew seat suspensions." In: *Journal of Aircraft* 42.5 (2005), pp. 1288–1295.

[10] Rolf R Coermann. "The mechanical impedance of the human body in sitting and standing position at low frequencies." In: *Human factors* 4.5 (1962), pp. 227–253.

[11] Raj Desai, Anirban Guha, and P Seshu. "Multibody Biomechanical Modelling of Human Body Response to Direct and Cross Axis Vibration." In: *Procedia computer science* 133 (2018), pp. 494–501.

[12] Thomas E Fairley and Michael J Griffin. "The apparent mass of the seated human body: vertical vibration." In: *Journal of Biomechanics* 22.2 (1989), pp. 81–94.

[13] Alessandro Fumagalli, Gabriella Gaias, and Pierangelo Masarati. "A simple approach to kinematic inversion of redundant mechanisms." In: *ASME 2007 International Design Engineering Technical Conferences and Computers and Information in Engineering Conference*. American Society of Mechanical Engineers. 2007, pp. 1931–1939.

[14] Kristin L. Harrer, Debra Yniguez, Maria Majar Maria, David Ellenbecker, Nancy Estrada, and Mark Geiger. "Whole Body Vibration Exposure for MH-60S Pilots." In: *43th SAFE*. Utah, USA, 2005.

[15] Katherine RS Holzbaur, Wendy M Murray, and Scott L Delp. "A model of the upper extremity for simulating musculoskeletal surgery and analyzing neuromuscular control." In: *Annals of biomedical engineering* 33.6 (2005), pp. 829–840.

[16] ISO ISO. "2631-1: Mechanical vibration and shock-evaluation of human exposure to whole-body vibration-Part 1: General requirements." In: *Geneva, Switzerland: ISO* (1997).

[17] Wayne Johnson. *Rotorcraft aeromechanics*. Vol. 36. Cambridge University Press, 2013.

[18] Mordechay Karpel and Daniella Raveh. "Fictitious mass element in structural dynamics." In: *AIAA journal* 34.3 (1996), pp. 607–613.

[19] Satoshi Kitazaki and Michael J Griffin. "A modal analysis of whole-body vertical vibration, using a finite element model of the human body." In: *Journal of Sound and Vibration* 200.1 (1997), pp. 83–103.

[20] Satoshi Kitazaki and Michael J Griffin. "Resonance behaviour of the seated human body and effects of posture." In: *Journal of biomechanics* 31.2 (1997), pp. 143–149.

[21] Jack D Leatherwood, Thomas K Dempsey, and Sherman A Clevenson. "A design tool for estimating passenger ride discomfort within complex ride environments." In: *Human Factors* 22.3 (1980), pp. 291–312.

[22] Santosh Mandapuram, Subhash Rakheja, Paul-Émile Boileau, and Setsuo Maeda. "Apparent mass and head vibration transmission responses of seated body to three translational axis vibration." In: *International Journal of Industrial Ergonomics* 42.3 (2012), pp. 268–277.

[23] Pierangelo Masarati, Vincenzo Muscarello, and Giuseppe Quaranta. "Linearized aeroservoelastic analysis of rotor-wing aircraft." In: (2010).

[24] Pierangelo Masarati, Giuseppe Quaranta, and Andrea Zanoni. "Dependence of helicopter pilots' biodynamic feedthrough on upper limbs' muscular activation patterns." In: *Proceedings of the Institution of Mechanical Engineers, Part K: Journal of Multi-body Dynamics* 227.4 (2013), pp. 344–362.

[25] Pierangelo Masarati, Giuseppe Quaranta, and Andrea Zanoni. "A detailed biomechanical pilot model for multi-axis involuntary rotorcraft-pilot couplings." In: (2015).

[26] Pierangelo Masarati, Vincenzo Muscarello, Giuseppe Quaranta, Alessandro Locatelli, Daniele Mangone, Luca Riviello, and Luca Vigano. "An integrated environment for helicopter aeroservoelastic analysis: the ground resonance case." In: (2011).

[27] Frank Henry Netter, Sharon Colacino, et al. *Atlas of human anatomy*. Ciba-Geigy Corporation, 2006.

[28] David Orne and Y King Liu. "A mathematical model of spinal response to impact." In: *Journal of biomechanics* 4.1 (1971), pp. 49–71.

[29] E Pennestrì, R Stefanelli, PP Valentini, and L Vita. "Virtual musculoskeletal model for the biomechanical analysis of the upper limb." In: *Journal of biomechanics* 40.6 (2007), pp. 1350–1361.

[30] Eberhardt Privitzer and Ted Belytschko. "Impedance of a three-dimensional head-spine model." In: *Mathematical Modelling* 1.2 (1980), pp. 189–209.

[31] Subhash Rakheja, RG Dong, S Patra, P-É Boileau, P Marcotte, and C Warren. "Biodynamics of the human body under whole-body vibration: Synthesis of the reported data." In: *International Journal of Industrial Ergonomics* 40.6 (2010), pp. 710–732.

[32] Xiangnan Shi, Libo Cao, Matthew P Reed, Jonathan D Rupp, Carrie N Hoff, and Jingwen Hu. "A statistical human rib cage geometry model accounting for variations by age, sex, stature and body mass index." In: *Journal of biomechanics* 47.10 (2014), pp. 2277–2285.

[33] Aeronautical Design Standard. "Requirements for Rotorcraft Vibration Specifications, Modeling and Testing." In: *US Army Aviation System Command, Novermber* (1986).

[34] International Organization for Standardization. *Mechanical vibration and shock: Range of idealized values to characterize seated-body biodynamic response under vertical vibration*. International Organization for Standardization, 2002.

[35] Ernest L Stech and Peter R Payne. *Dynamic models of the human body*. Tech. rep. Frost Engineering Development Corp Englewood Co, 1969.

[36] A Tamer, V Muscarello, P Masarati, and G Quaranta. "Vibration Rating of Medical Helicopters." In: *74th International Annual Forum American Helicopter Society (AHS)*. 2018, pp. 1–12.

[37] R Toth. "Multiple degree-of-freedom nonlinear spinal model." In: *Proceedings of the 19th Annual Conference on Engineering in Medicine and Biology*. 1967, p. 102.

[38] Martin GR Toward and Michael J Griffin. "Apparent mass of the human body in the vertical direction: Inter-subject variability." In: *Journal of Sound and vibration* 330.4 (2011), pp. 827–841.

[39] Filippo Tunesi. "Modelli dinamici per lo studio delle vibrazioni della colonna vertebrale." In: (2013).

[40] Pier Paolo Valentini. "Virtual dummy with spine model for automotive vibrational comfort analysis." In: *International journal of vehicle design* 51.3-4 (2009), pp. 261–277.

[41] Pier Paolo Valentini and Ettore Pennestrì. "An improved three-dimensional multibody model of the human spine for vibrational investigations." In: *Multibody System Dynamics* 36.4 (2016), pp. 363–375.

[42] Yi Wan and Joseph M Schimmels. "A simple model that captures the essential dynamics of a seated human exposed to whole body vibration." In: *Advances in Bioengineering* (1995).

[43] Takuya Yoshimura, Kazuma Nakai, and Gen Tamaoki. "Multibody dynamics modelling of seated human body under exposure to whole-body vibration." In: *Industrial health* 43.3 (2005), pp. 441–447.

[44] Andrea Zanoni. "Estimation of the Dependence of Upper Limb's Biomechanical Impedance on Muscular Activation Using Inverse Dynamics." In: (2011).

[45] Andrea Zanoni and Pierangelo Masarati. "Geometry generation and benchmarking of a complete multibody model of the upper limb." In: *4th Joint International Conference on Multibody System Dynamics (IMSD 2016)*. 2016, pp. 1–18.

[46] Liu Zhong-hua Li Xiao-ling Zhang E Xu Lin-an. "Dynamic modeling and vibration characteristics of multi-DOF upper part system of seated human body." In: *Chinese Journal of Engineering Design* 15.4, 244 (2008), p. 244. URL: http://www.zjujournals.com/gcsjxb/EN/abstract/article_407.shtml.

DECLARATION

I declare that this thesis was composed by myself, that the work contained herein is my own except where explicitly stated otherwise in the text, and that this work has not been submitted for any other degree or professional qualification.

Milan, April 2019

Alessandro Cocco

COLOPHON

This document was typeset using the typographical look-and-feel `classicthesis` developed by André Miede. The style was inspired by Robert Bringhurst's seminal book on typography "*The Elements of Typographic Style*". `classicthesis` is available for both LaTeX and LyX:

https://bitbucket.org/amiede/classicthesis/